Towards inducing superconductivity into graphene

Dmitri K. Efetov

Submitted in partial fulfillment of the

requirements for the degree

of Doctor of Philosophy

in the Graduate School of Arts and Sciences

COLUMBIA UNIVERSITY

2014

ABSTRACT

Towards inducing superconductivity into graphene

Dmitri K. Efetov

Graphenes transport properties have been extensively studied in the 10 years since its discovery in 2004, with ground-breaking experimental observations such as Klein tunneling, fractional quantum Hall effect and Hofstadters butterfly. Though, so far, it turned out to be rather poor on complex correlated electronic ground states and phase transitions, despite various theoretical predictions. The purpose of this thesis is to help understanding the underlying theoretical and experimental reasons for the lack of strong electronic interactions in graphene, and, employing graphenes high tunability and versatility, to identify and alter experimental parameters that could help to induce stronger correlations.

In particular graphene holds one last, not yet experimentally discovered prediction, namely exhibiting intrinsic superconductivity. With its vanishingly small Fermi surface at the Dirac point, graphene is a semi-metal with very weak electronic interactions. Though, if it is doped into the metallic regime, where the size of the Fermi surface becomes comparable to the size of the Brillouin zone, the density of states becomes sizeable and electronic interactions are predicted to be dramatically enhanced, resulting in competing correlated ground states such as superconductivity, magnetism and charge density wave formation. Following these predictions, this thesis first describes the creation of metallic graphene at high carrier doping via electrostatic doping techniques based on electrolytic gates. Due to graphenes surface only properties, we are able to induce carrier densities above $n > 10^{14}$ cm^{-2} ($\varepsilon_F > 1$ eV) into the chemically inert graphene. While at these record high carrier densities we yet do not observe superconductivity, we do observe fundamentally altered transport properties as compared to semi-metallic graphene. Here, detailed measurements of

the low temperature resistivity reveal that the electron-phonon interactions are governed by a reduced, density dependent effective Debey temperature - the so-called Bloch-Grüneisen temperature Θ_{BG}. We also probe the transport properties of the high energy sub-bands in bilayer graphene by electrolyte gating. Furthermore we demonstrate that electrolyte gates can be used to drive intercalation reactions in graphite and present an all optical study of the reaction kinetics during the creation of the graphene derived graphite intercalation compound LiC_6, and show the general applicability of the electrolyte gates to other 2-dimensional materials such as thin films of complex oxides, where we demonstrate gating dependent conductance changes in the spin-orbit Mott insulator Sr_2IrO_4.

Another, entirely different approach to induce superconducting correlations into graphene is by bringing it into proximity to a superconductor. Although not intrinsic to graphene, Cooper pairs can leak in from the superconductor and exist in graphene in the form of phase-coherent electron-hole states, the so-called Andreev states. Here we demonstrate a new way of fabricating highly transparent graphene/superconductor junctions by vertical stacking of graphene and the type-II van der Waals superconductor $NbSe_2$. Due to $NbSe_2$'s high upper critical field of $H_{c2} = 4$ T we are able to test a long proposed and yet not well understood regime, where proximity effect and quantum Hall effect coexist.

Table of Contents

List of Figures

Acknowledgments

First and foremost I want to thank my advisor Philip Kim, who I will be always grateful for taking me into his group and giving me the opportunity to learn and grow under his supervision. Not only did I learn a great deal from his broad knowledge of experimental condensed matter physics, but not less importantly, from his wisdom in dealing with people, always trying to involve and to find a compromise with everybody. Despite an overly busy travelling schedule he always found time for countless scientific and personal discussions, which in good times, when the projects were running well, tremendously helped to push forward the experimental progress, and in bad times, when they didn't, had shear endless patience, never letting you give up, always trying to re-focus ones moods and bring things back on track. Thank you for your guidance!

Also I owe a great debt of gratitude to Igor Aleiner as he has been a big source of help and advice since the very first day I stepped on the campus of Columbia. Besides having taught me most of what I know about statistical mechanics and condensed matter physics in his classes, he also always found time for active scientific discussions, and, with his creativity and almost encyclopedic knowledge, on many occasions pointed out ideas which turned out to be crucial for the understanding of my experiments. I will also miss the condensed matter seminars - they aren't going to be the same without Igor's input.

Having spent now about seven years in the Kim group I have seen several generations of postdocs, graduate and undergraduate students entering and leaving the group. I have to address thanks to everybody who worked with me, be it just through fruitful discussions or in direct involvement in the experiments. It all started with Barbaros Oezylmaz and Pablo Jarillo-Herrero who took me in into their project and taught me everything there is

to know about fabrication techniques, and, along the way, also gave me a first glimpse of what it means to be a scientist, to run an experiment from start to finish, starting with an idea and finishing with a experimental observation.

I also want to thank all the graduate students and postdocs with which I had the pleasure working and sharing an office throughout the years. Meninder Purewal who tried to accommodate me in my very beginning and invited me to his parents place for my first US christmas, Erik Henriksen who was the first to show me how to use a cryostat, Kirill Bolotin for having always a sarcastic phrase to cheer one up, Yuri Zuev for being my room-mate in the first two years, Melinda Han for being always approachable, Yue Zhao for cheering people up by always being in a great mood, Andrea Young as he was always one step ahead and was a good role-model, Mitsuhide Takekoshi who had always a helping hand, Vikram Deshpande who impressed me with his knowledge in various fields of condensed matter physics, Patrick Maher for being a great and knowledgeable office mate, Jayakanth Ravinchandran as he cheered me up in the last two years, and for the countless discussion on materials science, Chul-Ho Lee for being the proof that hard work pays off, Jean-Damian Pillet for teaching me proximity effect and Frank Zhao for trying to continue some of my experiments. I also cherish the many relationships which developed with co-workers from other group and fields - Kin Fai Mak, Inanc Meric, Chengyao Chen, Cory Dean, Lei Wang, Yinsheng Guo. Special thanks also to the undergraduates I had the honor to supervise Simas Glinskis, Nathan Booth and Clevin Handschin. Without their hard work many of the experiments would not have been pushed forward the way the did.

Last but now least I also want to thank my parents, who supported me in any way imaginable throughout my whole PhD adventure. Without their ongoing inspiration and encouragement this thesis could not have been completed. Thank you all!!!

To my parents Olga V. Efetova and Konstantin B. Efetov.

Chapter 1

Introduction

1.1 Overview and outline

Having joined Philip Kim's research group as an undergraduate student in 2006, with graphene haven been discovered only 2 years prior, put me instantly in the position of an observer from within in an extremely dynamic and, in retrospect, with the award of the Nobel prize for the discovery of graphene in 2010, historic stretch of condensed matter research. At that time, graphene had received immense attention for its massless Dirac Fermion physics and its unexpectedly high electronic quality which led to the observation of the unusual half-integer quantum Hall effect [1; 2; 3; 4].

Albeit being a superb ballistic conductor with unusual single particle properties, as soon as I started my PhD in 2007, I began to hear voices asking wether graphene also could sustain more complex electronic phases and phase transitions, such as superconductivity or exciton condensation [5; 6; 7; 8; 9; 10]. The search of such exotic phases started first at close proximity of the Dirac point. However, specifically with regard to intrinsic superconductivity in graphene, we quickly realized that the regime where we could have the best chance of observing it, would be in the opposite limit where the Fermi energies are as far away from the Dirac point as possible. This initial intuition resulted in an active search for the regimes where graphene could potentially have a superconducting order, starting a

strong push towards inducing record high carrier densities with electrolyte gates and ended with the induction of superconducting correlations into graphene via proximity effect.

In Chapter 1, we first quickly introduce graphene and its electronic properties [11; 12; 13; 14; 15; 16; 17] and present band-structure calculations with a specific focus on singular points where the density of states has strongly elevated values, the so-called van Hove singularities [9], and put these into context with theoretical predictions for intrinsic superconductivity in graphene. Then we introduce general concepts of the superconducting proximity effect [18] and explain how these manifest themselves when coupled with the Dirac equation in graphene [19].

In Chapter 2 we discuss electrolyte gating concepts and its implications to various materials [20; 21; 22; 23; 24; 25]. Motivated by the at the time mostly unstudied properties of graphene at higher carrier densities and the intriguing theoretical predictions for this regime [10], we decided to apply stronger gating techniques to graphene devices. For this purpose we used a solid polymer electrolyte gate that had before been demonstrated for other thin films and improved it for the use with graphene [26]. With these experimental techniques at hand almost any thin film material can be gated, especially materials with complex carrier density dependent phase transition like cuprates or complex oxides [24].

In this chapter we will introduce basic electrochemical concepts and experimental techniques and present the application of these to materials such as graphene, graphite and complex oxides. While for the case of graphene we will present a detailed approach to introduce highest possible carrier densities with a solid polymer electrolyte gate, in the case of the complex oxide Sr_2IrO_4 we use the ionic liquid DEME-TFSI and compare the effect of electrostatic gating with that of chemical doping. Finally we discuss the limits of electrolyte gating when electrochemical reactions set on at high gate voltages and demonstrate that these can be used to intercalate ionic species into graphite to form crystallized intercalation compounds.

Chapter 3 mainly deals with the application of the electrolytic gates to monolayer and bilayer graphene devices. The extreme tunability of graphene with the electrolytic gates

makes it possible to tune the Fermi energy continuously from $\epsilon_F \sim 0$ eV to $\epsilon_F > 1$ eV, allowing to study not only graphenes properties at high carrier densities, but also a material at the cross-over from a zero band-gap semi-conductor to a metal [26]. While here graphene does not show clear signs of superconductivity even at the highest carrier densities we achieved so far, these studies help to fill an empty space in the big phase space of graphenes properties [27].

Along those lines we present a carrier density dependent study of the temperature dependent resistivity of monolayer graphene at the cross-over from a semi-metal to a metal. Here we find that the fundamental electron-phonon scattering process is governed by a new characteristic temperature scale, the Bloch-Grüneisen temperature Θ_{BG}, and investigate its striking density dependence. Moreover we present a study of bilayer graphene where, for the first time, we were able to fill up the high-energy sub-bands, resulting in a multi-band conduction regime.

In Chapter 4, we discuss in detail our efforts to induce superconducting correlations into graphene via proximity effect. This study was mainly motivated by a set of long standing theoretical predictions such as the possibility of specular Andreev reflections in graphene [19], and the interplay of Andreev reflections with the quantum Hall effect [28; 29]. To approach the regime where these predictions could be realized, both ultra clean graphene and a very transparent electrical contact to a type-II superconductor with a large SC gap are needed. While over the years the quality of graphene has been improved tremendously [30], coupling it with such superconductors has been challenging [31; 32], mainly due to the invasiveness of the deposition techniques such as sputtering or evaporation.

Here we discuss our novel approach to contact high quality hBN/graphene stacks with the layered van der Waals material $NbSe_2$ employing the recently developed stacking technique. We show that the so fabricated graphene/$NbSe_2$ junctions yield very transparent Ohmic interfaces, resulting in a high probability of the Andreev reflections. Furthermore, as $NbSe_2$ is a type-II superconductor with a relatively high $H_{c2} \sim 4$ T, Andreev reflections can be retained up to fields where the quantum Hall effect is fully developed.

1.2 Theoretical overview of graphene

1.2.1 Graphenes band structure from the tight-binding approximation

Monolayer graphene

Graphene is a single sheet of carbon atoms arranged symmetrically in a two-dimensional honeycomb lattice (Fig. 1.1 (a)). The unit cell in the Bravais lattice contains two equivalent carbon atoms referred to as the A and B sub-lattice sites with the inter-atomic distance $a_0 = 1.42$ Åand the lattice constant $a = \sqrt{3}a_0 = 2.46$ Å. The two unit vectors of this lattice (Fig. 1.1 (c)) are defined :

$$\vec{a_1} = \left(\frac{\sqrt{3}a}{2}, \frac{a}{2}\right) \quad ; \quad \vec{a_2} = \left(\frac{\sqrt{3}a}{2}, -\frac{a}{2}\right) \tag{1.1}$$

with the vectors connecting the nearest neighbors being :

$$\vec{\delta_1} = \frac{a}{2}\left(\frac{1}{\sqrt{3}}, 1\right) \quad ; \quad \vec{\delta_2} = \frac{a}{2}\left(\frac{1}{\sqrt{3}}, -1\right) \quad ; \quad \vec{\delta_3} = \frac{a}{2}\left(\frac{2}{\sqrt{3}}, 0\right) \tag{1.2}$$

and the $\vec{K}$, $\vec{K'}$ vectors in the reciprocal space :

$$\vec{K} = \left(0, \frac{4\pi}{3a}\right) \quad ; \quad \vec{K'} = \left(0, \frac{-4\pi}{3a}\right) \tag{1.3}$$

Each carbon atom has three nearest neighbors, lying in a 120° angle to one another and six electrons, of which four are valence electrons - one in the $2s$ and three in the $2p$ orbitals. Embedded in the two dimensional crystal, the $2s$, $2p_x$ and the $2p_y$ orbitals hybridize to form three in-plane sp^2 orbitals determining the σ-bonds, and one $2p_z$ orbital forming the covalent π-bonds between the neighboring atoms. The in-plane σ-bonds are extremely strong and contribute to the structural stability of graphene, making it the strongest material in the world. The electrons in the σ-bonds are very tightly bound and are localized at relevant energy scales. The delocalized π-bands however cross the Fermi energy and therefore

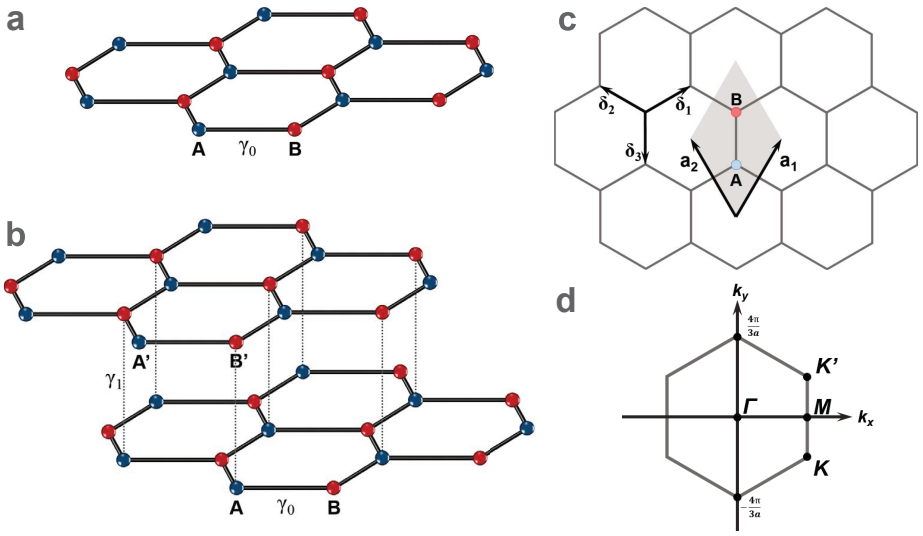

Figure 1.1: (a) and (b) Crystallographic schematics of monolayer and bilayer graphene. The π-electrons can move in-plane between the two equivalent lattice sites A and B and are connected through the hopping integral γ_0. In bilayer graphene, the carbon sheets are Bernal stacked with the A site on the lower sheet sitting directly below the B' site of the upper sheet. Here A and B' and are coupled through the hopping integral γ_1.
(c) Graphenes unit cell with two equivalent carbon atoms spanned by the unit cell vectors $\vec{a_1}, \vec{a_2}$. The nearest-neighbor vectors are $\vec{\delta_1}, \vec{\delta_2}, \vec{\delta_3}$. (d) Graphenes Brillouin zone with the high-symmetry points K, K', M and Γ.

determine the low energy electronic properties of graphene.

Although the electrons in the π-bands are not as strongly bound as in the σ-bands, the tight-binding approximation still provides very accurate estimates. Considering only nearest neighbor hopping the tight-binding Hamiltonian is given [33] :

$$\mathcal{H} = \gamma_0 \sum_{\langle i,j \rangle} (\hat{a}_i^\dagger \hat{b}_j + h.c.) \tag{1.4}$$

where $\gamma_0 \approx 3.16$ eV is the overlap integral between the p_z states of the carbon atoms and $\hat{a}_i^\dagger$, $(\hat{a}_i)$, $\hat{b}_i^\dagger$, $(\hat{b}_i)$ are the creation and annihilation operators for the lattice sites A and B respectively and $\langle i, j \rangle$ are a pair of nearest carbon atoms. This Hamiltonian can be expressed with respect to the basis of the wave-function amplitudes on the individual sub-lattice sites A and B (ψ_A, ψ_B) :

$$\mathcal{H} = \begin{pmatrix} 0 & \gamma_0 \sum_i e^{-i\vec{k}\vec{\delta_i}} \\ \gamma_0 \sum_i e^{i\vec{k}\vec{\delta_i}} & 0 \end{pmatrix} \tag{1.5}$$

and results in two bands defined as the valence $\pi(-)$ and the conduction $\pi^*(+)$ bands (Fig. 1.2 (a)), defined by the two energy eigenvalues :

$$\varepsilon_{\pm}(\vec{k}) = \pm\gamma_0 \sqrt{1 + 4\cos\left(\frac{\sqrt{3}ak_x}{2}\right)\cos\left(\frac{ak_y}{2}\right) + 4\cos^2(ak_y)} \tag{1.6}$$

The energy spectrum of this relation results in a large gap in the Brillouin zone (BZ) center which smoothly closes at corners of the BZ (K and K'). As each carbon atom contributes exactly one electron to the π-bands, each band is exactly half filled with the Fermi energy ϵ_F sitting in the overlap regions of the π and π^* bands, the K and K' points with $\varepsilon_{\pm}(\vec{K}) = \varepsilon_{\pm}(\vec{K'}) = 0$. Around this point the dispersion relation is defined by two equivalent linear regions, the so-called Dirac cones (Fig. 1.2 (b)) with its singular overlapping point, the Dirac point. As the Fermi surface in this point is infinitely small, graphene, in all generality, can be defined as a zero band-gap semiconductor.

To better illustrate the peculiar low energy properties of graphene we rewrite the Hamiltonian in the new basis $(\psi_{K,A}, \psi_{K,B}, \psi_{K',B}, \psi_{K',A})$ of the wave-function amplitudes on the A and B lattice sites near the K, K' points [11; 17]. Furthermore we expand the Hamiltonian for low energies around the $\vec{K}$-points with $\vec{\kappa} \equiv \vec{K} - \vec{k}$ and the Fermi velocity $\upsilon_F = \frac{\sqrt{3}a\gamma_0}{2} \approx 10^6$ m/s :

$$\mathcal{H} = \begin{pmatrix} 0 & i\upsilon_F|\vec{\kappa}|e^{-i\theta} & 0 & 0 \\ -i\upsilon_F|\vec{\kappa}|e^{i\theta} & 0 & 0 & 0 \\ 0 & 0 & 0 & i\upsilon_F|\vec{\kappa}|e^{i\theta} \\ 0 & 0 & -i\upsilon_F|\vec{\kappa}|e^{-i\theta} & 0 \end{pmatrix} = \upsilon_F \begin{pmatrix} \hat{\vec{\sigma}} \cdot \vec{\kappa} & 0 \\ 0 & -\hat{\vec{\sigma}} \cdot \vec{\kappa} \end{pmatrix} \tag{1.7}$$

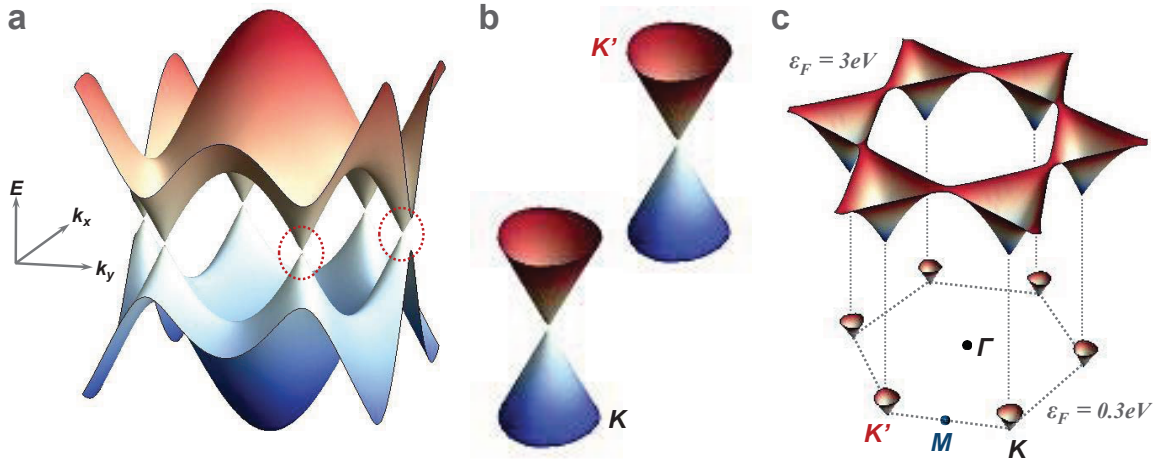

Figure 1.2: (a) π-bands of graphene from the tight-binding approximation. At zero doping the bands are half-filled with the Fermi energy sitting exactly at the touching points of the Dirac cones, the so-called Dirac points. (b) Low energy spectrum with the two linear Dirac cones in the BZ corner sites K and K'. (c) Fermi surface for different values of the Fermi energy ϵ_F. At high energies the two separated valleys merge together in the M-point and form a large single Fermi surface. The electronic properties at these energies are no longer defined by the relativistic Dirac equation.

where $\hat{\vec{\sigma}} = (\sigma_x, \sigma_y)$ is the Pauli matrix operator with :

$$\sigma_x = \begin{pmatrix} 0 & i \\ -i & 0 \end{pmatrix} \quad ; \quad \sigma_y = \begin{pmatrix} 0 & 1 \\ 1 & 0 \end{pmatrix} \tag{1.8}$$

leading essentially to two decoupled valleys in the corners of the BZ with each valley having a linear energy dispersion relation :

$$\epsilon(\vec{\kappa}) = \pm \upsilon_F |\vec{\kappa}| \tag{1.9}$$

The linear dispersion relation is a consequence of the fact that the Hamiltonian in Eqn. 1.7 is identical to the Dirac Hamiltonian of zero-mass relativistic particles, like photons or neutrinos, with the Fermi velocity replacing the speed of light. One of the peculiarities of the Dirac equation is that it directly ties the direction of the spin of the particle with its

momentum, a concept called chirality. In graphene the electron spin is decoupled from the degrees of motion, but the spinor (ψ_A, ψ_B), termed as pseudo-spin, replaces the role of the spin for Dirac Fermions. The electrons in graphene therefore are chiral with its momentum intimately tied with the pseudo-spin direction. Although just a mathematical peculiarity seemingly not having direct relativistic particles in play, the description of the electrons with the Dirac equation has real consequences on the conduction properties of graphene. The most striking consequence is the observation of Klein tunneling in graphene, a counter-intuitive relativistic phenomena where the transmission probability of a relativistic particle incident on a potential barrier is increasingly higher the higher the barrier becomes, reaching perfect transmission for infinitely high barriers. This effect also explains the absence of back-scattering in graphene which in turn leads to the very high observed mobilities.

At high energies, the Fermi surface alters dramatically from the low energy case as is demonstrated in Fig. 1.2 (c). Instead of the two small circular Fermi surfaces around the K and K' points and a linear dispersion relation around them, the two valleys are trigonally warped and merge together at around $\epsilon \sim 3$ eV to form a single Fermi surface spanning the entire BZ. The dispersion relation around these energies is not linear and results in flat band regions. In particular in the M-points, the band exhibits saddle point behaviour with an extremely high density of states (DOS), resulting in van Hove singularities (vHS). With its large Fermi surface in this regime graphene can be better described as a good metal rather than a zero band-gap semiconductor and is predicted to exhibit strong correlated electronic states, such as superconductivity, typically found only in metallic systems.

Bilayer Graphene

Though the properties of monolayer graphene are key to understand bilayer graphene, it is an entirely different electronic system. The π-bands in bilayer graphene can also be calculated by a tight-binding Hamiltonian taking only inter-layer and intra-layer nearest-neighbor interactions into account, though here the picture turns out to be quite more complicated with now four carbon atoms in the unit cell and new hopping terms coupling the two graphene sheets, hence resulting in now four π-bands. In addition, the two graphene

sheets can generally have two different potential energies, for example due to the application of a transverse electric field, where a finite layer potential difference Δ leads to a reconstruction of the band-structure and an opening of a band-gap around the charge neutrality point (CNP).

In the context of this thesis we will be only covering Bernal stacked or A-B stacked bilayer graphene, where the two monolayers are stacked such that the B atom in the upper sheet sits directly above the A atom of the lower sheet (Fig. 1.1 (b)). Although there can be many other arrangements of two stacked graphene sheets, Bernal stacked graphene is the most common form and we will only focus on this type as it has been used for the experiments in this thesis. We further will only consider one hopping term $\gamma_1 \approx 0.4$ eV between the two layers that is corresponding to hopping from A to B', and neglect all other hopping terms. Although such an approximation fails to elucidate the ultra low energy properties of the bilayer graphene band-structure, it provides very good estimates for higher energies and is fully sufficient for our experimental work.

The four atoms in the unit cell consist of two atoms on each graphene sheet with the assigned indices A, B and A', B' correspondingly. We can write the Hamiltonian in the basis of the four local density wave-functions $(\psi_A, \psi_B, \psi_{A'}, \psi_{B'})$ essentially doubling the single layer Hamiltonian in Eqn. 1.7 and additionally introduce the A-B' inter-layer hopping term expressed by γ_1 [34; 35]. In addition we account for the potential difference between the two graphene sheets expressed by $\Delta = V_1 - V_2$, with V_1, V_2 being the potential energy of each graphene layer :

$$\mathcal{H} = \begin{pmatrix} -\Delta/2 & \gamma_0 \sum_i e^{-i\vec{k}\vec{\delta_i}} & 0 & 0 \\ \gamma_0 \sum_i e^{-i\vec{k}\vec{\delta_i}} & -\Delta/2 & \gamma_1 & 0 \\ 0 & \gamma_1 & \Delta/2 & \gamma_0 \sum_i e^{-i\vec{k}\vec{\delta_i}} \\ 0 & 0 & \gamma_0 \sum_i e^{-i\vec{k}\vec{\delta_i}} & \Delta/2 \end{pmatrix} \tag{1.10}$$

again expanding for low energies around the K-point with $\vec{\kappa} \equiv \vec{K} - \vec{k}$ we can rewrite the

Hamiltonian :

$$\mathcal{H} = \begin{pmatrix} -\Delta/2 & iv_F|\vec{\kappa}|e^{-i\theta} & 0 & 0 \\ -iv_F|\vec{\kappa}|e^{i\theta} & -\Delta/2 & \gamma_1 & 0 \\ 0 & \gamma_1 & \Delta/2 & iv_F|\vec{\kappa}|e^{-i\theta} \\ 0 & 0 & -iv_F|\vec{\kappa}|e^{i\theta} & \Delta/2 \end{pmatrix} \tag{1.11}$$

yielding the following four-band dispersion relation (Fig. 1.3):

$$\epsilon^{\pm}_{1,2}(\vec{\kappa}) = \pm\sqrt{\frac{\gamma_1^2}{2} + \frac{\Delta^2}{4} + \hbar^2 v_F^2\kappa^2 \pm \sqrt{\frac{\gamma_1^4}{4} + \hbar^2 v_F^2\kappa^2(\gamma_1^2 + \Delta^2)}} \tag{1.12}$$

This dispersion relation yields now four sub-bands, with two low energy sub-bands touching in the zone center at zero energy ($\Delta = 0$ eV) and two sub-bands originating at higher(lower) energies $|\epsilon| > \gamma_1 \approx 0.4$ eV. Just like in the monolayer case, here the Fermi energy of neutral bilayer graphene sits in the singular overlapping point of the two low-energy sub-bands at half-filling, hence defining bilayer graphene as a zero-gap semiconductor. Though for $\Delta \neq 0$ eV a band-gap is opened between the two sub-bands, now defining bilayer graphene as a semiconductor with a gate tunable gap reaching values of up to $\Delta \sim 200$ meV.

In general, similarly to the case of monolayer graphene one can expand the bilayer graphene Hamiltonian for low energies around the K- and $K^{'}$-points and show that the low energy spectrum in bilayer graphene also obeys the Dirac equation, only this time for massive chiral particles, comparable to massive near-relativistic neutrinos.

1.2.2 Van Hove singularities in graphene

In search for exotic correlated states and many-body interactions in new materials, a very strong attention is often directed to positions in the band-structure where the density of states (DOS) is extremely high or exhibits non-monotonic behaviour as a function of energy.

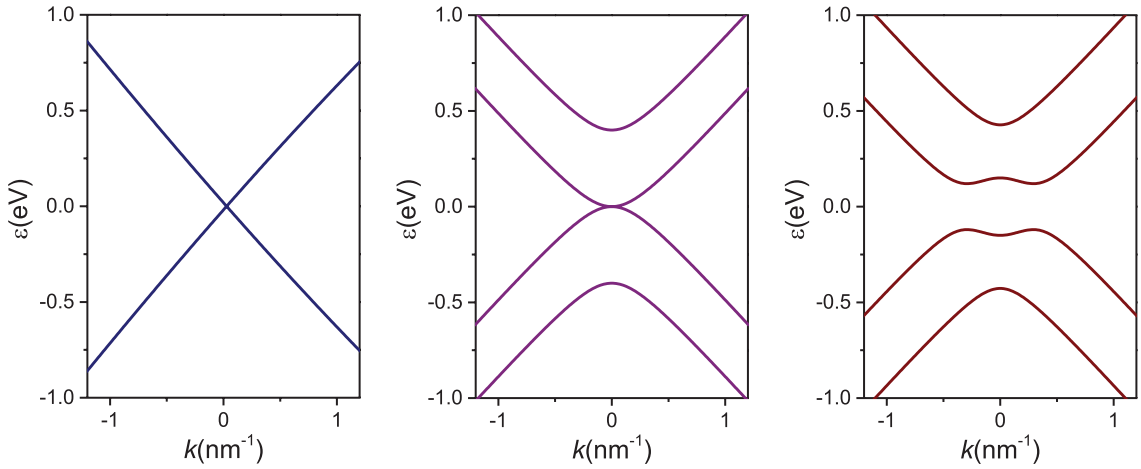

Figure 1.3: Band-structure in the BZ corner K of single layer graphene (left), un-gapped bilayer graphene with $\Delta = 0$ eV (center) and gapped bilayer graphene with $\Delta = 0.3$ eV (right). A band-gap is opened in the spectrum of bilayer graphene when the two graphene sheets have different potential energies defined by Δ. In addition, bilayer graphene has two high energy sub-bands beginning at $\epsilon > 0.4$ eV.

At such points, often referred to as van Hove singularities (vHS), correlated electronic states can occur due to an increased available phase space volume for the exchange of virtual quasi-particles. For example in the case of superconductivity, virtual phonons are responsible for the strength of the attractive force between the electrons in a Cooper pair and strongly depend on the DOS [36]. In general, for various complex materials with nontrivial correlated ground states, such as superconductivity, magnetism or charge density wave formation, it is believed that a high DOS and the nesting of the Fermi energy in a vHS are key for the understanding of these exotic phases [10].

Monolayer graphene

In the case of monolayer graphene the DOS can be calculated analytically from the nearest neighbors tight-binding band-structure as it was derived in the previous section. Here an exact analytical expression can be derived and is given by [11; 17] :

$$DOS(\epsilon) = \frac{4}{\pi^2}\frac{|\epsilon|}{\gamma_0^2}\frac{1}{\sqrt{Z_0}}\mathbf{F}\left(\frac{\pi}{2}, \sqrt{\frac{Z_1}{Z_0}}\right) \tag{1.13}$$

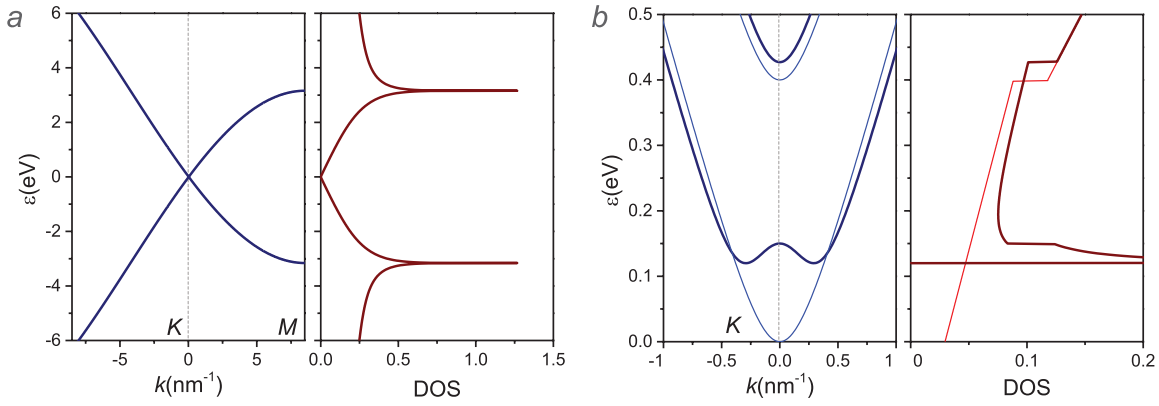

Figure 1.4: (a) Dispersion relation of monolayer graphene and the corresponding $DOS(\epsilon)$. The band-structure disperses linearly with energy around the K-point, with a linearly increasing DOS starting from zero energy. In proximity to the M-point the bands become flat resulting in a strong singular increase in the DOS, the vHS. (b) Low energy dispersion relation of bilayer graphene around the K-point for values of $\Delta = 0$ eV (thin line) and $\Delta = 0.3$ eV (thick line) and the corresponding $DOS(\epsilon)$. For finite Δ several flat band regions in the band-structure appear giving rise to non-monotonic jumps in the DOS. A further vHS appears at the onset energy of the high-energy sub-bands $\epsilon \sim 0.4$ eV. In contrast to monolayer graphene where the DOS at the K-point is zero, here, due to its curved band-structure at the band edge, the DOS has finite values.

where $\mathbf{F}\left(\frac{\pi}{2}, x\right)$ is the complete elliptical integral of the first kind with Z_0:

$$Z_0 = \begin{cases} \left(1 + |\frac{\epsilon}{\gamma_0}|\right)^2 - \frac{[(\epsilon/\gamma_0)^2-1]^2}{4}, & |\epsilon| \leq \gamma_0 \\ 4\frac{|\epsilon|}{\gamma_0}, & |\epsilon| \geq \gamma_0 \end{cases} \tag{1.14}$$

and vice versa for Z_1:

$$Z_1 = \begin{cases} 4\frac{|\epsilon|}{\gamma_0}, & |\epsilon| \leq \gamma_0 \\ \left(1 + |\frac{\epsilon}{\gamma_0}|\right)^2 - \frac{[(\epsilon/\gamma_0)^2-1]^2}{4}, & |\epsilon| \geq \gamma_0 \end{cases} \tag{1.15}$$

Fig. 1.4 (a) displays the DOS in Eq. 1.13 side-by-side with the energy spectrum. Being completely zero at the Dirac point, the DOS first increases linearly with energy but then scales much faster close to the M-point where it reaches a sharp maximum at $\epsilon = \gamma_0$ hence forming a vHS. The steep increase of the DOS in this point is a direct consequence of the

flattening of the bands when they approach the M-point, since it enhances the number of momentum states per given energy. Overall one can define two distinct points with non-monotonic behaviour of the DOS, the Dirac point with $\epsilon = 0$ eV and the vHS with $\epsilon = \gamma_0 \sim 3.16$ eV.

While being quite accurate for low energies, the nearest-neighbors tight-binding band-structure is not a good approximation for the higher energy band-relation. Although it resembles all the main characteristics of the experimentally obtained band-structure, as it was obtained by angle resolved photo-emission spectroscopy studies (ARPES) shown in Fig. 1.5 [9], the corresponding energy scales alter quite severely. Here the two valleys touch in the M-point at much lower energy than predicted $\epsilon = 1.5$ eV, with the flat band regions through the M-point being much flatter and much more extended, hence resulting in an even sharper vHS with higher maximal DOS values. The reasons for such a strong deviation of the experimental band-structure stem from in a strong renormalization of the energy spectrum due to the onset of strong electronic correlations which, in turn, could be caused by the high values of DOS. Therefore these findings further support that complex electronic states could be found in the vHS of single layer graphene and suggest that these could be potentially much more easily accessible than expected, since the lower onset energies directly translate into lower carrier densities that are needed to fill up the bands. Here the carrier density at the vHS are $n_{exp} \sim 5 \times 10^{14}\ cm^{-2}$ much lower than the theoretically predicted $n_{theor} \sim 1 \times 10^{15}\ cm^{-2}$.

Bilayer graphene

In general monolayer and bilayer graphene bands have very similar high energy properties, where in exact analogy to the monolayer case both, the low- and high-energy sub-bands follow a linear dispersion relation that becomes flatter close to the M-point where the two valleys merge. The low energy characteristics of the bilayer graphenes band-structure however, with a band-gap opening for $\Delta > 0$ eV, is strikingly different from the monolayer case. For this reason, we will skip the similar behaviour near the M-point, and will only work out the behaviour of the DOS at the low energy regime.

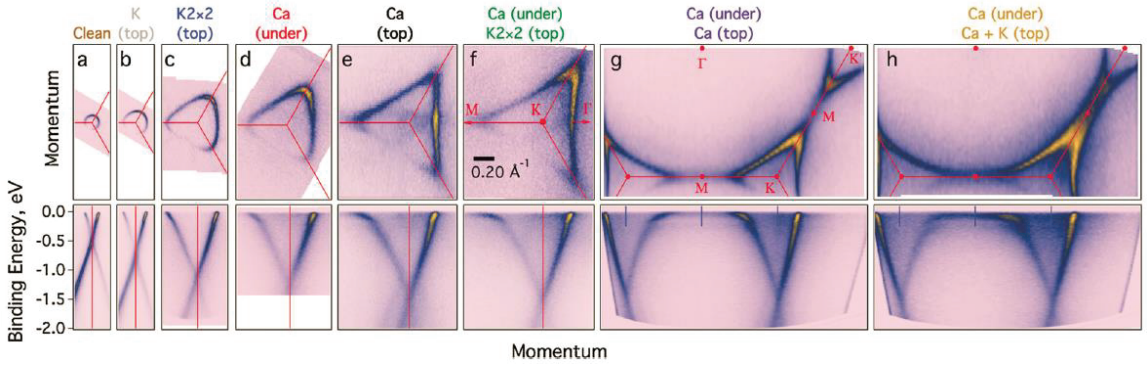

Figure 1.5: Doping dependence of the band-structure of monolayer graphene measured by angle resolved photo emission spectroscopy (ARPES). Here the carrier density of the graphene devices was varied by adsorption of evaporated positively charged ionic species, resulting in different values of the Fermi energy. Here the energies at which the two valley merge are $\epsilon_F \sim 1.5$ eV much lower than the $\epsilon_F \sim 3$ eV expected from the nearest-neighbor tight-binding approximation. Figure is taken from [9].

The *DOS* can be calculated from the low energy approximation of the band-structure around the K-points as it was derived in the previous section using the identity :

$$DOS(\epsilon, \Delta) = \frac{2k(\epsilon, \Delta)}{\pi \left(\frac{d\epsilon(k,\Delta)}{dk(\epsilon,\Delta)} \right)} \tag{1.16}$$

with the wave-vectors for the low- and high-energy sub-bands k_1 and k_2 being defined as :

$$k_1(\epsilon, \Delta) = \frac{1}{\hbar v_F} \sqrt{\frac{\Delta^2}{4} + \epsilon^2 + \frac{\sqrt{4\Delta^2\epsilon^2 + 4\gamma_0^2\epsilon^2 - \gamma_0^2\Delta^2}}{2}} \tag{1.17}$$

$$k_2(\epsilon, \Delta) = \frac{1}{\hbar v_F} \sqrt{\frac{\Delta^2}{4} + \epsilon^2 - \frac{\sqrt{4\Delta^2\epsilon^2 + 4\gamma_0^2\epsilon^2 - \gamma_0^2\Delta^2}}{2}} \tag{1.18}$$

resulting in the rather lengthy expressions for the *DOS* of the low- and high-energy sub-bands DOS_1 and DOS_2 :

$$DOS_1(\epsilon,\Delta) = \frac{1}{\pi h^2 v_F^2}\Theta_H\left(\epsilon-\epsilon_1\left(\frac{\Delta\sqrt{2\gamma_0^2+\Delta^2}}{hv_F},\Delta\right)\right)\left(2\epsilon+\frac{8\gamma_0^2\epsilon+8\Delta^2\epsilon}{\sqrt{4\Delta^2\epsilon^2+4\gamma_0^2\epsilon^2-\gamma_0^2\Delta^2}}\right)$$

$$-\frac{1}{\pi h^2 v_F^2}\Theta_H\left(\epsilon-\epsilon_1\left(\frac{\Delta\sqrt{2\gamma_0^2+\Delta^2}}{hv_F},\Delta\right)\right)\Theta_H(\epsilon_1(0,\Delta)-\epsilon)\left(2\epsilon-\frac{8\gamma_0^2\epsilon+8\Delta^2\epsilon}{\sqrt{4\Delta^2\epsilon^2+4\gamma_0^2\epsilon^2-\gamma_0^2\Delta^2}}\right) \tag{1.19}$$

$$DOS_2(\epsilon,\Delta) = \frac{1}{\pi h^2 v_F^2}\Theta_H(\epsilon-\epsilon_2(0,\Delta))\left(2\epsilon-\frac{8\gamma_0^2\epsilon+8\Delta^2\epsilon}{\sqrt{4\Delta^2\epsilon^2+4\gamma_0^2\epsilon^2-\gamma_0^2\Delta^2}}\right) \tag{1.20}$$

with Θ_H the Heaviside step function that is used to account for the singular points in the band-structure, and ϵ_1, ϵ_2 the low- and high-energy sub-band dispersions as obtained in the previous section.

The total $DOS(\epsilon,\Delta) = DOS_1(\epsilon,\Delta) + DOS_2(\epsilon,\Delta)$ is plotted in Fig. 1.4 (b) for different values of Δ side-by-side to the energy-spectrum. While for $\Delta = 0$ eV, starting from a finite value in the CNP the DOS increases linearly and exhibits a sharp non-monotonic jump at the onset of the high-energy sub-bands, for $\Delta > 0$ eV the $DOS(\epsilon)$ is immensely modified. Here, due to band-gap opening, the low-energy sub-bands have now the shape of a "Mexican hat" with two flat band regions. At the bottom ring of the Mexican hat, the DOS has very strong singularities forming additional vHSs. Similarly to the vHSs in monolayer graphene these vHSs have also attracted attention in the research community with various predictions stating the possibility of exotic electronic states.

1.3 Predictions of intrinsic superconductivity in graphene

Whenever a new material is discovered, one of the very first questions researchers address is whether or not this material could sustain intrinsic superconductivity (SC) at low temperatures and whether the SC order could be of an unusual kind. Ever since the discovery of graphene this question has kept hopes high for the potential discovery of SC in graphene and myriads of theoretical studies predicted unusual pairing mechanism resulting from graphenes chiral Dirac electrons and pseudo-spin properties [8; 9; 10; 37]. Furthermore, as many graphene derived materials like graphite intercalation compounds (GIC's) [38; 39; 40; 41; 42], potassium doped fullerene compounds Rb_3C_{60} [43] and, more controversially, carbon-nanotube bundles [44] showed SC properties with T_c's of up to 28 K, the question arises whether the graphene planes in these materials could have a major role in the occurrence of SC and whether single layer graphene, when subjected to similar conditions, could sustain a similar form of SC pairing by itself [37]. A potential discovery of superconductivity in graphene could therefore shed some light on the SC mechanisms in other carbon compounds. Yet, in the year 2014 graphene has still not shown signs of intrinsic SC. Why not?

In order to try to address this question without giving a full account of all the different theoretical predictions, we first give a back-of-the-envelope reason why, and under which conditions, SC could be feasible in graphene. Here we assume conventional electron-phonon interaction mediated SC and employ the typical formula for T_c from the BCS theory, the McMillan formula [36] :

$$T_c = 1.14\Theta_D \exp\left(\frac{-2}{V_0 DOS}\right) \tag{1.21}$$

with Θ_D the Debye temperature and V_0 the electron-phonon coupling potential.

As due to graphenes extreme in plane strength $\Theta_D \simeq 2300$ K is almost an order of magnitude higher than Θ_D in typical metals, the existence of SC in graphene should appear

to be rather likely. Though, as the other two parameters V_0 and DOS are entering the formula exponentially, these have much more weight and too small values of either V_0 or DOS would result in extremely low T_c's that would be impossible to explore experimentally. Here, while V_0 is relatively high, owing to a reasonably strong electron-phonon coupling term $\lambda \sim 0.2$ [42], the DOS is zero in the Dirac point and vanishingly small in its vicinity. The small DOS's could be therefore the main reason why SC was not observed close to the Dirac point, albeit a lot of experimental activities searching for SC down to milli-Kelvin temperatures.

At higher doping levels however the DOS is much larger and reaches extremely high values in the vHSs. In this regime all three parameters that enter the McMillan formula would be relatively high and could hence result in high T_c values. Indeed most theoretical predictions of SC in graphene are made for the regime at extremely high doping levels around the vHSs [8; 9; 10]. However, the experimental phase space in this regime remains almost completely unexplored since typical gating techniques do not allow to exceed Fermi energies beyond $\epsilon_F \sim 0.3$ eV and hence to accesses this regime.

1.3.1 Superconductivity in graphite intercalation compounds

Graphite intercalation compounds (GIC's) are a very well studied family of materials based on highly oriented pyrolytic graphite (HOPG) with crystallographically oriented layers of ions arranged in-between the graphene sheets. Here the intercalated ionic species are most commonly small alkali and rare earth ions like Li^+, Ca^{2+} arranged in a XC_6 stoichiometry where X represents metallic ions, but also much larger ions like K^+ or Cs^+ can be successfully intercalated in a XC_8 stoichiometry [38]. Depending on the number of graphene layers intercalated in-between two consecutive ionic layers one can define a stage number to the resulting compound, with for example stage 1 and stage 3 corresponding to one or three graphene planes in-between two ionic planes, respectively (Fig. 1.6 (a)).

Many stage 1 compounds like KC_8, YbC_6 and most recently and prominently CaC_6 [41; 42] were found to be superconductors with relatively high T_c's of 0.5 K, 6 K and 11.5 K

respectively. Although these observations are already several decades old, the exact nature and origin of SC in these compounds is still a big debate in the community. There exists a big dispute whether the graphene derived π-bands have a prominent role in the nucleation of the SC or whether it could be solely explained by the 3D spherically symmetric electronic bands derived from the intercalated ions [39; 40; 41; 42].

Though, with several recent experimental studies including angle resolved photo emission spectroscopy (ARPES) [41; 42] and scanning tunneling microscopy (STM) which were performed on these materials for the first time, the focus towards the explanation of the SC mechanism seems to shift in favor to the graphene derived π-bands. Here specifically the ARPES results are very revealing as shown in Fig. 1.6 (b). It turns out that the band-structure of CaC_6 is essentially identical to the band-structure of monolayer graphene with a strongly elevated Fermi energy. This result suggests three major effects of the intercalate layers on the graphene : 1. The ionic planes increase the spacing between the graphene layers d, in the case of CaC_6 from $d = 3.35$ $\mathring{A}$ to $d = 4.52$ $\mathring{A}$, resulting in an effective electronic decoupling of these. Without direct electronic hopping between the graphene planes the band-structure is equivalent to that of monolayer graphene; 2. The positively charged Ca^{2+} ions dope the graphene planes and elevate their Fermi energy to extremely high values in close proximity to the vHS in the M-points with their high DOS. Here the charge transfer per ion is not unity and does vary for the various GIC's with the highest percentages of $\sim 60 - 70\%$ typically obtained for CaC_6; 3. As the intercalated layers arrange in crystallographic order they give rise to new phonon branches which in turn can couple to the π-band electrons. As it was also inferred from a more detailed analysis of the ARPES data of CaC_6 [42], these additional phonons lead to an overall enhancement of the electron-phonon coupling parameter λ from ~ 0.2 in pure graphite to ~ 0.85 in CaC_6.

Overall these findings bring the graphene derived π-bands into the focus and suggest that the occurrence of SC in GIC's could potentially be explained by very similar arguments that were given in the previous subsection. Here, assuming conventional BCS superconductivity and the validity of the McMillan formula, the high DOS values paired with the enhanced

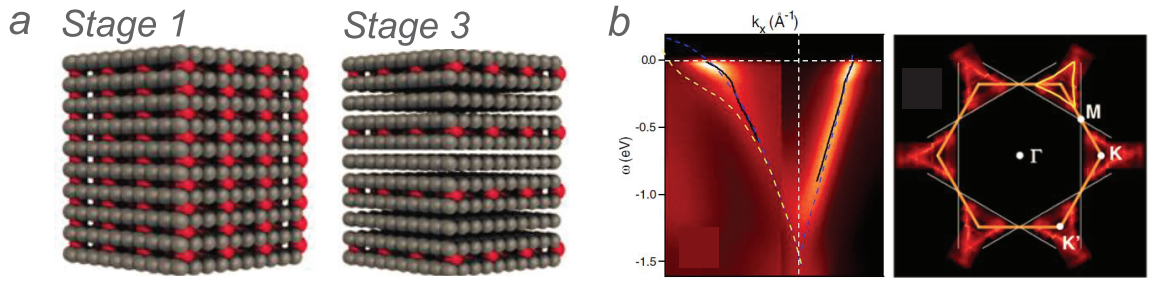

Figure 1.6: (a) Schematics of graphite intercalation compounds with different stages of intercalation. The graphene planes (black) are separated by crystallographically arranged layers of ions (red). Here the stage number corresponds to the number of graphene layers in-between two ionic layers. (b) Electronic band-structure of the stage 1 GIC CaC_6 as measured by angle resolved photon emission spectroscopy (ARPES). In contrast to the band-structure of graphite, the dispersion relation of CaC_6 is equivalent to the band-structure of highly doped monolayer graphene. Figure (b) is taken from [42].

electron-phonon coupling parameter λ could be the key factors for the relatively high T_c observed in CaC_6. In general, by extracting the Fermi energies and λ's from ARPES data for various GIC's, it was shown that the values of their corresponding T_c's have indeed certain trends towards higher DOS and λ's [41].

It naturally arises the question whether under similar conditions monolayer graphene could also sustain similar SC. Now indeed a very similar Fermi energy and DOS can be achieved in graphene with novel electrolytic gates, which in addition could also be used to adsorb different ionic species onto the graphene to potentially increase λ. In general the strong tunability of monolayer graphene could allow to even further vary these parameters and, hypothetically, to obtain even higher T_c's.

1.4 Superconducting proximity effect induced electronic correlations in graphene

While intrinsic SC has not been observed in graphene yet, it is though possible to induce SC correlations into graphene via proximity effect, by bringing it into electrical contact with an intrinsic SC. Here, although not thermodynamically stable in a normal metal (N), Cooper pairs can leak in from the SC and form phase-correlated electron-hole states [45; 46; 36]. The key for understanding this effect is a process called Andreev reflection (AR) which occurs when an electron from N is incident on a SC [47]. Since the electron can only continue to propagate in the SC as a Cooper pair it has to bind with another electron, though due to charge conservation, this process is only possible if at the same time a hole is created in the normal metal. This hole is retro-reflected back into N with the exactly opposite momentum of the incident electron. This electron and the reflected hole inherit the phase-coherent properties of the electrons in Cooper pairs and form phase-coherent electron-hole quasi-particles in the normal metal, the so called Andreev states [46].

In general, the proximity effect in graphene can be of specific interest as it combines AR processes that are described by the Bogoliubov-de Gennes equations (BdG) with graphenes Dirac equation, so coupling two seemingly completely unrelated fields, relativistic physics and the physics of condensed collective ground states. This combination can lead to the yet not experimentally observed prediction of specular AR's [19; 48], an exotic type of AR's where unlike for the case of retro-reflection, the hole is reflected back at an angle to the momentum of the incident electron.

Moreover, owing to its strict two dimensionality and its ballistic transport properties, graphene is also an excellent platform to study the effect of high magnetic fields on AR's, a long time proposed but experimentally almost not studied field in mesoscopic condensed matter physics where an interesting interplay between the quantum Hall effect and the AR processes is expected [29; 49; 50; 51]. While similarly these experiments could also be performed with other ballistic 2D electron gases for example in semiconductor quantum well

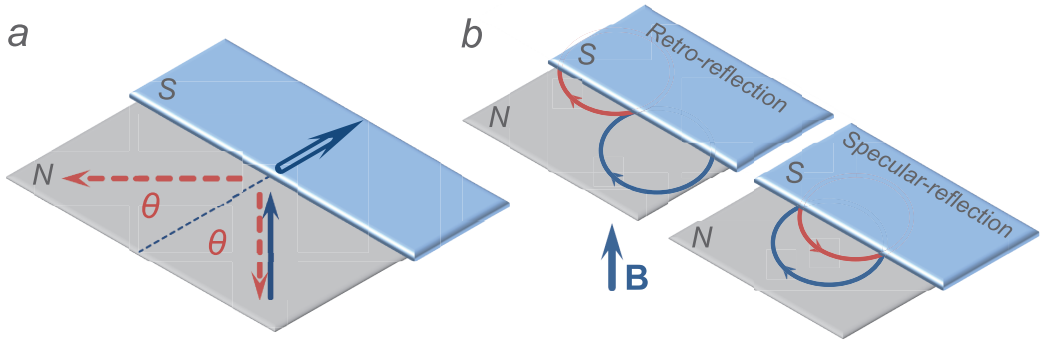

Figure 1.7: (a) Schematic of retro and specular Andreev reflections. While the retro-reflected hole is reflected back in exactly the same direction as the incident electron, the specular-reflected hole is reflected at an angle, equal to the angle of incidence. (b) Schematics of retro and specular ARs in perpendicular magnetic fields. The cyclotron motion of the retro-reflected hole is directed in the same direction as the incident electron, resulting in propagation along the edge. The specular-reflected holes cyclotron motion is counter-directed to the electron, resulting in localized states.

structures, such as GaAs and InAs [52; 53; 54; 55; 56; 57; 58] it can be typically very challenging to engineer Ohmic electronic interfaces and transparent contacts, a prerequisite to have a high probability of Andreev reflections at the SN interface. As will be discussed later on, being a semi-metal, graphene can have advantages to these semiconducting materials and the creation of transparent SN interfaces could be less challenging.

1.4.1 Andreev reflections from the BKT theory

A widely used theoretical framework to calculate the conductance across superconductor-to-normal (SN) junctions is the BKT theory named after Blonder, Tinkham and Kalpwijk [18]. This one dimensional conduction model assumes an infinite SC condensate, that is described by the Bogoliubov-de Gennes equations (BdG) [36], which is in electrical contact with an infinite normal metal, that typically can be just described by a free electron Hamiltonian $H = \frac{\hbar^2}{2m}\frac{d}{dx^2}$. We can write down the BdG equations, which are a set of coupled Schrödinger equations [18; 46; 45] :

$$\begin{aligned} E\psi(x) &= -(H + \epsilon_F)u(x) + \Delta(x)v(x) \\ E\psi(x) &= (H + \epsilon_F)v(x) + \Delta(x)u(x) \end{aligned} \tag{1.22}$$

with $\Delta(x)$ the spatially varying SC pairing potential and μ the chemical potential.

Together with the two component wave-function ψ, which is given by its electron-like u ($k > k_F$) and hole-like v ($k < k_F$) components that are coupled through the relation $u^2 = 1 - v^2 = \frac{1}{2}(1 + \sqrt{E^2 - \Delta^2}/E)$ and with the energy E and the macroscopic phase of the SC condensate ϕ :

$$\psi = \begin{pmatrix} u \\ v \end{pmatrix} e^{\frac{2iEt}{\hbar} + \phi} \tag{1.23}$$

we obtain four types of quasi-particle wave-functions :

$$\psi_{\pm k^+}(x) = \begin{pmatrix} u \\ v \end{pmatrix} e^{\pm ik^+ x} \quad and \quad \psi_{\pm k^+}(x) = \begin{pmatrix} u \\ v \end{pmatrix} e^{\pm ik^+ x} \tag{1.24}$$

Here the SN interface can be modeled as an infinitely sharp tunneling barrier that can be described by a Delta function $V(x) = H\delta(x)$ with potential height H and is typically described by the dimensionless parameter $Z = H/\hbar v_F$, where $\hbar$ is the Planck's constant and v_F the Fermi velocity of the normal metal. Boundary conditions demand the continuity of the wave-functions on both the S and N sides $\psi_S(0) = \psi_N(0)$, and in view of the δ-potential we have to set $\hbar/2m(\psi_S^{'}(0) - \psi_N^{'}(0)) = H\psi(0)$ as well. Taking these condition into account one can distinguish three types of waves, the incident wave ψ_{inc}, the reflected wave ψ_{ref} and the transmitted wave ψ_{trans}, which can be expressed by :

$$\psi_{inc}(x) = \begin{pmatrix} 1 \\ 0 \end{pmatrix} e^{iq^+ x} \quad ; \quad \psi_{ref}(x) = a \begin{pmatrix} 0 \\ 1 \end{pmatrix} e^{iq^- x} + b \begin{pmatrix} 1 \\ 0 \end{pmatrix} e^{-iq^+ x} \tag{1.25}$$

$$\psi_{trans}(x) = c \begin{pmatrix} u \\ v \end{pmatrix} e^{ik^- x} + d \begin{pmatrix} u \\ v \end{pmatrix} e^{-} ik^+ x \tag{1.26}$$

where the dispersion relations for the momentum inside and outside the SC are $\hbar k^{\pm} = \sqrt{2m(\mu \pm \sqrt{E^2 - \Delta^2})}$ and $\hbar q^{\pm} = \sqrt{2m(\mu \pm E)}$.

From the above expression for the reflected wave ψ_{ref} we can see that the incident electron can be either reflected as a hole with an amplitude a or as an electron with an amplitude b. Overall these two processes can be defined as AR's and the normal back-scattering of the electron, respectively. With the parameter $\gamma = u^2 + (u^2 - v^2)Z^2$ the probabilities for these scattering processes result in :

$$A = |a|^2 = \left(\frac{uv}{\gamma}\right)^2 \qquad B = |b|^2 = \left(\frac{(u^2 - v^2)(Z^2 + iZ)}{\gamma}\right)^2 \tag{1.27}$$

$$C = |c|^2 = \left(\frac{u(1 - iZ)}{\gamma}\right)^2 \qquad D = |d|^2 = \left(\frac{ivZ}{\gamma}\right)^2 \tag{1.28}$$

As u and v are energy-dependent, the resulting scattering probabilities also scale with E and hence can be probed by changing V_{sn}, the voltage difference between S and N. Fig. 1.8 (a) demonstrates these coefficients as a function of V_{sn} for different Z-factors. For $Z = 0$, $A = 1$, hence only AR can take place for $eV_{sn} < \Delta$, with A decaying fast for higher V_{sn}. For $Z > 0$ however, A is severely reduced with now B, the normal reflection processes, becoming more probable.

The total current across the junction is just the sum of the transmission coefficients over all the modes, and since only the probabilities for AR's A and back-scattering B affect the conduction properties across the junction, the current-voltage characteristics $I - V_{sn}$ can be written with the conductance above T_c defined as G_0 :

$$I(V_{sn}) = \frac{G_0}{e} \int_0^{\infty} dE(f(E) - f(E + eV_{sn}))(1 + A(E) - B(E)) \tag{1.29}$$

with the Fermi-Dirac distribution $f(E) = (e^{(E-\mu)/kT} + 1)^{-1}$ to account for temperature smearing of the Fermi energy.

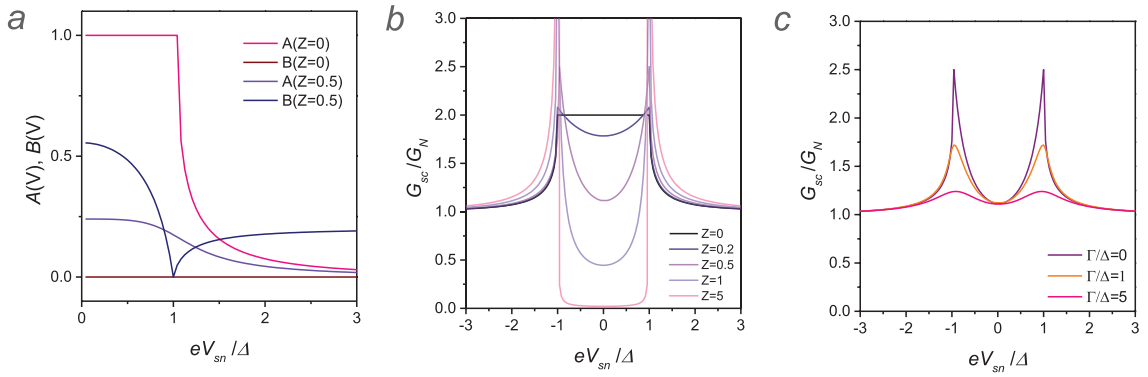

Figure 1.8: (a) Probabilities for Andreev reflections A and back-scattering processes B vs. the voltage drop across the SN interface V_{sn} for different tunnel barrier strengths Z. While A is relatively large for $eV_{sn} < \Delta$ it decays away quickly for larger V_{sn}, and while $B = 0$ for $Z = 0$ it becomes larger for $Z > 0$. (b) Normalized differential conductance G_S/G_N vs. V_{sn} for different Z. As $A = 1$ and $B = 0$ for $Z = 0$ in the voltage range $eV_{sn} < \Delta$, the conductance is doubled, though when $Z > 0$ and B becomes sizeable, G_S/G_N is strongly decreased around $V_{sn} = 0$ V, overall resulting in a characteristic conductance double-peak shape that is marking the SC gap Δ. (c) Finite quasi-particle life-times expressed by the parameter Γ dramatically broaden and reduce the sharp double-peak features.

As it is often more relevant for experimental measurements, we can now introduce the normalized differential conductance G_S/G_N, which is the ratio between the differential conductance $G_S = dI/dV_{sn}$(T= 0 K) below and $G_N = G_0$ above T_c :

$$\frac{G_S}{G_N}(V_{sn}) = \frac{1}{G_0}\frac{dI}{dV_{sn}} = (1 + A(eV_{sn}) - B(eV_{sn})) \tag{1.30}$$

It is directly evident from Eq. 1.30 that where-as A is effectively increasing the conductance, B is reducing it. The resulting G_S/G_N vs. V_{sn} curves for different Z are plotted in Fig. 1.8 (b), resulting in the typical Z-dependent conductance double-peak curves, with the voltage positions of the peaks marking the SC gap $eV_{sn} \sim \Delta$.

In general the BKT model is a gross approximation, as it does not take into account possible differences of the Fermi momenta in the two different materials and does not account for inelastic scattering processes typically occurring at the SN interfaces or in the materials itself. Though it provides an initial framework, that in spite of its simplicity, accounts for the

most striking transport properties across SN interfaces, and specifically well approximates the effect of AR's on the junctions conductivity.

Additionally, as it is now the wide understanding in the field of SC proximity effect, during the AR process the incident electron and the reflected hole form a phase-coherent Andreev state [46]. However, as in any realistic system one has to account for disorder, temperature and inelastic scattering processes, these can cause the Andreev states to decoher over very short length scales hence resulting in very short lifetimes [45; 59]. To phenomenologically account for the finite life-times $\Delta\tau$, using Heisenberg's uncertainty principle $\Delta E \Delta\tau > \hbar$, one can introduce an effective energy-broadening term Γ that enters the BKT theory by replacing E with $(E - i\Gamma)$. The effect of finite quasi-particle life-times can be seen in Fig. 1.8 (c) leading to an overall broadening and reduction of the typical conductance double-peak shape.

1.4.2 Magnetic field dependent Andreev reflections

Electrically coupling graphene to a type-II SC with relatively high upper critical fields H_{c2} allows to study the effect of magnetic fields on the ARs. In general, when AR's are taking place in B-fields, both the injected electron and the reflected hole are bend onto cyclotron orbits. Here, as has been shown in the previous section, in a typical retro-reflection process the electrons and holes cyclotron motion rotates in the same direction, so forcing these to spatially separate, with the exact opposite happening for specular-reflection, where the electrons and holes rotate in opposite directions.

Employing the ideal 2D nature and ballistic transport properties of graphene, the above discussed peculiarities can be studied in simple focusing experiments. For specific values of B-fields electrons can be injected onto a SC with the reflected holes being detected by a symmetrically arranged collection electrode (Fig. 1.9 (a) and (b)). Depending on whether the reflected holes are retro- or specular-reflected the measured current on the collection electrode would differ substantially, since while a retro-reflected hole would be focused on the collection electrode, a specular-reflected hole would be focused back onto the injector

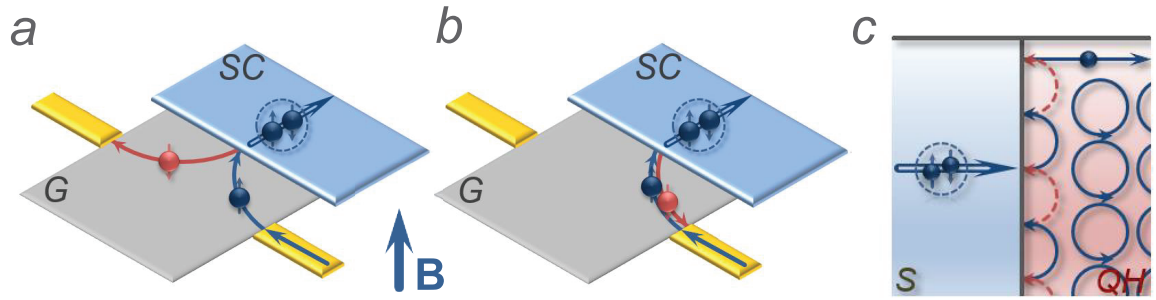

Figure 1.9: (a) and (b) Electron focusing setup where electrons are injected on a SC under a small B-field. Here, whether the hole is retro- (a) or specular-reflected (b) can be detected by a symmetrically arranged collection electrode. (c) Andreev bound states (ABS) of skipping electron and hole orbits are formed along the SN interface if graphene is in the quantum Hall regime. In ultra clean samples the ABS can retain phase-coherence over several scattering cycles forming propagating Andreev edge states.

electrode [19]. Furthermore, the high probability of specular ARs at the Dirac point, and vice versa the high probability of retro ARs away from it would allow to continuously tune these probabilities with a gate. Due to time reversal symmetry, this process is in all generality equivalent to the crossed AR or Cooper pair splitting process [60; 61], a process that aims to study the dissipation process of a Cooper pair in the normal metal. Here the electron-hole pairs, that are created by the injection of a Cooper pair into N, are spatially split apart by the B-field.

In the limit of strong magnetic fields where the cyclotron orbits are extremely small, a retro-reflected hole is bent back onto the SC with the then retro-reflected electron being bent back onto it again. The B-fields hence bind the electron-hole pairs to the SN interface effectively defining these as Andreev bound states (ABS) [29; 49; 50]. The formation of the ABS at the SN interface can severely modify its conduction properties, where in the ultra clean limit when the electron-hole pairs can retain phase-coherence even after several ARs a phase-coherent propagating edge state of alternating electron and hole orbits is created, the so-called Andreev edge state (AES) (Fig. 1.9 (c)) [51].

Chapter 2

Strong carrier density modulation with electrolytic gates

2.1 Electrolytic gating

2.1.1 Electric field effect in material science - an overview

The electric field effect (EFE) is a very powerful technique in the field of low dimensional condensed matter physics as it allows to alter the physical properties of various low dimensional material classes by electrostatically changing its carrier density n by inducing a perpendicular electric field. This technique can be applied to a wide variety of materials like metallic and semiconducting thin films [62], two dimensional electron gases such as in GaAs hetero-structures and graphene [2], and one dimensional systems like nanowires or carbon nanotubes. Typically the thicknesses of the materials are chosen such that these are thinner than the Debey screening length λ_D, which is typically in the order of 10 nm, guaranteeing that the electric field can penetrate the whole sample. Since by employing the EFE n can be altered without introduction of chemical dopants, detailed n-dependent physical properties can be studied in a clean way without introducing additional disorder into the system as it is the case for chemical doping techniques. In general, this technique also allows to study n-dependent properties of materials where chemical doping proved to

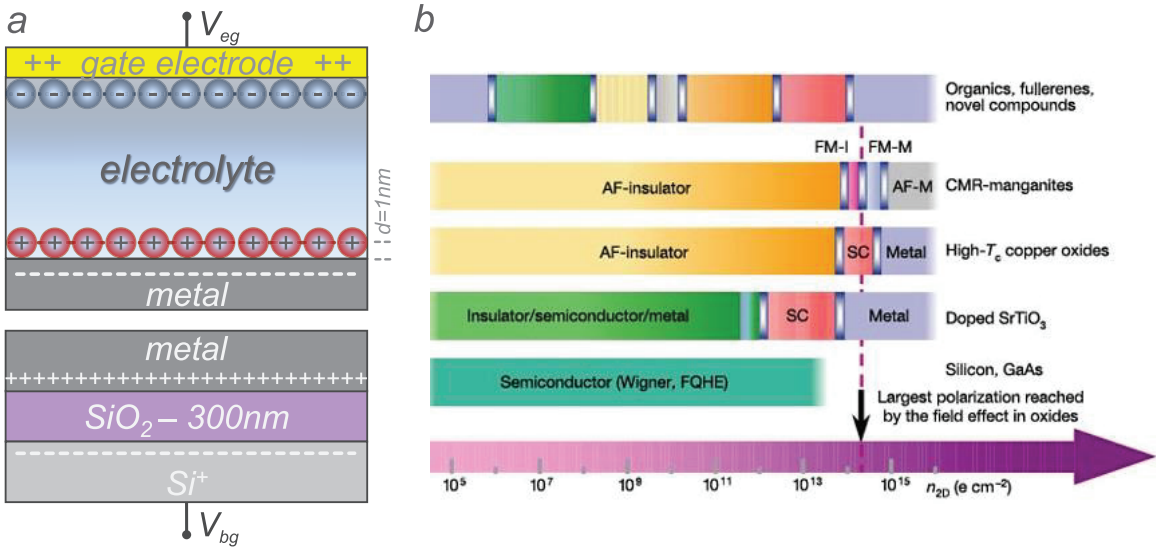

Figure 2.1: (a) Schematic of the electrolytic gate (top) and the typical silicon based back gates (bottom). The close proximity of the Debey layers of $d \sim 1$ nm to the samples surface in the electrolytic gates results in two orders of magnitude higher capacitances as compared to the back gates with their $d = 300$ nm gate dielectrics. (b) Overview of n-dependent physical properties for various material groups as taken from [63].

be very challenging.

In many different classes of materials not only simple physical properties are strongly n-dependent, like f.e. the conductance in semi-conductors, but also complex phase-transition like for example the anti-ferromagnetic (AFM) to high-temperature superconductor transitions in cuprates [63; 24]. The carrier density ranges needed to induce these changes can vary dramatically from material to material. Fig 2.1 (b) shows an overview of different classes of materials and the corresponding electronic phases vs. n. Here, whereas some phase transition can be induced by adding relatively low $n \sim 10^{12}$ cm^{-2} like in the case of the insulator-superconductor transition in the complex oxide $SrTiO_3$, many other transitions can only take place by inducing much higher $n \sim 10^{15}$ cm^{-2}. As it was discussed previously, in the case of graphene the expected n to reach the vHSs in the M-points are $n \sim 5 \times 10^{14}$ cm^2.

Traditionally the EFE is induced by semi-conductor-based field effect transistor devices with rather thick gate dielectrics, the commonly used 300 nm thick thermally grown SiO_2

backed by a gate electrode made of highly doped silicon - the so-called "back-gates" (Fig. 2.1 (a) bottom) [2]. These gates can be treated as parallel plate capacitors and allow to induce n only up to $n < 5 \times 10^{12}$ cm^{-2}. Here, the limiting factors to achieve higher n are mainly the low capacitances $C \sim 10$ nFcm^{-2} due to the very thick gate dielectrics and the dielectric breakdown of the SiO_2 when gate voltages of $V_{bg} > 60$V are applied, resulting in a discharge across the capacitor. Whereas it is in general possible to grow thinner gate dielectrics it can result in proportionally reduced dielectric breakdown voltages hence not allowing to increase maximal n.

A recently developed alternative to such gates are electrolytic gates [25; 26; 20; 21; 24]. As is shown in Fig 2.1 (a) an electrolytic gate employs an electrolyte solution that is covering the sample. By applying a voltage V_{eg} to a gate electrode charged ionic layers accumulate in direct proximity of the sample. These Debey layers are typically only a distance of $d \sim 1$ nm away from the direct sample surface and therefore result in much higher capacitances of $C \sim 5$ μFcm^{-2}. Here, just like for the dielectric gates, the limiting factor to achieve even higher n is the onset of leakage currents, the Faradaic currents [64], from the gated material into the electrolyte, which are generally accompanied by electrochemical reactions on the sample. As these occur at voltages of about $V_{eg} = 5$ V, maximal n reported for electrolyte gates are in the range of $n \sim 10^{15}$ cm^{-2} allowing to approach many of the transition described in Fig. 2.1 (b) [20; 21].

2.1.2 Solid polymer electrolytes and ionic liquids

In order to induce strong modulation of n with electrolytic gates several conditions concerning the gated material, the electrolyte itself and the interaction between the two have to be fulfilled [20; 26]. The gated material has to have an atomically sharp surface which is typically achieved for thin films grown by molecular beam epitaxy (MBE) or for mechanically exfoliated van der Waals (vdW) materials. In general, considering the spatial proximity of the Debye layers to the surface of only $d \sim 1$ nm, a surface roughness greater than this value would result in very strong inhomogeneities of n, a highly undesirable effect

that would effectively deplete the surface into charged puddles. Furthermore the material and the electrolyte should be chemically inert to one another as any chemical reactions can severely modify the surfaces properties, potentially resulting in insulating sacrificial layers that would severely reduce C. Additionally it is crucial to have a large voltage range ΔV_{eg} where no electrochemical reactions between the electrolyte and the material occur. As such reactions are accompanied with Faradaic currents across the interface these hinder the accumulation of additional charge in the sample, and as these are intimately linked to the chemical decomposition of the material, these lead to irreversible degradation of the materials surface. Therefore, as many electrolytes have similar C, a large ΔV_{eg} is the crucial factor for achieving highest possible n,

Although there are seemingly countless electrolytic systems, so far only very few have been shown to work well with low dimensional condensed matter systems. These are the solid polymer electrolyte gates and the ionic liquids. Although very similar, these two kinds of electrolytes can differ significantly for different purposes and when applied to different materials.

Solid polymer electrolytes

This electrolyte is very versatile and simple and is being used in many different commercially available products, most prominently in lithium ion batteries. The solid polymer electrolyte consists of the polymer poly(ethylene)oxide (PEO) and the salt lithium perchlorate ($LiClO_4$), although many other salts and ionic species are compatible with it as well [25; 26]. The PEO acts as a solvent to $LiClO_4$ separating it into positively Li^+ and negatively ClO_4^- charged ions. As is shown in Fig. 2.2 (a) the microscopic structure of the resulting electrolyte is such, that the PEO chains wrap around the Li^+ ions establishing van der Waals bonds between the Li^+ and the oxygen atoms in the PEO chain. Such wrapping is very advantageous as it protects the gated material from the highly reactive Li^+ ions and so dramatically enhances the ΔV_{eg} ranges.

The ions in this electrolyte are mobile down to a temperature of about 290 K, the freezing point of the electrolyte. It is very viscous at room temperature, typically referred to as being

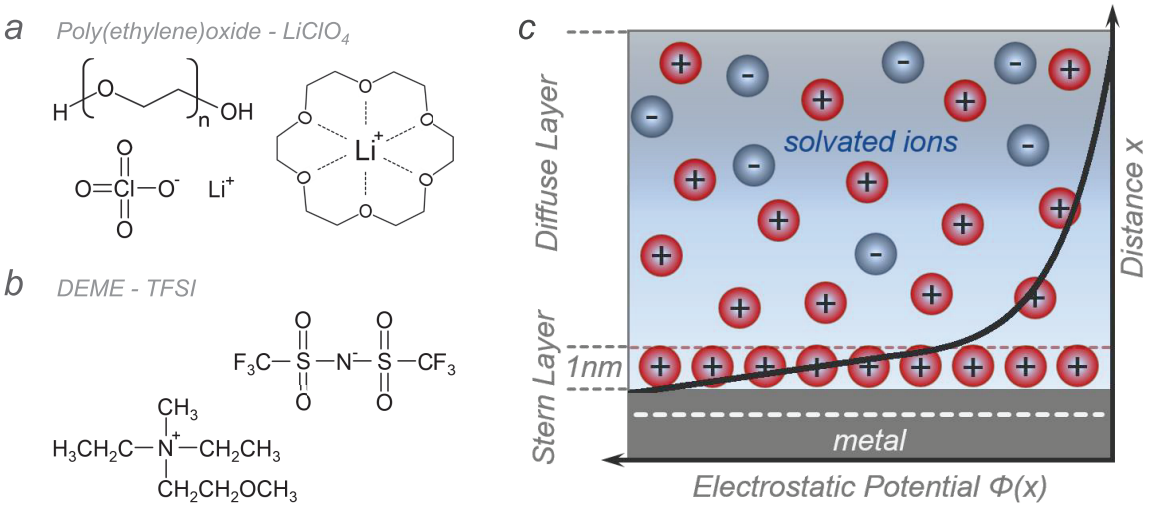

Figure 2.2: (a) Chemical composition of the solid polymer electrolyte based on PEO and $LiClO_4$. PEO chains wrap around the dissolved Li^+ ions, hence acting as a protection layer between the sample and the highly reactive Li^+ ions. (b) Chemical composition of the ionic liquid DEME-TFSI. (c) Schematic of the Stern-Gouy-Chapman electronic double layer (EDL) with the spatially varying electrostatic potential $\Phi(x)$. Due to adsorbed ions at the interface that form the so-called Stern layer, $\Phi(x)$ scales linearly in proximity to the interface. Away from it the ions are solvated and due to their thermodynamic distribution $\Phi(x)$ scales exponentially.

solid, which has great experimental advantages especially when the measurement setup is confined to very tight spaces such as low temperature cryostats and optical chambers. Here the electrolyte can be deposited on-chip by spin-coating, allowing to avoid the typical liquid cell setups needed for liquid electrolytes.

This electrolyte works well with chemically non-reactive materials such as graphene, graphite and some stable complex oxide compounds such as strontium titanate $SrTiO_3$. Though, due to the reactive nature of the Li^+ ions, for materials known for their chemical instability such as the cuprates, it was found to almost instantly distort their surfaces. In addition, the presence of Li^+ ions, the smallest ions in nature, has also proven to be very advantageous, as here besides the electrostatic gating, adsorption and intercalation processes can be reversibly induced when voltages beyond ΔV_{eg} are applied. For chemically stable materials such as graphene or graphite these additionally adsorbed ions can help to induce additional n into the material.

Ionic liquids

In contrast to the solid polymer electrolyte, the ionic liquid DEME-TFSI (Fig. 2.2 (b)) [20; 21] is solvent free and can be described as a molten salt of large ionic molecules. Here, similarly to the polymer electrolyte, the ions charge is localized in the center of the molecules and allows to avoid direct contact with the sample surface. As these ions do not contain highly reactive species like Li^+ the ΔV_{eg} ranges can be quite large and can be even further increased since the ions are mobile down to much lower temperatures of 220 K where many electrochemical reactions are suppressed.

Due to its chemical stability the ionic liquids can be combined with almost any material without inducing strong chemical degradations. So far these gates showed the strongest n modulations for any gate, reaching values of $n \sim 10^{15}$ cm^{-2}. One mysterious and rather unexplained disadvantage of the ionic liquid gates is though that C seems to decrease as the gated material becomes thinner, ultimately resulting in very low C for single layer crystals such as graphene.

2.1.3 Electric double layer model for metal-electrolyte interfaces

The microscopic nature of the interfacial region between an electrolyte and a metal surface is still an active area of research today, however rather simple electrostatic models can be addressed that allow to shed light on the structure and the ionic distribution at the interface. Here we derive a classical model in the field, the Stern-Gouy-Chapman electronic double layer (EDL) model [64]. This model has certain limitations, as it assumes only Coulomb interactions between the ions, constant permittivity for the solvent throughout the double layer, neglects the molecular nature of the solvent and the viscosity of the fluid (which can be crucial for a solid polymer electrolyte). Still it can provide deep insights in the properties of the EDL and can be used to obtain quite accurate predictions for the capacitance C of the electrolyte.

As is demonstrated in Fig. 2.2 (b), this model is based on the thermodynamic Gouy-Chapman model, that is based on the assumption of a diffuse layer of ions close to the metal

interface that can be described by a Poisson-Boltzmann equation. In this layer the ions are fully solvated with excess charge concentrations increasing in proximity to the interface, so giving rise to an exponential increase of the electrostatic potential $\Phi(x)$. Additionally, as ionic species tend to adsorb directly at the surface one has to account for the compact, unsolvable ionic layers at the interface, that give rise to a steep linear increase of $\Phi(x)$.

We can write the Poisson equation for the spatially varying electric potential $\Phi(\vec{r})$:

$$\nabla^2\Phi(\vec{r}) = -\frac{\rho(\vec{r})}{\varepsilon} \tag{2.1}$$

with ε the dielectric constant of the medium, $\rho(\vec{r}) = \sum_i N_i(\vec{r}) z_i e$ the volume charge density, with e the electronic charge, the valence of the ions z_i and the number of ions $N_i(\vec{r})$ for the different ionic species with index i.

Assuming a Boltzmann distribution of the ions along the electrostatic potential, that starts a distance d away from the metal surface to account for the Stern layer of adsorbed ions, $N_i(\vec{r})$ has the following spatial dependence :

$$N_i(\vec{r}) = N_{i0} \exp\left(-\frac{z_i e(\Phi(\vec{r}) - \Phi(\vec{d}))}{kT}\right) \tag{2.2}$$

with N_{io} the number of ions at $\vec{r} = \vec{d}$. This formula can be simplified for the case of a two dimensional boundary conditions (here a $2D$ metal interface) and taking only one ionic specie into account. We get the Boltzmann-Poisson equation :

$$\frac{d^2\Phi(x)}{dx^2} = \frac{2N_0 ze}{\varepsilon} \sinh\left(\frac{ze\Phi(d)}{2kT}\right) = -\frac{\rho(x)}{\varepsilon} \tag{2.3}$$

The charge density in the diffuse layer σ_d is directly related to $\rho(x)$:

$$\sigma_d = \int_d^\infty \rho(x)dx = \int_d^\infty \varepsilon \frac{d^2\Phi(x)}{dx^2} dx = \varepsilon \left[\frac{d\Phi(x)}{dx}\right]_d^\infty \tag{2.4}$$

and with the integration of $\int \frac{d}{dx}\left(\frac{d\Phi(x)}{dx}\right)dx = \int \frac{4N_0ze}{\varepsilon}\sinh\left(\frac{ze\Phi(x)}{2kT}\right)d\Phi$ results in :

$$\frac{d\Phi(x)}{dx} = \frac{-2\kappa kT}{ze}\sinh\left(\frac{ze\Phi(x)}{2kT}\right) \tag{2.5}$$

introducing here the Debye-Hückel parameter $\kappa = \sqrt{\frac{2N_AIe^2}{\varepsilon kT}}$, with Avogadros number N_A, the ionic strength $I = \frac{1}{2}\sum c_i z_i^2$ representing the concentration of all ions present in the solution (here c_i is the molar concentration), and finally can be written as :

$$\sigma_d = \frac{-2\varepsilon\kappa kT}{ze}\sinh\left(\frac{ze\Phi(d)}{2kT}\right) \tag{2.6}$$

The resulting total differential capacitance of the so modeled interface is therefore :

$$C_d = -\frac{d\sigma_d}{d\Phi(d)} = \varepsilon\kappa\cosh\left(\frac{ze\Phi(d)}{2kT}\right) \tag{2.7}$$

The addition of a Stern layer (see Fig. 2.2 (b)) to the here derived Gouy-Chapman model shifts the position of the diffuse layer away from the interface, accounting for the finite size of the ions. The Stern model adds effectively a charged plane to the interface that sits at a distance equal to the atomic thickness, resulting in a linear electric potential dependence in that region. The strength of the linear potential drop is in general proportional to the concentration of the adsorbed ions, but cannot be easily quantified in the framework of this model.

Overall, from this formula it is evident that the total capacitance of the electrolyte C_d is directly related to four variables, such as the valence of the used ions z, the concentration of the ions in the solution, here expressed by the ionic strength parameter I, the dielectric constant of the electrolyte solvent and the temperature. When designing a new electrolyte with the goal to induce even stronger carrier densities, all these parameters can be adjusted by choosing different ions, solvents and concentrations.

2.1.4 Tailoring electrolytic gates towards better performance

Looking through the literature it becomes evident that for different materials very different electrolytes are used [25; 26; 27; 24; 20]. While a certain electrolyte can induce extremely high n for one material, they can completely fail for another. In general, as it is often the case in material science and electrochemistry, both, the material and the electrolyte have to be chemically compatible with another, having minimal chemical reactions between each other and have a large electrochemically stable voltage range ΔV_{eg}. There is no one best electrolyte for every material, only for a material.

In general, trying to increase C of an electrolyte by changing the different parameters that influence it, such as the valence of the ions or the dielectric constant of the solvent, might eventually not overall result in an increase of the maximal n. Here, as the change of these parameters goes along with changing the ionic species or polymers, the chemical interaction of these with the material can be altered as well and result in smaller ΔV_{eg}, and in the worst case in chemical distortions of the materials surface. Overall, the EDL model has rather low predictive power in the search for better electrolytes, hence a rather systematic sampling approach has proven to be more successful.

As discussed before, to reach highest possible n, one needs both, a high C and a large ΔV_{eg}. To measure the C, we employ Hall measurements in a low magnetic field for different values of the electrolyte gate voltage V_{eg}. As the Hall Voltage $V_H = -\frac{IB}{ne}$ is inversely proportional to n we can extract the capacitance $C = \frac{ne}{V_{eg}}$ of the electrolyte (Fig. 2.3 (b)). Furthermore, in order to map out the ΔV_{eg} range, we perform cyclic voltammetry (CV) measurements which measure the leakage current of the sample vs. V_{eg} [64]. The measured leakage current I is negligibly small for low V_{eg}, but exponentially increases for higher V_{eg}. The cross-over region between these two regimes defines ΔV_{eg}.

2.1.5 Graphene devices with highest possible carrier densities

Here we demonstrate the use of a solid polymer electrolyte gate with mesoscopic graphene devices [65; 25]. This approach has previously been applied to graphene samples [66; 67; 68] and carrier densities of $n \sim 10^{13}$ cm^{-2} have been reported under ambient conditions. Following this experimental approach, we increase the efficiency of the electrolyte gate by employing a rapid cooling method which prevents sample degradation, and reach $n > 10^{14}$ cm^{-2} for both electrons and holes.

Fig. 2.3 (a) shows a working principle of the solid polymer electrolyte gate used in our experiment. Li^+ and ClO_4^- ions are mobile within a solid "mesh" formed by the polymer poly(ethylene)oxide (PEO). By applying a voltage V_{eg} to the electrolyte gate, the ions form Debye layers on top of the graphene and the gate electrode, respectively. The extreme proximity of these charged layers, separated only by the Debye length $\lambda_D \sim 1$ nm from the graphene surface, results in huge capacitances per unit area $C_{eg} = 1/\epsilon\lambda_D$. Under ambient conditions the electrolyte gate V_{eg} can be swept continuously, doping the graphene samples to either electrons or holes, inducing a modulation of $\rho(V_{eg})$ (Fig. 2.3 (a)).

The maximal $|n|$ that can be induced by the solid polymer electrolyte is mainly limited by the onset of electrochemical reactions of the ions with the graphene, which typically turn on when $V_{eg} \sim 3$ V are applied. Although the threshold of the electrochemistry, signaled by a steady increase of ρ with time, depends on the details of the particular device and sample quality, the time span until complete degradation of the sample is typically just a few minutes. We could apply extremely high V_{eg} of up to 15 V to the electrolyte, avoiding electrochemically induced sample degradation by immediate cooling of the sample (< 1 min) below $T < 250$ K. At this temperature, both, the Li^+ and ClO_4^- ions "freeze" out and are no longer mobile within the PEO, fixing the accumulated charges in the Debye layers to the graphene surface. The induced charge carrier densities do not vary significantly over time and temperature until after the sample is warmed up again. Accumulated $|n|$ for each applied gate voltage V_{eg} are characterized directly by performing Hall measurements (Fig. 2.3 (b) inset). Fig. 2.3 (b) shows the measured n as a function of V_{eg}. The capacitive

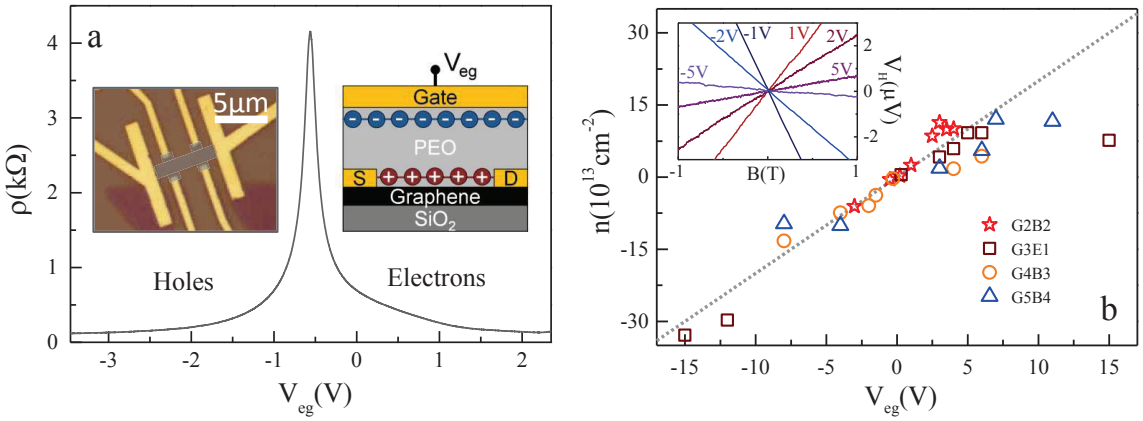

Figure 2.3: (a) Resistivity as a function of applied electrolyte gate voltage V_{eg} at $T = 300$ K. Right inset: a schematic view of the electrolyte gated device. The Debye layers are formed $d \sim 1$ nm above the graphene surface. Left inset shows an optical microscope image (false colors) of a typical etched Hall bar device. (b) Inset shows the Hall voltage V_H as a function of magnetic field B for different V_{eg} (current across sample $I = 100$ nA). The main panel shows the extracted densities n from the various Hall measurements as a function of V_{eg} for 4 different samples. The slope of the line fit represents the capacitive coupling of the electrolyte gate to the graphene.

coupling of the electrolyte can be then estimated from the slope of $n(V_{eg})$ where we obtain $C_{eg} \approx 3.2\ \mu\text{Fcm}^{-2}$, which is more than 250 times higher than that for typical 300 nm thick SiO_2/Si back gates.

2.2 Ionic liquid gating of complex oxide thin films

Mott insulators are typically the parent phases for high-T_c superconductivity, colossal magnetoresistance and metal-insulator transitions [69; 70]. Transition metal oxides (TMOs), particularly 3*d*-TMOs, are excellent model systems for Mott insulators, where localized *d*-orbitals cause strong electron correlation effects. As we move down the periodic table, 4-*d* and 5-*d* TMOs show weaker electron correlation but larger spin-orbit coupling, due to large atomic number. Specifically, in the case of 5-*d* TMOs, the correlation and spin-orbit coupling energy scales become very comparable. Among the 5-*d* TMOs, Ruddlesden-Popper series of iridates such as $Sr_{n+1}Ir_nO_{3n+1}$ ($n > 0$), specifically Sr_2IrO_4 (SIO), show an unusually robust insulating ground state with a spectroscopic gap of ~ 0.1 eV, which persists despite all the efforts on chemical doping and pressure [71; 72]. The exact origin of the robust insulating nature of SIO remains controversial [73; 74; 75; 76; 77]. This compound also shows a weak ferromagnetic moment [78] and is attributed to its canted antiferromagnetic ground state [79; 80; 81]. Due to the interplay between electron correlation, spin-orbit coupling, magnetism and crystal field effects, understanding the nature of insulating state of SIO remains complicated and yet interesting. Existing transport studies report insulating and/or non-ohmic behavior in SIO [71; 78; 82] and have provided little insight into the role of disorder and transport mechanisms of the insulating state. Moreover, predictions of superconductivity in the electron doped SIO and its similarities to La_2CuO_4 [83] invites a thorough transport study to identify means to achieve metallicity in Mott insulating SIO.

The EFE doping with ionic liquids provides a good platform to explore the electronic phase diagram of this Mott insulator without significant chemically induced disorder. Due to the persistent insulating nature, SIO is a good model system to study the interplay of electron localization mechanism in a lightly doped Mott insulator. This discussion on ionic liquid gating of the spin-orbit coupled Mott insulator Sr_2IrO_4 was published in better detail elsewhere [27].

2.2.1 Density dependent transport studies of Sr_2IrO_4

In this section we investigate the electric field effect (EFE) induced magnetoelectric transport in thin films of undoped and La-doped Sr_2IrO_4 using ionic liquid gating.

Thin films of SIO (10-25 nm thick) were grown on $(LaAlO_3)_{0.3}$-$(Sr_2AlTaO_6)_{0.7}$ (LSAT) and $SrTiO_3$ (STO) substrates using pulsed laser deposition. The details of the growth procedures are discussed in detail elsewhere [84]. The transport measurements were carried out in both Hall bar geometry for all the ionic liquid based measurements and van der Pauw geometry in some cases. All the patterns were fabricated using electron beam lithography with PMMA as the resist. Pd (10 nm)/Au (70 nm) electrical contacts and side gate electrodes were deposited using e-beam metal evaporation. The films were then etched into Hall bars using Ar ion milling. A small drop of ionic liquid, N, N-diethyl-N-(2-methoxyethyl)-N-methylammonium bis (trifluoromethyl sulphonyl)-imide (DEME TFSI), was applied on to the device with the liquid covering the entire channel and the side gates (inset of Fig. 2.4 (a)).

We applied gate voltage (V_g) to the side gate in contact with ionic liquid at 260 K and subsequently the sample was cooled at a fixed gate voltage. Below 220 K, the ionic liquid freezes out completely and a stable electrical measurement becomes possible. The gate modulation in the range of -2 V to 3 V was achieved without significant degradation of samples. V_g applied outside of this regime caused electrochemical reactions producing irreproducible $R(T)$. We measured the resistance R of the samples as a function of the temperature T in the range between 1.5-200 K. Fig. 2.4 (a) shows $R(T)$ for SIO films doped chemically with La (filled symbols) and using an ionic liquid gate (open symbols). All samples exhibit $dR/dT < 0$, i.e., an insulating behavior, regardless of chemical doping (up to 10% La doping).

The resistance of ionic liquid gated samples changes rapidly with decreasing T, whose behavior can be modulated by V_g. To quantify this gate dependence, we replot $R(T)$ in an Arrhenius form at fixed gate voltage V_g (inset of Fig. 2.4 (b)). The temperature dependence of these samples could be divided broadly into two regimes: (i) high temperature activated

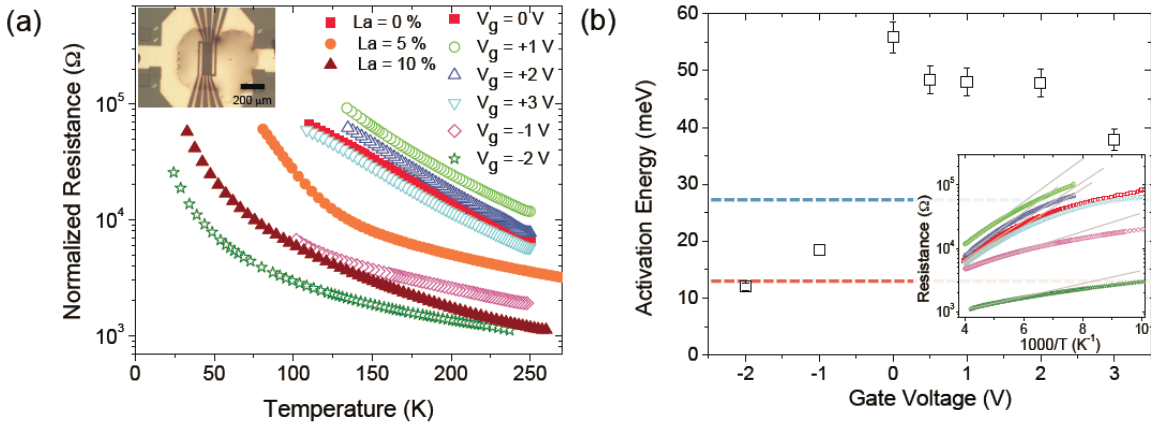

Figure 2.4: (a) Temperature dependence of resistance of an undoped, 10 nm thick SIO thin film with ionic liquid gating (for different applied gate voltages) and chemically doped films (5 and 10% La). The resistance values of chemically doped films were normalized to a 10 nm thick film for comparison. The inset shows the optical image of the Hall bar device with the ionic liquid. (b) The extracted activation energy (black open squares) is shown as a function of applied gate voltage. The inset shows the channel resistance plotted as a function of inverse of temperature. The symbols and the color code used are the same as in (a). The grey lines show the fits for activated transport, whose slopes were used to obtain the activation energy at the high temperature regime. The horizontal dotted lines corresponds to activation energy obtained in the 5% (blue) and 10% La (red) doped samples, respectively.

regime (T >150 K); and (ii) low temperature variable range hopping (T <150 K). The exact nature of the hopping conduction will be addressed later. The activation energy can be obtained from the slope of the linear fit in the high temperature range of the Arrhenius plot. Fig. 2.4 (b) shows the activation energy versus gate voltage. Interestingly, the activation energy, E_a, drops as $|V_g|$ increases with a peak value of $\sim$ 50 meV at $V_g = 0$ V. This ambipolar behavior suggest that the Fermi level E_F of the undoped ($V_g = 0$ V) sample is close to the middle of the gap. The Hall measurement (data not shown) also indicates that $V_g > 0$ (< 0) corresponds to n-type (p-type) carriers. Thus, the bell-shape plot $E_a(V_g)$ establishes ambipolar transport behavior in the Mott insulating SIO. Until recently[85], demonstration of ambipolar doping in a Mott insulator was not realized and it is worth noting that the recent demonstration was also achieved by chemical doping across many samples. In our experiment, similar ambipolar doping of a Mott insulator (SIO) is

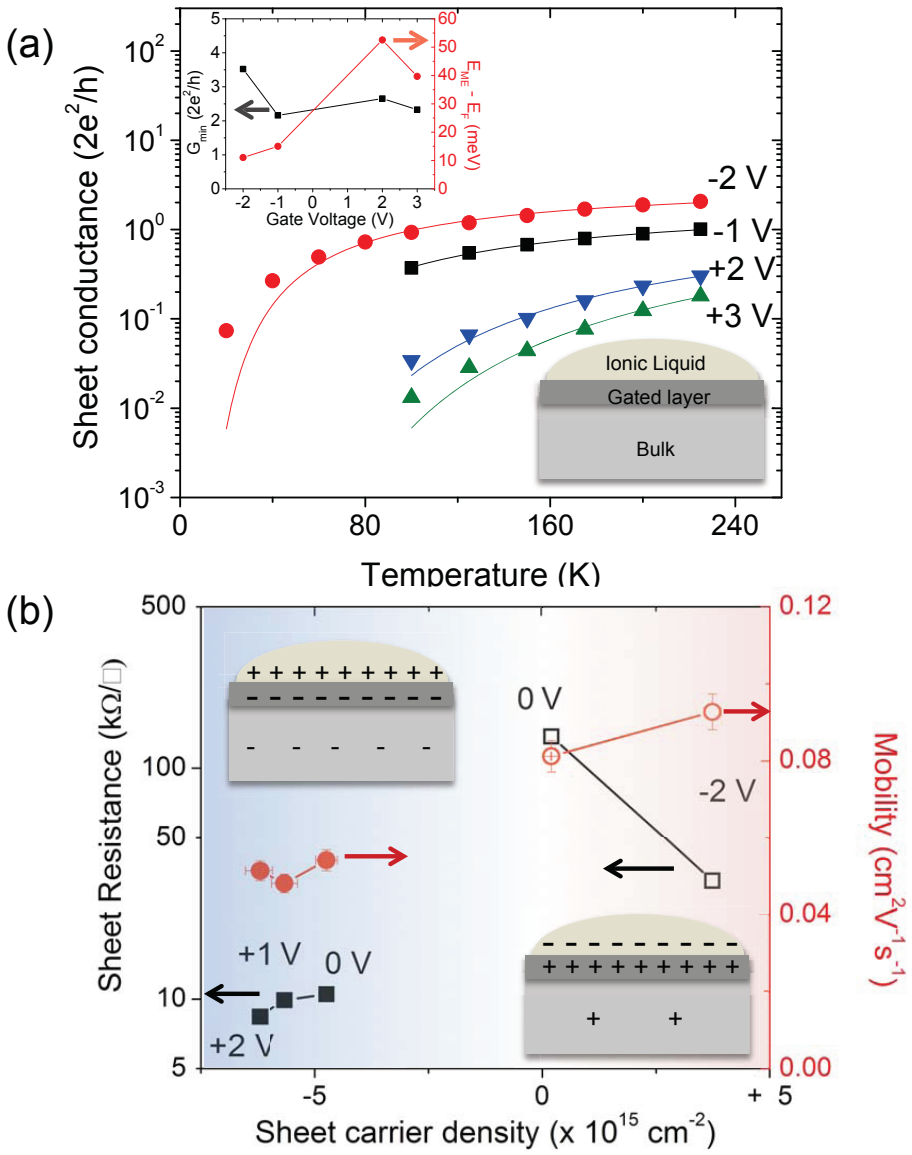

Figure 2.5: (a) Temperature dependent sheet conductances of the ionic liquid gated surface layers measured at different gate voltages. The conductance of the surface layer ΔG was obtained by subtracting the conductance of the ungated portion of the samples (see the lower inset for a schematic bi-layer model). The solid lines are fits using activation to the mobility edge (see text). The upper inset shows the variation of the G_{min} (black squares) and $E_{ME} - E_F$ (red circles) with the applied gate voltage. (b) Gate modulated resistivity (black squares) and Hall mobility (red circles) for a 10 nm thick 10% La doped SIO thin film (filled symbols) and a 25 nm thick 'undoped' SIO thin film (open symbols) as a function of the Hall sheet carrier density (modulated by the gate voltage). The data were obtained at similar temperatures of 190 and 150 K respectively. The inset shows the schematic diagram of free and bound charge distributions in the samples.

demonstrated in a single sample via electrochemical modulation.

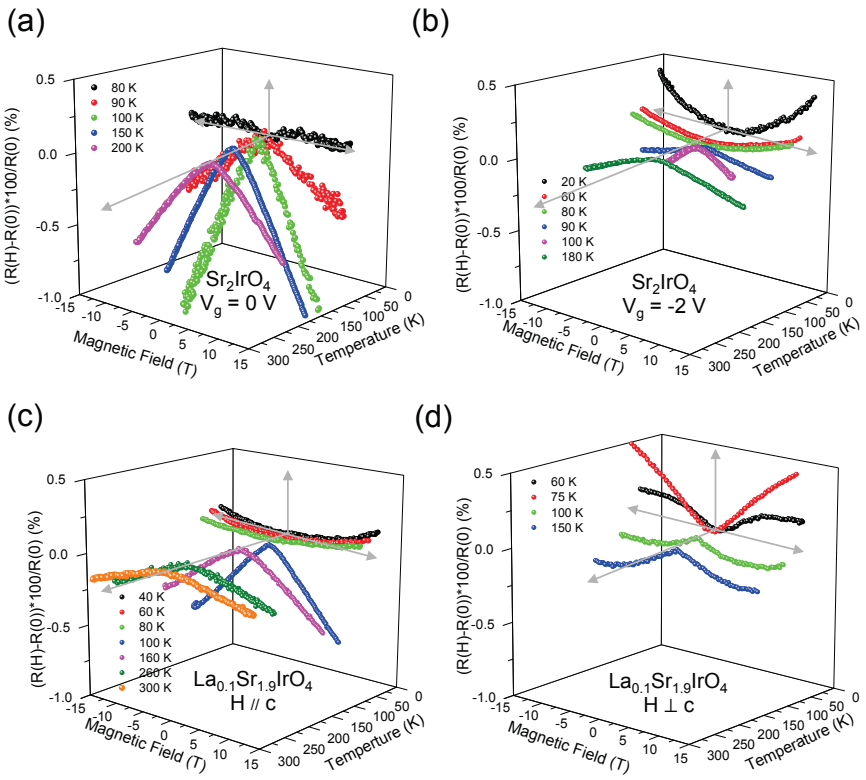

Figure 2.6: The measured magnetoresistance as a function of both applied magnetic field and temperature for (a) undoped SIO, (b) ionic liquid gated SIO (hole doped with $V_g = -2$ V), (c) electron doped $La_{0.1}Sr_{1.9}IrO_4$ thin film, and (d) electron doped $La_{0.1}Sr_{1.9}IrO_4$ thin film with applied field parallel to $a-b$ plane. For all the other three cases, except (d), the magnetic field was applied parallel to c-axis.

In order to understand the nature of the gated surface layer, we used a simple two layer model as depicted in the lower inset of Fig. 2.5 (a). Hall measurements show that the 'undoped' bulk sample has a weak p-doping (Fig. 2.5 (b)), with the carrier density $n \approx 9 \times 10^{19}$ cm^{-3}. Upon applying electrolyte gating, EFE induced charges accumulate on a surface layer, which has a different conductivity as compared to the bulk of the film. For the hole accumulation side ($V_g < 0$), the conductance of surface layer, G_s, can be estimated from the difference of the conductance with reference to $R_0 = R(V_g = 0\text{V})$: $G_s(V_g) = R(V_g)^{-1} - R_0^{-1}$.

In the case of electron doping ($V_g > 0$), depletion layer forms in between the electron accumulated n-type surface conduction layer and weak p-type bulk. Therefore $R(V_g)$ decreases initially when V_g increases as shown in Fig. 2.4 (a). For undoped samples, $R(V_g)$ is the largest for $V_g \approx 1$ V. The thickness of depletion layer, ℓ_d, thus can be estimated from $\ell_d = (R(Vg = 1\text{ V})/R_0 - 1)d \approx 4$ nm, where $d = 10$ nm is the thickness of the sample. Using ℓ_d, we can estimate G_s for this inversion regime by subtracting the sheet conductance of depleted layer using the formula : $G_s = R(V_g)^{-1} - \left(\frac{d-\ell_d}{d}\right) R_0^{-1}$. Fig. 2.5 (a) shows G_s (T) for fixed V_g. The conductance steeply drops as T decreases, as expected from the transport through localized states. We employ a simple activation model to mobility edge to describe the temperature dependent transport through the surface conduction layer: $G_s = G_{min} \exp\left[\frac{-(E_{ME}-E_F)}{k_B T}\right]$, where E_{ME}, E_F, and G_{min} are the mobility edge, Fermi energy, and Mott minimum conductance, respectively. Typically such an analysis is performed on semiconductors which show disorder induced mobility edge [86], where characteristic carrier density and temperature dependence of the mobility is observed. Using this simple activation formula, we fit the experimental data of temperature dependent G_s for fixed V_g (solid lines in Fig. 2.5 (a)) and obtain E_{ME} - E_F and G_{min} for different gate voltages are shown in the upper inset of Fig. 2.5 (a). The activation fits are reasonable for higher temperature range (T) for the most of gate voltages. The obtained values of $\Delta E = E_{ME}$ - E_F are similar to the activation energy, E_a, and the G_{min} is $\sim$ few e^2/h, as it is expected for 2D localization [87]. While the disorder driven localization seemingly explain the observed behavior of G_s, there are a few factors that are not captured by a simple localization theory. Fig. 2.5 (b) shows that the measured Hall mobility remains roughly constant ($\sim$0.08 cm^2/Vsec), despite G_s and ΔE decreases almost an order of magnitude for a wide range of carrier density (both electrons and holes). This filling independent mobility is not expected for disorder induced localization, where one expect a steep increase of mobility as the E_F is getting close to the mobility edge [86]. In a system such as SIO, the origin of the mobility edge can be a very delicate question to address, due to the significant interplay between electron correlation, spin-orbit coupling and magnetism affecting the localization

behavior.

Magnetoresistance (MR) measurements can uncover the details of transport mechanisms and has been used as a good check for disorder induced Anderson localization. Fig. 2.6 shows the transverse MR for (a) undoped, (b) ionic liquid gated hole doped, and (c) chemically electron doped samples, and (d) longitudinal MR for electron doped samples, all of which demonstrate a MR sign change at ~ 90 K. At low temperatures, the MR was positive and shows quadratic scaling with field, but at high temperatures, the MR becomes negative and scales linearly with field. For electron doped samples, similar crossover and field dependence was observed in longitudinal MR but the MR values tended to saturate at high fields unlike the transverse MR. The high temperature linear negative MR is often attributed to the quantum interference in the case of hopping conduction [88] and has also been observed experimentally [89; 90]. The low temperature positive MR could be attributed to several possibilities such as the shrinking of electronic impurity wave function under a magnetic field [88], spin dependent MR (Kamimura effect) [91] or due to superconducting or magnetic fluctuations [92]. We eliminate the role of superconducting fluctuations as we are far from the metallic limit. We also exclude the possibility of a magnetic fluctuation based mechanism, since a decreasing MR with temperature is expected as we approach the ordering temperature. We performed magnetization measurements on the undoped and 10% La doped samples to compare the Curie temperature with the MR crossover temperature. The ferromagnetic transition temperatures were ~ 240 K and ~ 150 K for the undoped and the La 10% doped SIO respectively. This suggests that the magnetic transition does not correlate with the observed MR sign crossover. While we cannot rule out any other scenario that can cause the filling independent MR sign change, for now we attribute the shrinking of the electronic impurity wave function as the probable cause for the observed positive MR at low temperatures.

The observed MR sign change and field dependence can be explained considering the ES-VRH to Mott-VRH transition. In particular, the suppression of negative MR at low temperatures is considered a signature of crossover from Mott (M-VRH) to Efros-Shklovskii

variable range hopping (ES-VRH) as predicted theoretically [93] and observed experimentally in a variety of systems [94; 95; 89; 90]. The formation of Coulomb gap during ES-VRH is the consequence of electron interaction and is also shown to be independent of the band filling [96], in agreement with our observations. This explains the universality of the crossover temperature across the doping in this system.

In conclusion, we have shown that ionic liquid gating can be used to realize ambipolar transport in thin films of SIO. Despite large carrier injection, the insulating state persists for both electron and hole doping with ionic liquid and chemical doping with La. We observe a clear MR crossover in terms of sign change, which could signify a crossover from Mott VRH to Efros-Shklovskii VRH. The conduction along Coulomb gap states is speculated as a probable origin of the persistent insulating state in SIO. A clear understanding of the routes to overcome the electron correlation can help us realize metallicity out of the Mott insulating gap in layered perovskite iridate systems.

2.3 Driving intercalation reactions with electrolytic gates

As has been discussed in chapter 1, graphite intercalation compounds (GICs) are stoichiometric, thermodynamically stable materials [38]. In these compounds in-plane electrical conductivity is significantly increased by electron or hole doping from various species that are intercalated between the graphene layers, and new physical phenomena such as for example superconductivity are predicted to emerge [37].

As mentioned earlier in this chapter it is typically highly undesirable to apply too large V_{eg} to electrolytic gates as unwanted electrochemical reactions begin to take place that can chemically distort the sample. Though, owing to graphenes chemically inert nature, it is know that Li^+ ions can be reversibly adsorbed and desorbed at graphenes surface without any chemical degradation. Employing this peculiarity we can now try to specifically induce Li^+ reactions by applying V_{eg}'s higher than the electrochemically stable window ΔV_{eg} where we find clear signatures of intercalation reactions. The electrolytic gates can therefore be used as a new method to create GICs down to single layer thickness.

2.3.1 Optical imaging of lithium intercalation kinetics in graphite

In this section we demonstrate direct, time-resolved and spatially-resolved optical measurements of Li^+ intercalation in GICs using a solid polymer electrolyte gate to drive the reaction. We use a single crystal graphite electrode with lithographically defined disc geometry to facilitate quantitative data analysis. A combination of Raman spectroscopy and optical reflectance microscopy allows us to identify the different Li GIC phases observed as a function of time. The optical measurements distinguish the intrinsic intercalation process against side reactions.

Kish graphite samples were mechanically exfoliated onto a Si substrate with 285 nm thermal oxide, and selected by visual inspection. A $\sim$ 100 nm thick chromium mask was defined by standard e-beam lithographic techniques and deposited by e-beam evaporation. Reactive ion etching with O_2 plasma was carried out to shape the underlying graphite

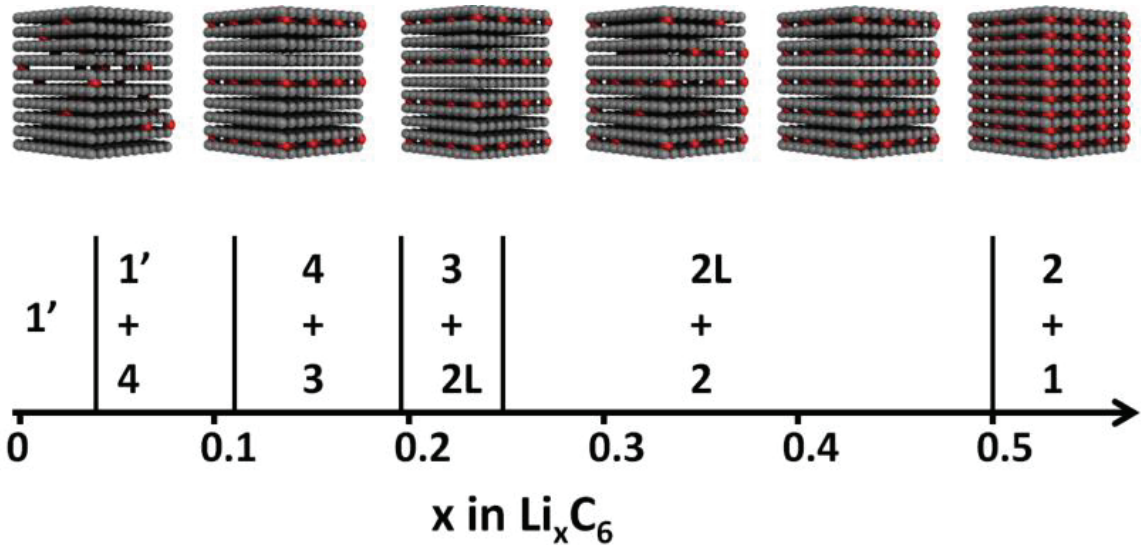

Figure 2.7: The equilibrium phase diagram for Li GIC [97; 98]. Li^+ ions diffuse between graphene layers from the graphite crystal edge. The stage number n refers to the number of graphene layers existing between two complete, crystalline intercalated Li monolayers. The equilibrium GIC undergoes diffusion-driven first order phase transitions through the shown sequence.

sample, followed by the removal of the chromium mask with chrome etchant. Ti contacts were defined by a second round of e-beam lithography and deposited by e-beam evaporation. Here Ti was chosen as the metal contact to utilize its dense native oxide layer to passivate its surface [99]. After lift-off in an acetone bath, the device was wire bonded to a chip carrier. At the side of the device, a blank Si substrate with e-beam evaporated Ti was also wire bonded to the same chip carrier. This served as a relay pad for attaching Li counter/reference electrodes.

The $LiClO_4$ and PEO were mixed to achieve a molar ratio of 36 : 1 $[CH_2\text{-}CH_2\text{-}O]/Li^+$ and dissolved in 10 ml acetonitrile [100]. A typical amount of 5 μl was applied to the device area under a stereo microscope. After the acetonitrile evaporated and the polymer electrolyte film dried, a fresh cut Li strip was brought into contact with the polymer electrolyte. Bulk Li metal was used as a counter and reference electrode in our study. The Li strip was attached to the Titanium covered blank Si substrate on the side. The assembled device was transferred into an optical cryostat and sealed.

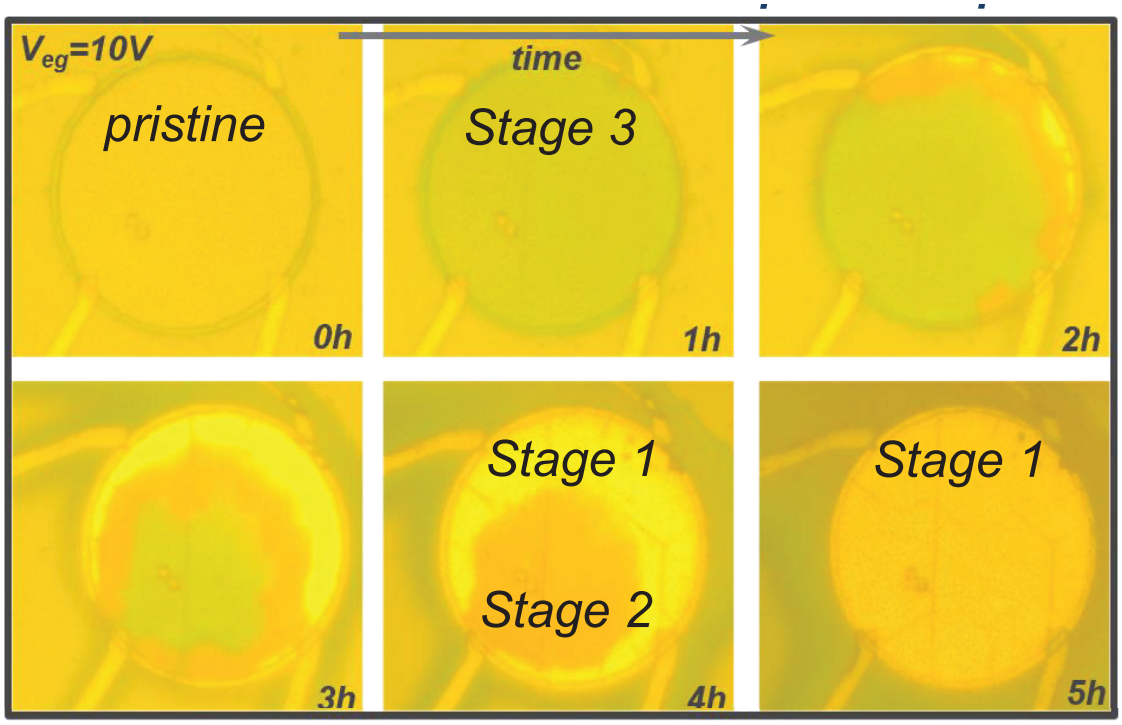

Figure 2.8: Sequential optical images of a disc-shaped graphite sample during the process of Li^+ intercalation over a period of 5 hours. This process is represented by the dilute stage 1 (0 h), stage 3 (1 h), formation of stage 2 and stage 1 (2 h), co-existence of stage 3, 2, and 1 (3 h), co-existence of stage 2 and stage 1 (4 h), stage 1 (5 h). The entire process was reversible when the voltage was reduced to zero.

Fig. 2.8 shows sequential optical images observed following a 5 V voltage step which initiates the Li intercalation from the edge towards the center of the 50 μm graphite disk. The images are also compiled into the time lapse movie in supporting information. Different stages of GIC exhibit distinct colors. These color changes during the intercalation result from the increasing density of delocalized in-plane graphene electrons donated by charge-transfer from the intercalated Li^+ ions. With increasing Li^+ concentration, the Drude plasma edge shifts into the visible region from the infrared region [101; 102; 103; 104], resulting in the distinct reflective color change. Stage 3 is green, stage 2 is red and stage 1 is golden in color.

These phase assignments are further confirmed by Raman spectra in Fig. 2.9 (a). The graphene G peak near 1580 cm^{-1} shows electronic resonance intensity enhancement and

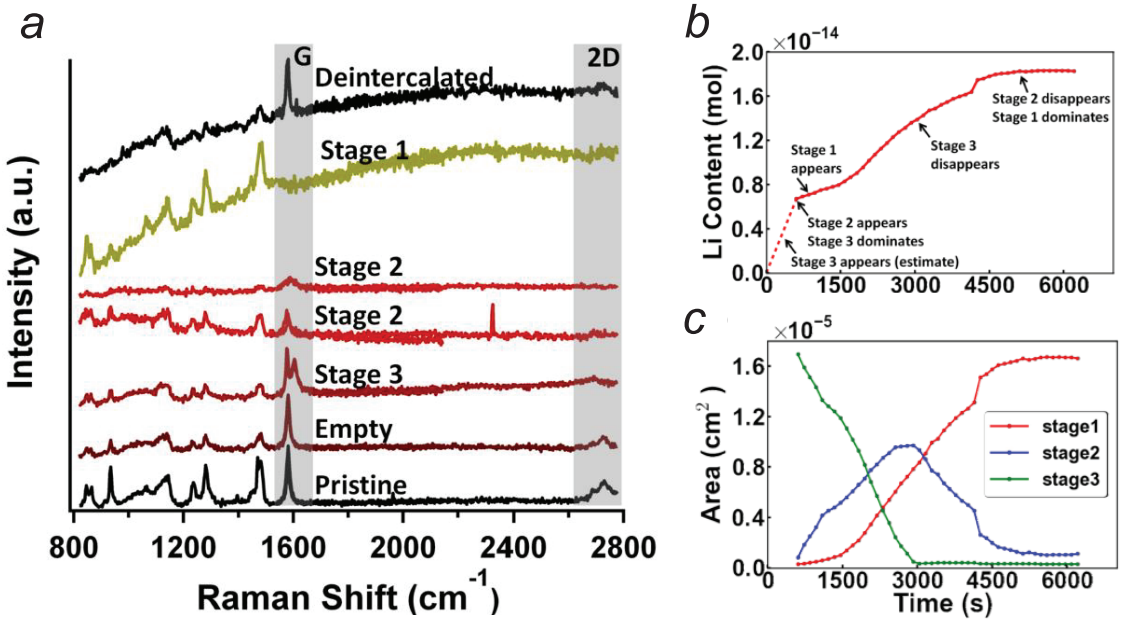

Figure 2.9: (a) Raman spectra of the Li/graphite intercalation system in different stages. The spectra are vertically offset for a clearer display. The peak around 1580 cm^{-1} is graphite G peak. The peak around 2700 cm^{-1} is the graphite 2D peak. The peaks below the G peak originate from the PEO and the (PEO)-Li complexes [105]. (b) and (c) Direct optical measurement of Li intercalation kinetics. Both, the total content of Li within the graphite disc (b) and the area of the distinct stages (c) are extracted from optical images by image segmentation.

shifts to higher frequency with the concentration of electrons donated from Li. It is diagnostic for the electronic structure, clearly evolving from one phase to the next. For $n = 3$ and higher stages, the G peak splits into two peaks as there are two physically inequivalent graphene layers : highly doped graphene in direct contact with intercalated Li and interior graphene with little doping, similar to pristine graphite. Similar two-peak Raman spectra have been recently observed in few layer graphenes with adsorbed NO_2, which is a strong electron acceptor [106]. For stage 2 GIC, in which all graphene layers are equivalent, there is only one G peak with weaker intensity. It is softened to a lower frequency than the direct contact G peak in stage 3, indicating a higher doping level in stage 2, explained by an in plane lattice expansion which sets in at higher doping levels [38]. For stage 1, the G mode is absent, or indistinguishable from the background.

This vanishing behavior, and the weak intensity of the G mode in stage 2, in part, occur because of a loss of electronic resonance intensity enhancement due bleaching of the graphene interband visible optical absorption that accompanies a large Fermi level shift on the order of 1 eV. Recent studies of few layer graphenes with adsorbed potassium, a similarly strong electron donor as Li, show essentially a complete loss of the interband optical absorption [107]. Note that several theoretical calculations have suggested that in stage 1 LiC_6, the charge transfer from the Li atoms to graphene approaches 100% [37; 108].

We can distinguish between different kinetic mechanisms directly from the optical images in Fig. 2.9 (a). If Li diffusion from the edge to the center is fast with respect to Li injection from electrolyte solution at the edge, then the concentration of Li will be the same across the disk. Nucleation of higher concentration phases would occur homogeneously across the disk. This behavior is observed for the initial transformation from dilute stage 1 to stage 3, with possibly stage 4 as an unobserved intermediate. In dilute stage 1 as concentration increases, the graphite domain gradually darkens as a whole. This darkening can be explained by the reduction of electron free carrier lifetime in the presence of randomly distributed Li. As the Li concentration rises, green stage 3 homogeneously nucleates across the disk.

However, the red phase 2 subsequently nucleates at the boundary. This indicates that diffusion of Li from the edge through stoichiometric stage 2, to the stage 3-stage 2 boundary that is moving towards the center, is far slower than the initial diffusion in dilute stage 1. Li concentration builds up at the edge following injection, and nucleates stage 2 before diffusion to the disk center occurs. Furthermore, nucleation of the golden stage 1 occurs almost immediately at the edge after stage 2 begins to form. The system is out of equilibrium, as evidenced by the fact that three different phases (3, 2, and 1) are observed simultaneously. The phase diagram indicates that only two phases (2 and 1 for $x > 0.5$ in Li_xC_6) will simultaneously exist at equilibrium. As the phase boundaries propagate towards the disk center, the green phase 3 first disappears, followed by the disappearance of stage 2, leaving only stage 1. The diffusion is fast enough to produce well formed boundaries between

phases, but not fast enough to distribute Li across the disk in the correct balance of phases, for an injection rate corresponding to the initial 5 V step.

After stage 3 forms, the total Li content in the graphite disk can be obtained directly from the optical images, since we know the stoichiometry of each of the stages 3, 2, and 1. The Li content in each phase is the geometrical area multiplied by the phase Li density. The sum from all phases present yields the total disk Li content, free from any other complicating simultaneous electrochemical processes. Indeed we observed blue film formation around the electrodes resulting from chemical reduction of the polymer electrolyte. The total Li content evolution is shown in Fig. 2.9 (b). The evolution of stage 1, stage 2 and stage 3 are presented in Fig. 2.9 (c).

The injection rate of Li along the disk circumference is the slope of the total Li content curve. It is clear that the injection rate slows down as the intercalation process proceeds. Here the dotted line indicates the presence of a dilute stage 1 and stage 3 and the first data point corresponds to the first image after phase boundaries between stage 3 and stage 2 appear. Comparing with the early fast injection in dilute stage 1, the Li content increases more slowly when it is more concentrated and the slope of this Li content curve decreases. Eventually the injection rate approaches zero as stage 1 forms completely. This slowing-down injection rate serves as a consistency check and supports the idea that Li transport within the graphite electrode is the rate limiting step.

In summary, we have employed an all optical imaging method to measure Li intercalation kinetics into a graphite single crystal in situ, free of complication from electrochemical side reactions. Our method offers direct visualization and a clean measurement of microscopic intercalation kinetics. We expect this method to provide new insight in studies of other 2D materials and in design of energy storage applications.

Chapter 3

Transport properties of graphene in the metallic limit

3.1 Graphene at high carrier densities

Graphenes properties close to the Dirac point, for Fermi energies not higher than $\epsilon_F < 0.3$ eV, or, correspondingly, a carrier density $n < 5\times10^{12}$ cm^{-2}, are studied quite extensively. In this regime graphene is a typical semi-metal with a very small Fermi surface, orders of magnitude smaller than the size of the Brillouin zone (BZ). It has a linear dispersion relation with a circularly symmetric Fermi surface and has two distinct valleys that can be described by the Dirac equation.

The above mentioned energy/density limits are mainly due to experimental conditions under which graphene was studied, where the vast majority of experiments were performed using the typical 300 nm thick Si/SiO_2 back gates, which do not allow to reach higher Fermi energies. For this reason, up to this point in time, graphenes properties at higher ϵ_F were almost unexplored. Though, with the use of electrolytic gates, as was shown in the previous chapter, ϵ_F can now be brought to values of $\epsilon_F \sim 1$ eV, or $n > 10^{14}$ cm^{-2}. In this regime graphene is better described as a metal, rather than a semi-metal, with the size of the Fermi surface now reaching values that are comparable to the size of the BZ. At these

energies the band-structure of graphene starts to deviate from the linear dispersion relation and the Fermi surface becomes strongly trigonally warped, losing its circular symmetry and failing to be approximated by the Dirac equation. The enhanced energies of the electrons also alter the specifics of the interactions of the electrons with phonons and impurities and are ultimately predicted to be drastically modified when ϵ_F is in close proximity to the van Hove singularities (vHS) in the M-points, potentially leading to more complex electronic interactions. In addition, for the case of bilayer graphene, the high energy sub-bands can be populated at $\epsilon_F \sim 0.4$ eV and thus conduction will be now described by a two-liquid model.

In general, due to graphene's amazing tunability, it is now possible to directly study a material at the transition from a semi-metal, or a zero band-gap semiconductor, to a metal, with multiple new observations, such as the first time demonstration of a gate tunable Bloch-Grüneisen temperature Θ_{BG}.

3.2 Electron-phonon interactions at the cross-over from a semi-metal to a metal

At finite temperatures electrons in typical conductors are scattered by phonons, producing a finite, temperature dependent resistivity ρ [109]. If the temperature T is comparable to or larger than the Debye temperature Θ_D - the representative temperature scale for the highest phonon energies - all phonon modes are populated. In this high temperature regime, $\rho(T) \sim T$, reflecting a classical equipartition distribution of the phonons. As T decreases below Θ_D, however, the bosonic nature of the phonons becomes important : only the acoustic phonon modes within the phonon sphere of diameter $k_{ph} = k_B T/\hbar v_s < k_D$ (where k_D is the radius of the Debye sphere and v_s is the sound velocity) are populated appreciably, leading to a more rapid decrease of the resistivity, $\rho(T) \sim T^5$, known as the Bloch-Grüneisen (BG) regime for typical 3-dimensional (3D) metals [110; 111; 112].

Due to the quasi-elasticity of the electron-phonon (e-ph) interactions, the maximal

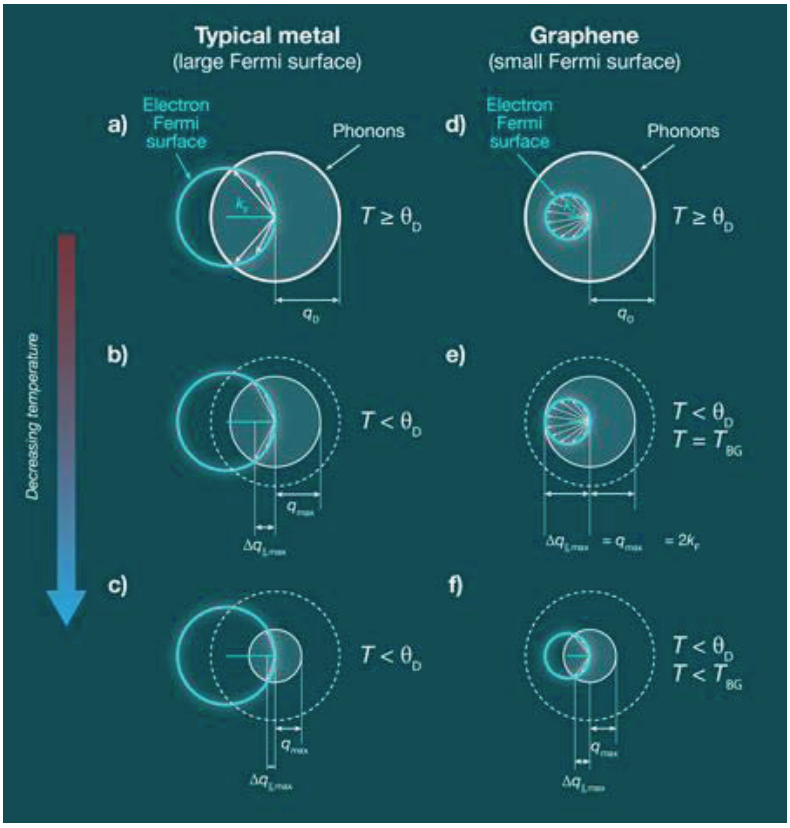

Figure 3.1: (a) to (c) Electron-acoustic phonon scattering for normal metals. Here, owing to the large Fermi surface, all phonon modes can scatter off electrons, with the highest phonon momenta $q_D = k_B\Theta_D/v_s < q_{max} = 2k_F$ being smaller than the momenta needed to quasi-elastically back-scatter an electron at the Fermi surface. (a) For $T > \Theta_D$ all phonon modes are occupied resulting in a $\rho \sim T$ dependence, as the number of occupied phonon modes does not change with T. (b) and (c) For $T < \Theta_D$ only the low energy modes are occupied, resulting in a $\rho \sim T^5$ dependence, as the number of occupied phonon modes now changes with T. (d) to (f) Electron-acoustic phonon scattering for graphene. Due to graphenes small Fermi surface the highest phonon momentum $q_D = k_B\Theta_D/v_s > q_{max} = 2k_F$ is bigger than the highest momentum allowed to quasi-elastically back-scatter an electron at the Fermi surface, allowing now only a small fraction of all occupied phonons to scatter electrons. This defines a new characteristic temperature the Bloch-Grüneisen temperature $\Theta_{BG} = 2\hbar v_s k_F/k_B < \Theta_D$. (d) While for $T > \Theta_D$ and (e) for $\Theta_{BG} < T < \Theta_D$, all phonon modes that are allowed to scatter electrons are occupied, the number of these modes does not change with T, resulting in a $\rho \sim T$ dependence. (f) Only for $T < \Theta_{BG}$ the number of these modes reduces with T, resulting in a $\rho \sim T^4$ dependence. This figure is taken from a ViewPoint on our article [113].

phonon momentum in an e-ph scattering event is limited to $2\hbar k_F$, representing a full backscattering of the electrons across the Fermi surface of radius k_F. Since in metals k_F is of the size of the BZ, $2k_F > k_D$, all populated phonons can scatter off electrons. For low density electron systems, however, the Fermi surface can be substantially smaller than the size of the BZ, and hence $k_F \ll k_D$. In this case, only a small fraction of the acoustic phonons with energies $\hbar v_s k_{ph} \leq 2\hbar v_s k_F$ can scatter off electrons. This phase space restriction defines a new characteristic temperature scale for the low density e-ph scattering, the BG temperature $\Theta_{BG} = 2\hbar v_s k_F / k_B < \Theta_D$. It was explicitly shown in low density 2-dimensional (2D) electron gases formed in semiconductor hetero-junctions [114] that $\rho(T)$ drops at temperatures below $T < \Theta_{BG}$ rather than Θ_D. However, the 3D nature of the phonons in the host material, and the low level of tunability of n, make this system ineligible for studying 2D BG physics and the explicit density dependence of Θ_{BG}.

The advance of graphene [14; 16] brings new aspects to the study of e-ph interactions in a low dimensional system. Graphene has a Debye temperature $\Theta_D \approx 2300$K almost an order of magnitude higher than for typical metallic systems, and the electrostatic tunability of $k_F \propto \sqrt{n}$ allows for a wide range of control of Θ_{BG}. In addition, the single atomic plane structure of graphene provides not only a strictly 2D electronic system, but a 2D acoustic phonon system as well. These unique properties have been considered theoretically, leading to the prediction that graphene exhibits a smooth crossover behavior between the high temperature $\rho(T) \sim T$ and the low temperature $\rho(T) \sim T^4$ dependence [115]. The slower reduction of $\rho(T)$ at low T as compared to the T^5 dependence observed in typical 3D conductors can be understood by the reduced spatial dimensionality. The main discussion on e-ph interactions at the cross-over from a semi-metal to a metal discussed in this chapter was published in better detail in our article [26].

3.2.1 Theory of electron-acoustic phonon interactions in graphene

In the present section we use a simple Boltzmann-transport theory to calculate the effect of electron-phonon scattering on the conductivity of graphene for various temperatures below 300 K, following closely the derivation by Hwang [115]. Here we consider only the interaction with the longitudinal acoustic phonons (LA), an approximation which is well justified, since the coupling to the transverse, out-of plane vibrational modes, the transverse acoustic phonons (TA), is very weak and can be neglected. All other phonon energies, such as graphenes own optical phonons or the substrate polar optical phonons, are extremely high, and can therefore be neglected as they are almost not populated at relevant temperature scales $T < 250$ K considered here.

Using the general expression for Boltzmann transport in graphene, the expression for the energy and temperature dependent resistivity is :

$$\rho(\epsilon_F, T) = \frac{\pi\hbar^2}{e^2\epsilon_F} \left\langle \frac{1}{\tau} \right\rangle \tag{3.1}$$

with the general relations for the Fermi energy and the Fermi wave-vector $\epsilon_F = \hbar v_F |\vec{k}_F|$ and $|\vec{k}_F| = \sqrt{\pi n}$, where v_F the Fermi velocity and $\tau(n, T)$ the density and temperature dependent scattering rate. The expression for the scattering time of an electron with wave-vector $\vec{k}$ can be in all generality written as :

$$\left\langle \frac{1}{\tau(\epsilon_{\vec{k}})} \right\rangle = \frac{1}{2} \sum_{\vec{k'}} (1 - \cos\theta_{\vec{k}\cdot\vec{k'}})(1 + \cos\theta_{\vec{k}\cdot\vec{k'}}) W_{\vec{k}\to\vec{k'}} \frac{1 - f(\epsilon_{\vec{k}})}{1 - f(\epsilon_{\vec{k}})} \tag{3.2}$$

Here the term $\frac{1}{2}(1+\cos\theta_{\vec{k}\cdot\vec{k'}})$ specifically accounts for the pseudo-spin of graphene which prohibits backward scattering of the electrons. $W_{\vec{k}\to\vec{k'}}$ is the transition probability from a state $\vec{k}$ to $\vec{k'}$ as derived from calculations of Fermi's Golden rule, and for the case of electron-acoustic phonon interactions can be approximated as :

$$W_{\vec{k}\to\vec{k'}} \approx \frac{2\pi D_A^2}{\rho_m v_s A} \sum_{\vec{k}-\vec{k'}} k_F \sin(\theta_{\vec{k}.\vec{k'}}/2)\Delta(\epsilon_{\vec{k}}, \epsilon_{\vec{k'}}) \tag{3.3}$$

with D_A the acoustic deformation potential, v_s the sound velocity of LA acoustic phonons in graphene, ρ_m graphenes mass density, A the area of the sample and $\Delta(\epsilon_{\vec{k}}, \epsilon_{\vec{k'}})$:

$$\Delta(\epsilon_{\vec{k}}, \epsilon_{\vec{k'}}) = N_{\vec{k}-\vec{k'}}\delta(\epsilon_{\vec{k}} - \epsilon_{\vec{k'}} - v_s(\vec{k} - \vec{k'})) + (N_{\vec{k}-\vec{k'}} + 1)\delta(\epsilon_{\vec{k}} - \epsilon_{\vec{k'}} - v_s(\vec{k} - \vec{k'})) \tag{3.4}$$

with $N_{\vec{k}-\vec{k'}} = (\exp(v_s|\vec{k} - \vec{k'}|/k_bT) - 1)^{-1}$ the temperature dependent bosonic occupation number of the phonons.

Having these expressions in place, the integration over all $\vec{k}$ and $\vec{k'}$ will give an effective overall scattering time τ. Here, since $k_BT \ll \epsilon_F$ for all relevant energies ($\epsilon_F > 0.1$ eV) and temperatures ($T < 300$ K), one can restrict all scattering events to within the Fermi surface, which is equivalent to setting $\epsilon_{\vec{k}} = \hbar v_F|\vec{k}| = \hbar v_F k_F = \epsilon_F$. This quasi-elasticity condition effectively pins the whole integration to transitions at the Fermi energy and results in the definition of an effective maximal cut-off energy for phonons that can interact with the electrons, the Bloch-Grüneisen temperature $k_B\Theta_{BG} = 2\hbar v_s k_F$. This energy scale is equal to the maximal energy transfer to an electron at the Fermi surface, in the case of an exact backscattering process with a momentum transfer of $2k_F$, matching a phonon energy of $2\hbar v_s k_F$. Under this quasi-elasticity condition all higher energy phonons are therefore not allowed to scatter electrons and are neglected in the following calculation. After several expansions and integration over all $\vec{k}$ the final expression for the overall resistivity $\rho(k_F, T)$ becomes :

$$\rho(k_F, T) = \frac{1}{4e^2\hbar} \frac{k_F D_A^2}{\rho_m v_s v_F^2} \frac{\Theta_{BG}}{T} \int_0^\pi \frac{\sin^2(\theta/2)\sin^2(\theta)}{\sinh^2((\Theta_{BG}/2T)\sin(\theta/2))} d\theta \tag{3.5}$$

We can now examine the asymptotic behaviour of this expression. In the limit of high temperatures, when $T \gg \Theta_{BG}$, one can expand the sinh in the denominator and obtain :

$$\rho(k_F,T) \approx \frac{1}{e^2\hbar}\frac{k_F D_A^2}{\rho_m v_s v_F^2}\frac{T}{\Theta_{BG}}\int_0^{\pi}\sin^2(\theta)d\theta = \frac{\pi k_F D_A^2}{2e^2\hbar\rho_m v_s v_F^2}\frac{T}{\Theta_{BG}} \tag{3.6}$$

and in the limit of low temperatures, when $T < \Theta_{BG}$, one can expand $\sin(\theta/2)$ and $\sin(\theta)$ integrating now to infinity, with $x = \frac{\Theta_{BG}}{4T}\theta$:

$$\rho(k_F,T) \approx \frac{64}{e^2\hbar}\frac{k_F D_A^2}{\rho_m v_s v_F^2}\left(\frac{T}{\Theta_{BG}}\right)^4\int_0^{\infty}\frac{x^4}{\sinh^2(x)}dx = \frac{192\zeta(4)}{e^2\hbar}\frac{k_F D_A^2}{\rho_m v_s v_F^2}\left(\frac{T}{\Theta_{BG}}\right)^4 \tag{3.7}$$

using the identity $\int_0^{\infty}\frac{x^4}{\sinh^2(x)}dx = \frac{1}{8}4!\zeta(4)$, where ζ is the Riemann-Zeta function

3.2.2 Temperature dependent transport in density controlled graphene

In this section, we study the experimental observation of the 2-dimensional Bloch-Grüneisen (BG) behavior in graphene. Using a polymer electrolyte gate as discussed in chapter 2, we achieve extremely high carrier densities up to $4\times10^{14}\text{cm}^{-2}$ for both electrons and holes, tuning Θ_{BG} to values of up to $\sim$ 1000 K. In the low T limit, $T \ll \Theta_{BG}$, a $\rho(T) \sim T^4$ is observed, reflecting the 2D nature of the electrons and the acoustic phonons in graphene. At high temperatures, the resistivity shows a semiclassical $\rho(T) \sim T$ behavior. From analysis of the experimental data of $\rho(T)$, we obtain $\Theta_{BG}(n)$ and show that $\rho(T)$ scales as a universal function $\rho(T/\Theta_{BG})$ of the normalized temperature T/Θ_{BG} for all densities $|n|$, which agrees well with the theoretical expressions.

In previous graphene experiments employing thermally grown SiO_2 layers as the gate dielectric [116; 117], $\rho(T)$ could be measured only in the density range $|n| < 5\times10^{12}$ cm^{-2}. In this relatively low range of carrier density, $\rho(T) \sim T$ was reported for all $T < 150$ K, and, at higher temperatures, $T \geq 150$ K, $\rho(T)$ exhibited a rapid increase presumably due to the scattering by thermally activated SiO_2 polar optical phonons [116], by thermally quenched graphene ripples [117], or by Coulomb impurities [118]. In addition, the low temperature behavior of $\rho(T)$ below $T < 20$ K was found to be completely dominated by disorder in the samples. These extrinsic effects become less pronounced at higher carrier densities where

the carrier screening is enhanced [116]. Furthermore, an increased carrier density would result in an increase of Θ_{BG}, allowing to access the non-linear $\rho(T)$ of the BG regime in a much wider temperature range.

In this experiment we have measured $\rho(T)$ for more than 10 single layer graphene samples, in the temperature range $1.5 < T < 300$ K and for $|n| < 2 \times 10^{14}$ cm^{-2}. Fig. 3.2 (a) shows a representative data set for the measured $\rho(T)$ at various fixed n. Generally, $\rho(T)$ decreases monotonically as T decreases, saturating to ρ_0 in the low temperature limit (in our experiment, ρ_0 is determined from the measured ρ at the lowest temperature (≈ 2 K)). This residual resistance ρ_0 stems from almost temperature independent scattering mechanisms, such as static impurity and point defect scattering, as discussed in previous studies [117; 116]. As shown in Fig. 3.2 (b) inset, the corresponding mobility follows $\mu_0^{-1} = (\rho_0 e n) \approx a + bn$ [119] with the fitting parameters $a = 3.3 \times 10^{-4}$ Vs/cm^2 and $b = 3.9 \times 10^{-18}$ Vs, representing long and short range impurity scattering, respectively.

At a first glance, the temperature dependent $\rho(T)$ can be subdivided into two different temperature regimes: (i) the high temperature linear T regime (For $|n| \leq 10^{13}$ cm^{-2}, a strong activation behavior of $\rho(T)$ is observed for $T \geq 150$ K as shown in [117; 116]); and (ii) the low temperature non-linear T regime. This transitional trend of $\rho(T)$ at low temperatures can be better scrutinized by subtracting off ρ_0 from $\rho(T)$. Fig. 3.2 (b) displays $\Delta\rho(T) = \rho(T) - \rho_0$ as a function of T in the logarithmic scale. At a given density n, each curve of $\Delta\rho$ shows a clear transition from a linear high temperature behavior ($\rho \sim T$) to a superlinear ($\rho \sim T^4$) behavior at low temperatures, as is expected from the BG model applied to electron-acoustic phonon scattering in graphene [115]. The cross-over temperature between these two different regimes appears to be higher for higher carrier densities, in good accordance with the BG description presented above, where $\Theta_{BG} \propto \sqrt{n}$.

We now quantitatively analyze our data in terms of the BG model. As derived in the previous section, considering the e-ph interaction as the major source of scattering, the temperature dependent resistivity of graphene can be obtained using the Boltzmann transport theory [115]:

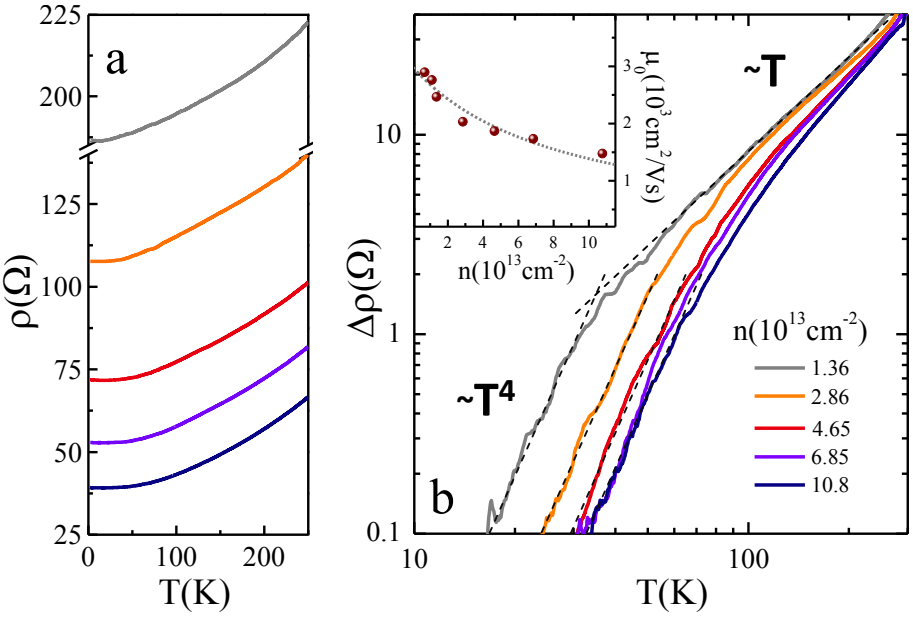

Figure 3.2: (a) Temperature dependence of the resistivity for different charge carrier densities of sample G8A4. (b) The temperature dependent part of the resistivity $\Delta\rho(T)$ scales as T^4 in the low T range and smoothly crosses-over into a linear T dependence at higher T. Dashed lines represent fits to the linear T and T^4 dependency, respectively. Inset shows the mobility μ_0 at $T = 2$ K as a function of the density n. Grey line is the theoretically expected mobility due to short and long range impurity scattering.

$$\Delta\rho(T) = \frac{8D_A^2 k_F}{e^2\rho_m v_s v_F^2} f_s(\Theta_{BG}/T), \tag{3.8}$$

where the generalized BG function for graphene is given by the integration form :
$f_s(z) = \int_0^1 \frac{zx^4\sqrt{1-x^2}e^{zx}}{(e^{zx}-1)^2}dx$.

Here we remark that Eq. 3.8 is different from a typical BG formula for a 3D metal in three points. First, the integrand contains x^4 instead of x^5, reflecting the 2D nature of both, the electrons and acoustic phonons in graphene. Second, the relevant normalized temperature scale is Θ_{BG} instead of Θ_D, considering the fact $\Theta_{BG} < \Theta_D$ in our experimental range. Third, the absence of backscattering for the carriers manifests itself in the factor $\sqrt{1-x^2}$ in the integrand, representing the chiral nature of the carriers in graphene.

Taking the two opposite limits of the temperature ranges, Eq. 3.8 we further approximate

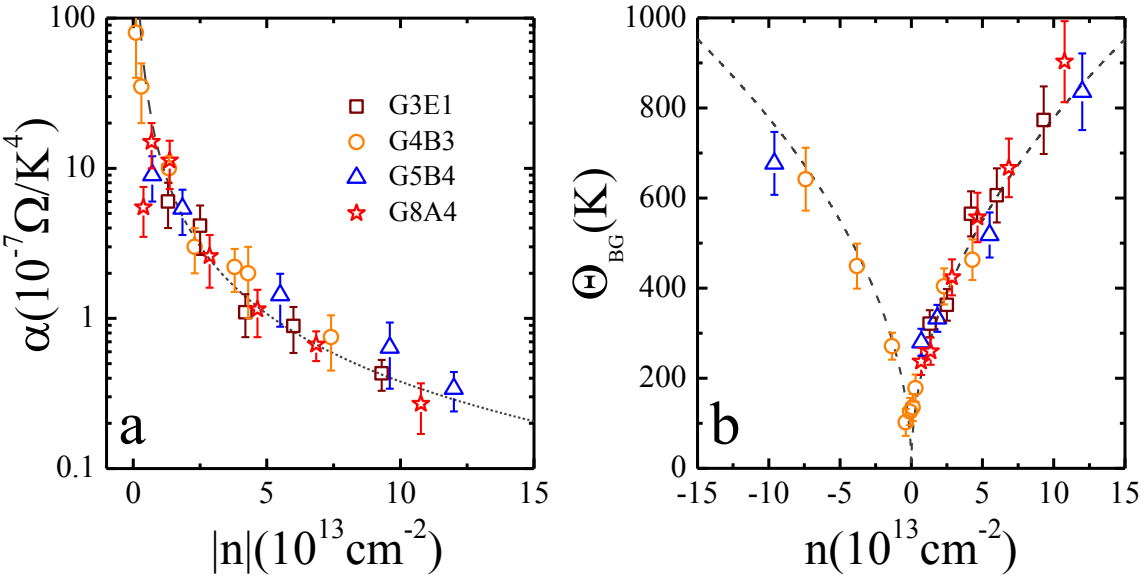

Figure 3.3: (a) Scaling of the prefactors $\alpha(n)$ ($\Delta\rho \approx \alpha(n)T^4$). Data points were obtained from T^4 fits of the $\rho(T)$ traces at different carrier densities and for different samples. The dashed line represents a theoretically predicted fit $\propto |n|^{-\frac{3}{2}}$. (b) Θ_{BG} at different carrier densities (symbols are defined as in (a)). The grey line is a fit to the theoretically predicted $\Theta_{BG} = 2\hbar v_s\sqrt{\pi n}/k_B$.

to $\Delta\rho \approx \gamma T$ for $T > \Theta_{BG}$ and $\Delta\rho \approx \alpha T^4$ for $T \ll \Theta_{BG}$, where the temperature independent proportionality coefficients are explicitly given by [115]:

$$\gamma = \frac{\pi D_A^2 k_B}{4e^2\hbar\rho_m v_s^2 v_F^2} \tag{3.9}$$

and

$$\alpha = \frac{12\zeta(4) D_A^2 k_B^4}{e^2\hbar^4\rho_m v_s^5 v_F^2}(\pi n)^{-\frac{3}{2}} \tag{3.10}$$

Here we particularly note that $\alpha \propto |n|^{-3/2}$, while, γ is density-independent. Using these properties, we obtain γ and $\alpha(n)$ from the experimentally observed $\Delta\rho$ at fixed n. First, $\gamma \approx (0.14 \pm 0.01)\ \Omega/\mathrm{K}$ is estimated from the converging high temperature limit, scaling almost linearly down to $T \sim 0.2\Theta_{BG}$ (dotted line in Fig. 3.2 (b) for example). This value

is in reasonable agreement with the previous studies [117; 116]. We then estimate α from each $\rho(T)$ curve at different densities by fitting to $\Delta\rho \sim T^4$ for the temperature range $T < 0.1\Theta_{BG}$. Fig. 3.3 (a) shows the resulting α versus $|n|$ in a wide range of experimentally accessible $|n|$ for 4 different samples. A clear trend of $\alpha(n) \sim |n|^{-3/2}$ can be seen (dashed trace in accordance with Eq. 3.10).

The combination of the two coefficients $\alpha(n)$ and γ allows us to compute the ratios of D_A^2/v_s^2 and D_A^2/v_s^5, respectively, and thus evaluate the values of D_A and v_s separately. Employing $\rho_m = 7.6 \times 10^{-7}$ kg/m^2, and $v_F = 10^6$ m/sec, we find that the average values for each parameter are $v_s = (2.6 \pm 0.4) \times 10^4$ m/sec and $D_A = (25 \pm 5)$ eV, in a good agreement with values reported in previous studies of suspended and substrate supported graphene devices, as well as for graphite and carbon nanotubes [115; 116; 120; 121; 122; 123; 124]. Using these we can now fit each experimental curve $\Delta\rho(T)$ by Eq. 3.8, using Θ_{BG} as a single fitting parameter. Fig. 3.3 (b) displays the experimentally determined Θ_{BG} from this fits as a function of n for both electrons and holes for all measured samples. The obtained Θ_{BG} exhibit the predicted $\sqrt{|n|}$ dependence, explicitly demonstrating our capability to tune the BG temperature of up to ~ 1200 K with the solid polymer electrolyte gate.

We finally discuss the universal scaling of $\Delta\rho(T)$. The experimental estimation of Θ_{BG} allows us now a direct test of the scaling behavior of $\Delta\rho(T)$ following Eq. 3.8 in all temperature ranges. Taking T/Θ_{BG} as a dimensionless parameter, Eq. 3.8 can be rewritten in a dimensionless scaling form :

$$\frac{\Delta\rho(T)}{\Delta\rho(\xi\Theta_{BG})} = \frac{f_s(\Theta_{BG}/T)}{f_s(\xi^{-1})} \tag{3.11}$$

where ξ is an arbitrary constant setting the normalization temperature relative to Θ_{BG}.

Fig. 3.4 displays the universal scaling behavior of Eq. 3.11 converted from Fig. 3.2. Here we simply choose $\xi = 0.2$ to ensure $\Delta\rho(\xi\Theta_{BG})$ is within the experimentally accessible range. Remarkably, each normalized curve of $\Delta\rho$ with different n (thus different Θ_{BG}) falls

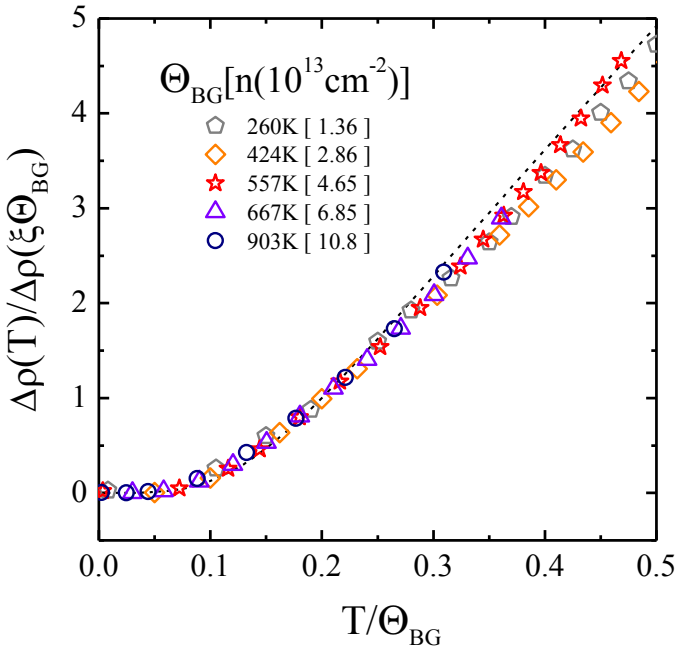

Figure 3.4: Universal scaling of the normalized resistivity $\Delta\rho(T)/\Delta\rho(\xi\Theta_{BG})$ as a function of the normalized temperature T/Θ_{BG}, explicitly using the constant $\xi = 0.2$. Data points correspond to $\Delta\rho(T)$ of sample G8A4 at different n and Θ_{BG} and are normalized with respect to $\Delta\rho(\xi\Theta_{BG})$ - the resistivity at $T = \xi\Theta_{BG}$. The dashed line trace represents the theoretically predicted scaling of $f_s(\Theta_{BG}/T)/f_s(\xi^{-1})$ without use of fitting parameters.

on top of the theoretical curve, indicating the BG model of e-ph scattering fully explains $\rho(T)$ not only in the low and high temperature limits, but for all temperatures.

In conclusion, using the electrolyte we have achieved extremely high carrier densities of up to $|n| = 4 \times 10^{14}$ cm^{-2} in graphene samples. This advancement allowed us to observe a strictly 2D Bloch-Grüneisen behavior in the measured resistivity, exhibiting the linear T to superlinear T^4 cross-over, defined by the gate tunable characteristic temperature Θ_{BG}. Our quantitative analysis of the temperature dependent resistivity shows an universal scaling behavior of the normalized resistivity $\rho(T)$ with the normalized temperature T/Θ_{BG}, representing the 2D nature of the electrons and phonons along with the chiral nature of the carriers in graphene.

3.3 Accessing the high energy sub-bands in bilayer graphene

Multi-band transport is common for many complex metals where different types of carriers on different pieces of the Fermi surface (FS) carry electrical currents. Conduction in this regime is controlled by the properties of the individual sub-bands, each of which can have distinct mobilities, band masses, and carrier densities. Other changes to the single-band conduction model include inter-band scattering processes and mutual electrostatic screening of carriers in different sub-bands, which alters the effective strength of the Coulomb potential and hence adjusts the strength of electron-electron and electron-charged impurity interactions.

To understand electronic conduction in this regime, it is desirable to study the properties of the individual bands separately and compare these to the properties in the multi-band regime. This was achieved in 2-dimensional electron gases (2DEGs) formed in GaAs quantum wells [125], where the sub-bands can be continuously populated and depopulated by inducing parallel magnetic fields. In these 2DEGs, an increased overall scattering rate due to inter-band scattering was observed upon the single- to multi-band transition, [126; 127], along with changes in the effective Coulomb potential which led to the observation of new filling factors in the fractional quantum Hall effect [128].

Bilayer graphene (BLG)[14; 16; 129; 130; 131], with its multi-band structure and strong electrostatic tunability, offers a unique model system to investigate multiple band transport phenomena. This discussion on accessing the high-energy sub-bands in bilayer graphene was published in better detail in our article [27].

3.3.1 Multiband transport in bilayer graphene at high carrier densities

In this section, we present a detailed transport study of multi-band conduction in bilayer graphene. Using an electrolytic gate, we were able to populate the HES of bilayer graphene, allowing for both the LES and HES to be occupied simultaneously. The onset of these sub-bands is marked by an abrupt increase of the sample resistivity, most likely due to the

opening of an interband scattering channel, along with the appearance of a new family of Shubnikov-de Haas (SdH) oscillations associated with the HES. A detailed analysis of the magneto- and Hall resistivities in combination with the HES SdH oscillations in this regime enables us to estimate the carrier mobilities in each sub-band separately, where we observe a two-fold enhanced mobility of the HES carriers as compared to the LES carriers at the same band densities.

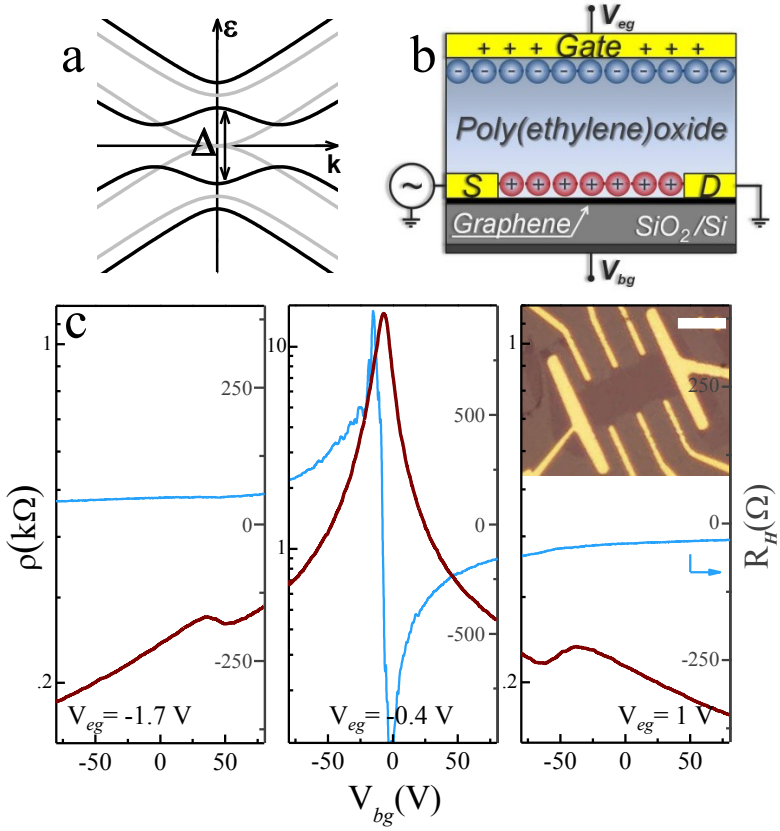

Figure 3.5: (a) The tight-binding band structure of bilayer graphene for interlayer asymmetries $\Delta = 0$ eV (gray) and $\Delta = 0.6$ eV (black). (b) Schematic view of the double gated device, consisting of the SiO_2/Si back gate and the electrolytic top gate. Debye layers of Cs^+ or ClO_4^- ions are formed $d \sim 1$ nm above the bilayer and the gate electrode, respectively. (c) Longitudinal resistivity and Hall resistance of the bilayer graphene device at $T = 2$ K as a function of back gate voltage V_{bg} for 3 different fixed electrolyte gate voltages $V_{eg} = -1.7, -0.4$, and 1 V from left to right, corresponding to pre-doping levels of $n_H = (-2.9, 0, 2.9) \times 10^{13}$ cm^{-2}. Inset shows an optical microscope image of a typical Hall bar device (the scale bar corresponds to 5 μm).

BLG's four-atom unit cell yields a band structure described by a pair of low energy sub-bands (LESs) touching at the charge neutrality point (CNP) and a pair of high energy sub-bands (HESs) whose onset is $\sim \pm 0.4$ eV away from the CNP (Fig. 3.5 (a)). Specifically, the tight binding model yields the energy dispersion [129] :

$$\epsilon^{\pm}_{1,2}(k) = \pm\sqrt{\frac{\gamma_1^2}{2} + \frac{\Delta^2}{4} + v_F^2 k^2 \pm \sqrt{\frac{\gamma_1^4}{4} + v_F^2 k^2(\gamma_1^2 + \Delta^2)}}, \tag{3.12}$$

where the upper and lower index indicates the conduction (+) and valence (−); and LES (1) and HES (2), k is the wave vector measured from the Brillouin zone corner, $v_F \approx 10^6$ m/s is the Fermi velocity in single layer graphene, $\gamma_1 \approx 0.4$ eV is the inter-layer binding energy, and Δ is the inter-layer potential asymmetry.

Interestingly, since a perpendicular electric field E across the sample gives rise to an inter-layer potential difference Δ, it opens a gap in the spectrum of the LES [130; 132; 133; 134; 67] and is furthermore predicted to adjust the onset energy of the HES. Whereas the LESs have been widely studied, the carrier densities needed to fill the HESs, with their expected onset density of $n^* \sim 2.4 \times 10^{13}$ cm^{-2} [130], are much higher than the maximal carrier densities achievable with the conventional SiO_2/Si back gates, which do not permit the tuning of carrier densities above $n \approx 0.7 \times 10^{13}$ cm^{-2} ($\epsilon_F \approx 0.2$ eV). Recent progress in electrolyte gating techniques now allow to access the carrier densities above n^* [26; 135], however the nature of multi-band conduction, especially through the HES in BLG has yet to be investigated.

Bilayer graphene devices were fabricated by mechanical exfoliation of Kish graphite onto 300 nm thick SiO_2 substrates, which are backed by degenerately doped Si to form a back gate. The samples were etched into a Hall bar shape with a typical channel size of ~ 5 μm and then contacted with Cr/Au (0.5/30 nm) electrodes through beam lithography (Fig. 3.5 (c) inset). In order to access the HES we utilized a recently developed solid polymer electrolyte gating technique[65; 66; 68; 25; 67; 26], which was recently shown to induce carrier densities beyond values of $n > 10^{14}$ cm^{-2} [26] in single layer graphene. The working

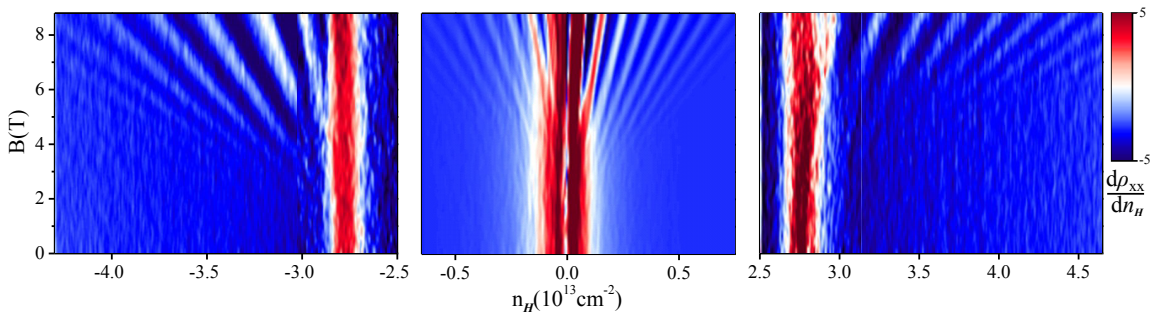

Figure 3.6: Landau fan diagram of the differential longitudinal resistivity $\mathrm{d}\rho_{xx}/\mathrm{d}n_H$ for 3 different density ranges at $T = 2$ K as a function of the Hall density n_H and the magnetic field. (center) The SdH oscillations in the LES converge at the CNP and flatten out at higher n_H due to decreasing LL separation. (left and right) For $|n_H| > 2.6 \times 10^{13}$ cm^{-2} additional SdH oscillations appear, originating at the resistivity spikes (vertical red (black) regions) that mark the onset of the HES.

principle of the solid polymer electrolyte gate is shown in Fig. 3.5 (b). Cs^+ and ClO_4^- ions are mobile in the solid matrix formed by the polymer poly(ethylene)oxide (PEO). Upon applying a gate voltage V_{eg} to the electrolyte gate electrode, the ions form a thin Debye layer a distance $d \sim 1$ nm away from the graphene surface. The proximity of these layers to the graphene surface results in huge capacitances per unit area C_{eg}, enabling extremely high carrier densities in the samples. While $CsClO_4$ has almost the same properties as the typically used $LiClO_4$ salt, we find a reduced sample degradation upon application of the electrolyte on top of the sample, resulting in considerably higher sample mobilities.

One major drawback of the electrolyte gate for low temperature studies is that it cannot be tuned below $T < 250$ K, where the ions start to freeze out in the polymer and become immobile (though leaving the Debye layers on the bilayer surface intact) [25; 26]. A detailed study of the density dependent transport properties at low temperatures can therefore be quite challenging. In order to overcome this issue, we employ the electrolyte gate only to coarsely tune the density to high values ($|n| < 10^{14}$ cm^{-2}) at $T = 300$ K, followed by an immediate cool-down to $T = 2$ K in a helium vapor atmosphere. We then use the standard SiO_2/Si back gate to map out the detailed density dependence of the longitudinal sheet resistivity ρ_{xx} and the Hall resistance R_H, from which we extract the total carrier density

of the sample $n_H = B/eR_H$, with B the magnetic field and e the electron charge. Here we find the back gate capacitance to be $C_{bg} = 141$ aF/μm^2, almost unaltered by the presence of the Debye layers on top of the sample.

In this experiment, we have measured ρ_{xx} and R_H of more than 3 BLG devices as a function of the back gate voltage V_{bg} at various fixed V_{eg} corresponding to the wide density range of $n_H \sim \pm 8 \times 10^{13}$ cm^{-2}. Fig. 3.5 (c) shows ρ_{xx} and R_H for a representative device for 3 selected cool-downs at $V_{eg} = -1.7, -0.4, 1$ V from left to right, corresponding to a pre-doping level of $n_H = (-2.9, 0, 2.9) \times 10^{13}$ cm^{-2}. For low doping levels ($V_{eg} = -0.4$ V, Fig. 3.5 (c) middle) we observe the expected Dirac Peak in ρ_{xx} and the bipolar transition of R_H as V_{bg} sweeps through the CNP. Away from the CNP, ρ_{xx} and R_H decrease as $|n_H|$ increases, as was observed before in BLG samples [131]. For the strongly pre-doped gate sweeps however (Fig. 3.5 (c) left and right), we observe a rather unexpected non-monotonic feature in the sample resistivity. Instead of a monotonic decrease of ρ_{xx} with increasing $|n_H|$, it exhibits an abrupt increase by $\sim 10\%$ symmetrically at both electron and hole sides at $n^* \sim |n_H| = 2.6 \times 10^{13}$ cm^{-2}, a carrier density which is consistent with theoretical expectations for the onset density of the HES [129; 130]. A similarly increasing resistivity at the opening of a new sub-band was previously observed in 2D electron gases (2DEGs) formed in wide GaAs quantum wells [125; 126; 127], where it was attributed to a decreased overall scattering time τ due to the opening of an additional inter-band scattering channel as the new sub-bands are populated. Such an inter-band scattering mechanism between the LES and the HES is also expected to give rise to a resistivity increase upon filling of the HES in BLG samples. However, considering the strong differences between the 2DEG in GaAs quantum wells and in BLG, including the vastly different densities of states, carrier dispersion relation, and more importantly the chiral nature of carriers, we cannot rule out the possibility that the observed resistivity increase in the BLG may differ that of conventional 2DEG.

The electronic structure of the LES and HES can be further investigated by studying the effect of the magnetic field B on the longitudinal resistivity $\rho_{xx}(B)$ in the various density

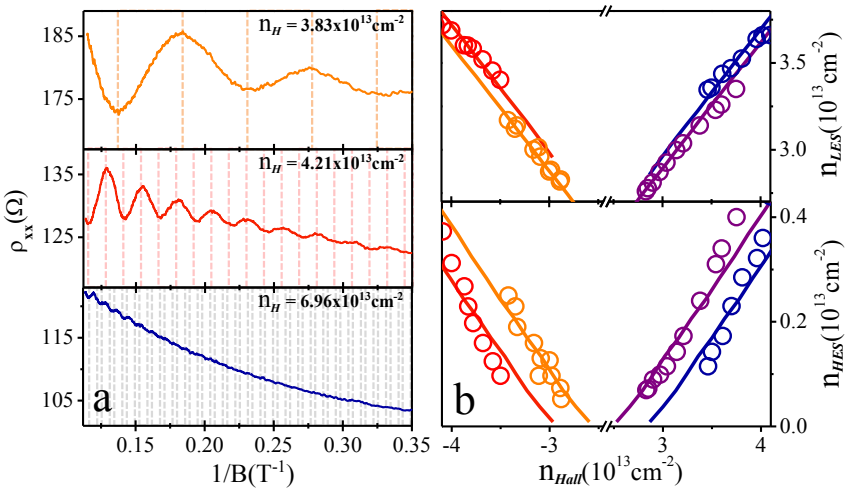

Figure 3.7: (a) Exemplary traces of the longitudinal resistivity as a function of inverse magnetic field at fixed values of n_H beyond the onset of the HES. (b) Carrier densities inferred from the SdH oscillations vs. the overall Hall densities n_H, from 4 cool-downs at different set electrolyte gate voltages $V_{eg} = -2$ V (yellow), -1.7 V (orange), 1 V (red), 1.4 V (blue). (bottom) $|n_{HES}|$ vs. n_H, fitted with theoretical expectations for the HES. (top) $|n_{LES}|$ vs. n_H, fitted with theoretical expectations for the LES. Line traces correspond to theoretical fits for different values of $\Delta = 0.31$ eV (yellow), 0.17 eV (orange), 0.13 eV (red), 0.26 eV (blue).

ranges. Fig. 3.6 shows the Landau fan diagram of the differential sheet resistivity $\mathrm{d}\rho_{xx}/\mathrm{d}n_H$ as a function of B and n_H. Close to the CNP (Fig. 3.6 center) the SdH oscillations in the two LES are quite pronounced, but with increasing density their amplitude quickly decays as the energy separation of the Landau Levels (LL) decreases. Above the onset of the HES (Fig. 3.6 left and right), marked by the "spikes" of increased resistivity (here the red regions) however, we observe another set of SdH oscillations which form LL fans converging into the onset point of the HES.

In order to analyze the SdH oscillations, we now plot the $\rho_{xx}(B)$ traces for various fixed n_H as a function of the inverse magnetic field B^{-1}. Fig. 3.7 (a) displays three exemplary traces at different n_H above the onset density of the HES. All traces show periodic oscillations in B^{-1} allowing us to obtain the SdH density, $n_{SdH} = \frac{4e}{h}\Delta(B^{-1})$, assuming that each LL is both spin and valley degenerate. Whereas for all $|n_H| < n^*$ we find that the obtained $n_{SdH} \approx n_H$, indicating that the SdH oscillations are solely from a

single band (i.e., the LES), for $|n_H| > n^*$ the obtained n_{SdH} values are much smaller than the simultaneously measured n_H values. This behavior can be well explained by assuming that these SdH oscillations reflect only the small fraction of charge carriers lying in the HES. For $|n_H| > n^*$ we hence are able to extract the occupation densities of the LES (n_{LES}) and HES (n_{HES}) from $n_{LES} = n_H - n_{SdH}$ and $n_{HES} = n_{SdH}$. Fig. 3.7 (b) shows the $|n_{LES}|$ and $|n_{HES}|$ in this regime as a function of the total carrier density $|n_H|$. For each fixed V_{eg}, the obtained $|n_{LES}|$ and $|n_{HES}|$ increase as $|n_H|$ increases (adjusted by V_{bg}), for both electrons and holes. Interestingly, we notice that the $|n_{LES}(n_H)|$ are slightly larger for larger $|V_{eg}|$ while the trend is opposite for the HES, i.e. $|n_{HES}(n_H)|$ are smaller for larger $|V_{eg}|$, even though their n_H values are in similar ranges. These general trends can be explained by an increase of the interlayer potential difference Δ for increased values of $|V_{eg}|$, which are predicted by the tight-binding model in Eq. 3.12 to result in an increase of the onset density (energy) of the HES.

While a precise quantitative determination of the expected shift in the onset density of the HES as a function of V_{eg} and V_{bg} requires a self-consistent calculation of $\Delta(V_{eg}, V_{bg})$ and would go beyond the scope of this paper, we can still qualitatively test the above prediction. This is possible since Δ is mostly controlled by V_{eg}, which has a much stronger coupling to the BLG sample than the V_{bg}, thus allowing us to approximately treat Δ as a constant for fixed V_{eg}. Since the experimental traces displayed in Fig. 3.7 (b) correspond to different values of V_{eg} but the same ranges of V_{bg}, Δ is different for each trace and can be extracted from the theoretical fits from Eq. 3.12, with Δ as the only fitting parameter. Indeed for all 4 traces we find good agreement with the theoretical fits; we clearly observe an enhanced onset density (energy) for the traces with larger set potential differences across the sample, which is in good qualitative agreement with theoretical predictions.

We now turn our attention to the transport properties of BLG in the limit of $n_H > n^*$. The filling of these sub-bands creates a parallel transport channel in addition to the one in the LES, thus defining the transport properties in this regime by two types of carriers with distinct mobilities $\mu_{1,2}$, effective masses $m^*_{1,2}$ and sub-band densities $n_{1,2}$ (here the

index corresponds to the LES(1) and HES(2)) [136; 137]. In sharp contrast to a single band Drude model, where $\rho_{xx}(B)$ does not depend on the B field, in a two-carrier Drude theory it is expected to become strongly modified, resulting in a pronounced B field dependence [138] (In this analysis we have adopted a two band model instead of using a more involved multi-band transport which explicitly includes inter-band scattering matrix elements (for example see [139]) in order to reduce the number of fitting parameters for experimental comparison.) :

$$\rho_{xx}(B) = \frac{n_1\mu_1 + n_2\mu_2 + (n_1\mu_1\mu_2^2 + n_2\mu_2\mu_1^2)B^2}{e((n_1\mu_1 + n_2\mu_2)^2 + \mu_1^2\mu_2^2(n_1 + n_2)^2B^2)}, \tag{3.13}$$

Fig. 3.8 (a) shows magneto-resistance traces for different fixed Hall densities n_H. Close to the CNP, where only the LES are populated (Fig. 3.8 (a) black trace), the $\rho_{xx}(B)$ traces are nearly flat as expected from the one-fluid Drude theory. When the density is increased and the HES starts to fill up, however, we observe a smooth transition to an approximately parabolic B field dependence, resulting in a strong increase of ρ_{xx} of up to 25% from 0 T to 8 T. Using the previously extracted carrier densities in the two bands $n_{1,2}$ we can now fit the $\rho_{xx}(B)$ traces with the two-carrier Drude model in Eq. 3.13, with the mobilities of the two sub-bands $\mu_{1,2}$ as the only fitting parameters. As shown in Fig. 3.8 (b) the experimental finding are in excellent agreement with the theory, allowing us to deduce the values of $\mu_{1,2}$ with good accuracy. Moreover, the ability to extract the mobilities of the HES allows us now to characterize the HES in more detail.

In Fig. 3.8 (c) we plot the extracted mobilities of the HES μ_2 against the carrier density in the HES n_2 and compare it to the mobilities μ_1 of the LES at a similar range of sub-band densities in the LES n_1. We find that the mobilities in the HES are at least a factor of two higher than those in the LES. Considering that the effective carrier masses are similar for the LES and the HES, this feature of the HES may be due to the enhanced screening of charged impurity scatterers at higher carrier densities, effectively reducing the scattering rate of the HES carriers on these scatterers. A more detailed theoretical study is required,

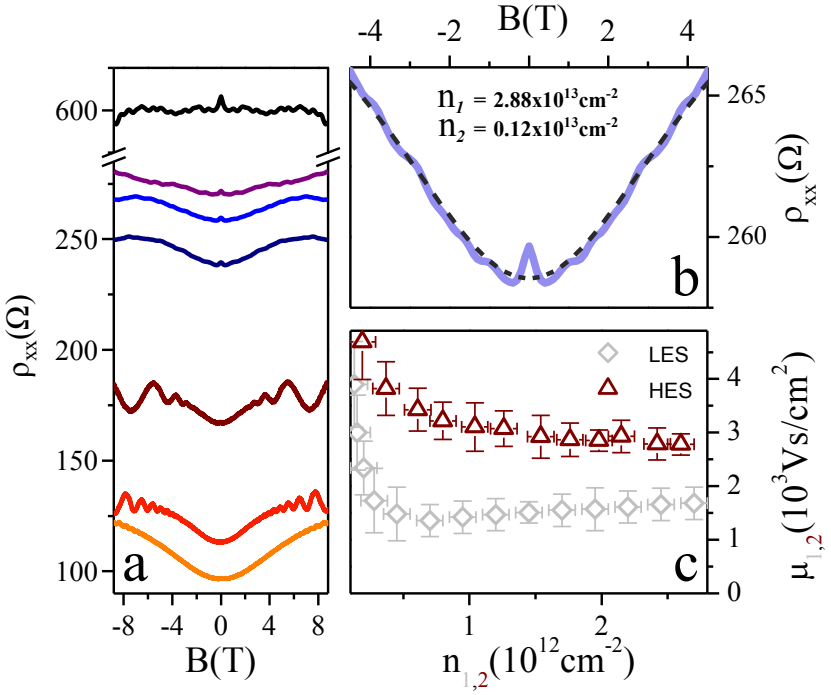

Figure 3.8: (a) Longitudinal resistivity $\rho_{xx}(B)$ as a function of magnetic field for $n_H = (0.84, 2.88, 3.00, 3.31, 3.83, 4.21, 6.96) \times 10^{13}$ cm^{-2}, from top to bottom. The $\rho_{xx}(B)$ traces undergo a smooth transition from a nearly B independent behavior when the HES is empty (below $n_H < n^* \sim 2.6 \times 10^{13}$ cm^{-2}), to a strong, non-trivial B dependence when the HES is occupied. (b) An exemplary $\rho_{xx}(B)$ trace at $n_H = 3 \times 10^{13}$ cm^{-2} and $n_{SdH} = 0.12 \times 10^{13}$ cm^{-2} with accompanying fit (dashed grey line) from Eq. 3.13, using the mobilities in the LES $\mu_1 = 741$ Vs/cm^2 and the HES $\mu_2 = 2303$ Vs/cm^2 as fitting parameters. (c) The mobilities $\mu_{1,2}(n)$ as extracted from $\rho_{xx}(B)$ traces at various fixed n_H as a function of the density in the individual sub-bands.

however, to undertake a quantitative analysis of this problem.

In conclusion, using a polymer electrolyte gate we have achieved two-band conduction in bilayer graphene. We have found that the filling of these bands above a Hall density of $|n_H| > 2.4 \times 10^{13}$ cm^{-2} is marked by an increase of the sample resistivity by $\sim 10\%$ along with the onset of SdH oscillations. From simultaneous Hall and magneto-resistivity measurements, as well as the analysis of the SdH oscillations in the two carrier conduction regime, we have characterized the distinct carrier densities and mobilities of the individual sub-bands, where we have found a strongly enhanced carrier mobility in the HES of bilayer graphene.

Chapter 4

Inducing superconductivity into graphene via proximity effect

4.1 Highly transparent SN junctions across stacked van der Waals materials

Vertical stacking of van der Waals (vdW) materials holds great promises [140; 141; 30; 142; 143; 144; 145]. In analogy to oxide hetero-structures grown by molecular beam epitaxy (MBE) and pulsed laser deposition (PLD) techniques [146; 147; 148; 149; 150], vdW stacking allows to engineer clean, atomically sharp and strongly interacting interfaces [30; 145]. Electronic coupling with properly chosen materials can severely modify the physical properties of the parent compounds and potentially induce complex electronic phases.

So far research on graphene based vdW stacks has predominantly focused on its combination with gapped materials, most prominently hexagonal boron nitride (hBN) [30; 142; 143] that led to dramatic increases of graphene's mobility to $\mu \sim 10^6$ cm^2/Vs and allowed to build high performance electronic devices [144; 141]. While coupling graphene with hBN enhances graphene's intrinsic properties by isolating it from the environment, the interaction between these materials is minimal. A direction so far not explored, however, is to couple graphene with materials that strongly interact with it and could severely modify its elec-

tronic properties, for example by inducing complex electronic phases, such as magnetism, spin-orbit coupling, and superconductivity.

Here it is essential to cleanly couple graphene to the interacting material and to create a highly transparent electronic interface between the two. However, it has proven to be quite challenging, as the typical deposition techniques, such as sputtering, evaporation, atomic layer deposition (ALD), and MBE growth, were shown to be often evasive and/or failed to produce transparent electronic coupling between graphene and the electrodes, resulting in rough and amorphous interfaces [31; 151; 152; 32; 153; 154]. Interfaces between vdW materials could be therefore advantageous here, as one can easily couple single crystals with atomically sharp and clean interfaces. Additionally, the rich variety of choices and the myriads of exotic phases in the vdW materials zoo, reaching from antiferromagnetism (AFM) and high temperature superconductivity in cuprates, to charge-density wave (CDW) and strong spin-orbit coupling in transition metal di-chalcogenides, allow for countless combinations.

In this chapter, we demonstrate the formation of electronically coupled vdW interfaces with highly transparent Ohmic contact resistances below $R_{cnt} < 200\ \Omega$ between stacked high mobility hBN/graphene devices and the superconducting transitional metal di-chalcogenide $NbSe_2$ [155; 156; 157; 158; 159]. Due to Andreev reflections (AR) [47; 45] across the superconductor-to-normal (SN) interface formed below $NbSe_2$'s critical temperature $T_c \sim 6.8$ K the differential conductance dI/dV becomes highly nonlinear and can be modeled with a BKT-theory [46; 45] for highly transparent SN interfaces with $Z \sim 0.5$, as was derived in chapter 1. Due to the large SC gap of $NbSe_2$ $\Delta_{NbSe_2} \sim 1.2$ meV [155] and the ultra clean properties of the so fabricated interfaces [30; 145] we can test a long proposed, but experimentally yet to be realized phase space, where the Fermi energy of graphene can be tuned to values $\epsilon_F \sim \Delta_{NbSe_2}$. Approaching this regime for a hBN/bilayer graphene/$NbSe_2$ stack, we observe strongly modulated AR probabilities, which are in good agreement with theoretical expectations [19; 48; 160].

4.1.1 Andreev reflections in the $\epsilon_F \sim \Delta$ regime in bilayer graphene

In this section we report on inducing superconducting (SC) correlations into bilayer graphene across an electrically coupled vdW superconductor $NbSe_2$. In general the SC proximity effect in graphene is of great interest, as it allows to study the combination of the Dirac equation with the Bogoliubov-de Gennes equations (BdG) [19; 48], leading to exotic predictions like the occurrence of specular AR at the monolayer graphene/SC interface when $\epsilon_F \sim \Delta$ [19], with very similar effects expected for bilayer graphene [160]. Here, instead of the typical retro-reflection process for ARs, where the momentum of the reflected hole is parallel to the momentum of the incident electron, for specular AR's the hole reflects back at an angel. In general, the regime $\epsilon_F \sim \Delta$ has so far not been demonstrated, as it demands for ultra clean graphene with very small potential fluctuations [161; 162; 163] and a transparent electronic interface to a SC with a large gap Δ.

For this purpose $NbSe_2$ is an ideal candidate, since besides its rich electronic properties with the coexistence of CDW and SC phases at low temperatures and a relatively large SC gap of $\Delta_{NbSe_2} \sim 1.2$ meV, it is also chemically stable and can be obtained at ultra high purities. Fig. 4.1 (a) demonstrates typical resistance R vs. temperature T measurements of a mechanically exfoliated 50 nm thick $NbSe_2$ single crystals, with a very sharp SC transition at $T_c \sim 6.8$ K and a wide "hump" due to the CDW transition below $T_{cdw} \sim 33$ K. Here the resistance was measured in a 4-point geometry after establishing electrical contact by direct transfer of the freshly cleaved crystal onto four pre-deposited gold electrodes, resulting in very low, Ohmic contact resistances with typical values of 50-500 Ω. The clear non-monotonicity of the resistance at the CDW transition and, despite the very thin crystal thickness, very sharp SC transition of $\delta T \sim 0.1$ K demonstrate the high quality of the used $NbSe_2$.

In order to fabricate the SN junctions in the cleanest way possible and to reduce any substrate or surface roughness issues, we employ a triple stacked geometry, where vertical stacks of hBN/graphene/$NbSe_2$ are created as shown in a Fig. 4.1 (b). Typical hBN/graphene devices are fabricated following the exact recipes as demonstrated previously [30]. After an

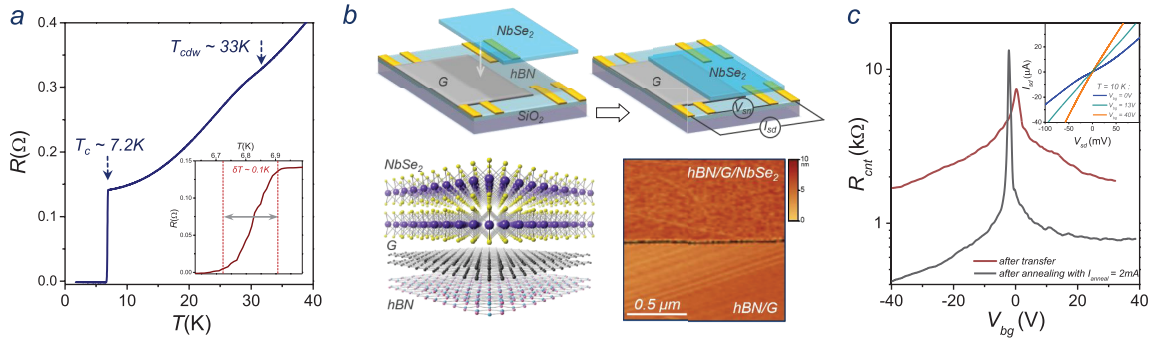

Figure 4.1: (a) Resistance R of the $NbSe_2$ crystal versus temperature T. The crystal undergoes a CDW and a SC phase transition below $T_{cdw} \sim 33$ K and $T_c \sim 6.8$ K respectively, manifesting itself in a "hump" and a sharp drop to zero resistance with a transition width of $\delta T \sim 0.1$ K (inset). (b) Top : Fabrication of a hBN/graphene/$NbSe_2$ stack. The cleaved $NbSe_2$ crystal is transferred onto a clean hBN/bilayer graphene stack from one side and four pre-patterned gold electrodes from the other side. We perform 4-terminal current-biased measurements to characterize the junction. Bottom : Sketch of the cross-section of a vertical hBN/bilayer graphene/$NbSe_2$ stack (left). AFM image of the junction area (right) demonstrates the sharpness and smoothness of the so created SN junction. (d) Inset : typical 4-terminal current-biased I-V measurements for different V_{bg} showing linear, Ohmic characteristics. Contact resistance R_{cnt} versus back gate voltage V_{bg} before (red line) and after (grey line) current annealing across the junction with $I_{anneal} = 2$ mA, resulting in a clear decrease of R_{cnt} after the current is applied, obtaining a minimal contact resistance of $R_{cnt} \sim 400\ \Omega$ ($V_{bg} = -40$ V).

annealing step in hydrogen/argon to clean graphene's surface, we then transfer a freshly cleaved, never exposed to chemicals $20 - 100$ nm thin $NbSe_2$ crystal. The $NbSe_2$ crystal then has an overlap with graphene on one side and with four pre-deposited gold electrodes on the other side, which, as mentioned before, make excellent contact with the $NbSe_2$.

To extract the contact resistance R_{cnt} between graphene and $NbSe_2$, we inject a current of $I_{sd} = 100$ nA across the interface and measure the voltage drop across the interface V_{sn}. In general the V_{sn} signal contains not only the voltage drop just across the graphene/$NbSe_2$ interface, but, due to the intrinsic resistivity of graphene, also a small contribution from the voltage drop inside the graphene channel V_{xx}. In order to compensate for this effect we measure V_{xx} and subtract it from V_{sn} with $R_{cnt} = (V_{sn} - V_{xx})/I_{sd}$. Typical R_{cnt} vs. V_{bg} measurements are shown in Fig. 4.1 (c). Here at negative V_{bg}, R_{cnt} has the lowest values with slightly higher, asymmetric values at positive V_{bg} and with a sharp peak around

the CNP at $V_{bg} \sim 0$ V. Overall this behaviour is analogous to typical metal contacts with graphene [164; 145], such as evaporated gold, or the recently developed side contacts, and can be explained by pn-junction formation at the junction edge, due to work function matching of the graphene with the deposited material under the contact area, with $NbSe_2$'s work-function having very similar values as gold. Here the direct consequence of such pn junction formation is that most of the current is injected at the contact edge and not underneath the contact interface.

Directly after transfer of $NbSe_2$ onto graphene the junction characteristics are Ohmic (inset of Fig. 4.1 (c)) and R_{cnt} has typically values of about $1 - 10$ kΩ at $V_{bg} = -40$ V. By passing a large annealing current of several mA across the interface, R_{cnt} can be further reduced to values as low as 200 Ω ($V_{bg} = -40$ V) in the tails, one of the lowest values reported for any graphene contact. In turn R_{cnt} becomes much higher and sharper in the CNP region (Fig. 4.1 (c)). These changes due to current annealing could be explained by a better hybridization of the vdW crystals at the interface resulting in an effectively reduced size of interfacial potential fluctuations.

To further characterize the junction properties we perform 4-point current biased dV/dI-measurements as a function of source drain current I_{sd}. While for $T > T_c$ dV/dI does not show any strong nonlinearities, for $T < T_c$ sharp nonlinearities starts to appear, becoming stronger as T is lowered (Fig. 4.2 (a)). As is common practice in SC proximity effect experiments, to better resolve the nonlinearities below T_c, we can take dV/dI traces below and above T_c, here at $T = 1.7$ K and $T = 10$ K, and normalize these by dividing them by each other, so defining the normalized differential conductance $G_{1.7K}/G_{10K} = (dV/dI_{10K})/(dV/dI_{1.7K})$. Furthermore, employing the previously extracted R_{cnt}'s, we can find the corresponding junction bias voltage $V_{sn} = R_{cnt}I_{sd}$. The resulting normalized conductance as a function of V_{sn} is shown in Fig. 4.2 (b). The so obtained curve has two pronounced conductance peaks at $V_{sn} \sim \pm 1.2$ mV, coinciding with the size of SC gap of $NbSe_2$, $\Delta_{NbSe_2} \sim 1.2$ meV, with quickly decaying tails at higher voltages and a conductance dip centered around zero bias.

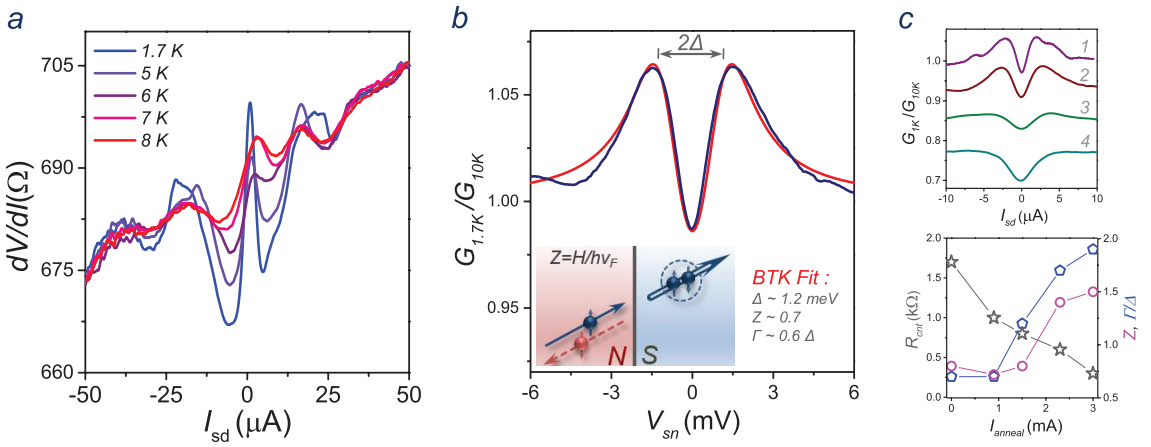

Figure 4.2: (a) Differential resistance dV/dI vs. source-drain current I_{sd} for different temperatures. Below $T_c \sim 6.8$ K the dV/dI signal becomes highly non-linear forming a double-dip structure with a peak around $I_{sd} = 0$ μA. (b) Normalized differential conductance $G_{1.7K}/G_{10K}$ vs. the voltage drop across the SN interface V_{sn}, extracted from $dV/dI-$traces taken below and above T_c. Fitted with an adjusted BKT-theory, we can extract the size of SC gap Δ, which is marked by the two conductance peaks, as well as the Z- and Γ-factors. Inset demonstrates the AR process. (c) Top : normalized differential conductance $G_{1.7K}/G_{10K}$ vs. source drain current I_{sd} for consecutive current annealing steps with the annealing current I_{anneal} across the SN interface with 1. $I_{anneal} = 0.9$ mA, 2. $I_{anneal} = 1.5$ mA, 3. $I_{anneal} = 2.3$ mA and 4. $I_{anneal} = 3$ mA. Overall, the shape of $G_{1.7K}/G_{10K}$ clearly broadens for consecutive annealing steps. Bottom : the extracted R_{cnt}, Z- and -factors vs. I_{anneal}. While R_{cnt} is dramatically reduced, Z and increase for consecutive annealing steps.

We can fit this dependence with a modified BKT [18; 46; 59; 165] theory which accounts for the AR process in the conduction across SN junctions. As is shown in the inset of Fig. 4.2 (b) in an AR process a hole is reflected back in the same direction as the incident electron effectively doubling the conduction and giving rise to a conduction increase for $|eV_{sn}| < \Delta$. Any realistic interface has a finite potential barrier, which can be approximatively modeled by a Delta potential $H\delta(x)$ with potential height H. The incident electron to this barrier can be also just back-scattered, effectively reducing the conductance and leading to a conductance dip around zero bias. These two different scattering events overall give rise to the observed double-peak shape, with the magnitude of the central dip being directly linked to the probability ratios between the two scattering processes which are defined by the transparency factor $Z = H/hv_F$ [18]. Here, for a most realistic fit we also account for

temperature smearing and a finite life-time of the quasi-particles expressed by Γ (Fig. 4.2 (b)).

Right after deposition of the $NbSe_2$ the SN junction has a highly transparent interface defined by $R_{cnt} \sim 1$ kΩ ($V_{bg} = -40$ V), $Z \sim 0.5$ and $\Gamma \sim 0.5\Delta$, so allowing for a high probability of AR processes. Though, these characteristics can be altered by current annealing. Fig. 4.2 (c) top shows $G_{1.7K}/G_{10K}$ vs. I_{sd} for four consecutive annealing steps at increasing maximal annealing currents I_{anneal} with 0.9 mA, 1.5 mA, 2.3 mA and 3 mA resulting in a continuous overall broadening of the double-peak shape, where the extracted Z and Γ are enhanced, while R_{cnt} is continuously reduced (Fig. 4.2 (c) right). While, at first it is rather counterintuitive that an increase of Z can lead to a decrease of R_{cnt}, it could be explained by the increased Γ values. Here one possible scenario would be the formation of mid-gap states in the potential barrier, which would overall lower R_{cnt} but induce disorder, hence increase Γ.

Having successfully fabricated and characterized very clean graphene based SN junctions with a high probability of AR, we can now approach the previously discussed regime where $\epsilon_F \sim \Delta$. Previous experiments were performed on low quality SiO_2 substrates resulting in very large potential fluctuations $\delta\epsilon_F \sim 100$ meV [161; 31; 151; 152; 32; 153; 154]. Here this regime could not be probed with the typical SCs, like aluminum, with their very small SC gaps $\Delta < 0.3$ μeV. For graphene on hBN, these potential fluctuations can now have rather small amplitudes of $\delta\epsilon_F < 5$ meV over spatial variations bigger than several μm [162; 163]. As has been explained before, in our devices the injected electrons enter the SC at the very sharp SN junction edge (see Fig. 4.1 (b)), with a typical overall junction width of ~ 1 μm. Comparing the junction size with the expected spatial variation of $\delta\epsilon_F(x)$, paired with the large SC gap of $NbSe_2$, it appears now to be feasible that when V_{bg} is set at the CNP a large portion of the graphene/$NbSe_2$ junction area fulfills the condition $\epsilon_F \sim \Delta_{NbSe_2} \sim 1.2$ meV.

In the center of Fig. 4.3 we plot $G_{1.7K}/G_{10K}(I_{sd})$ versus V_{bg}, choosing here a much smaller I_{sd} range than in Fig. 4.2 to better resolve the inner gap region where $|eV_{sn}| < \Delta$.

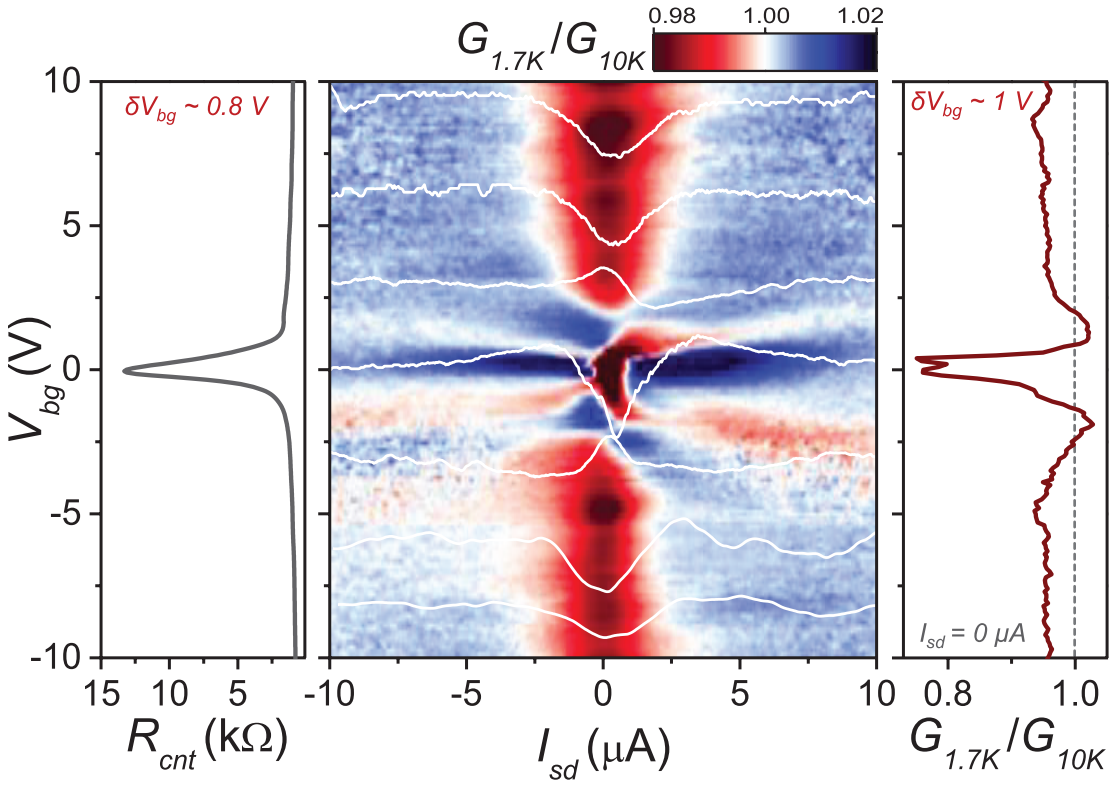

Figure 4.3: Left : R_{cnt} vs. V_{bg} showing the position of the CNP around $V_{bg} \sim 0$ V, with a corresponding half-width of $\delta V \sim 0.8$ V. Center : $G_{1.7K}/G_{10K}$ vs. I_{sd} vs. V_{bg}. The differential conductance is strongly re-normalized for V_{bg} in close proximity to the CNP. Here zero bias dips alternate with zero bias peaks. Right : Line cut from the central figure for $I_{sd} = 0$ μA. While the conductance is reduced for V_{bg} far away from the CNP, it is then enhanced close to it and then much stronger reduced in the CNP.

Here, while for large $|V_{bg}|$ we obtain a familiar double-peak behavior, for $|V_{bg}|$ in close proximity to the CNP, $G_{1.7K}/G_{10K}$ changes quite dramatically : the zero bias dip first renormalizes into a peak and then changes back to a much more pronounced dip directly at the CNP. This is better visible in a line-cut for $G_{1.7K}/G_{10K}(0\ \mu\text{A})$ (Fig. 4.3 right), where it becomes evident that $G_{1.7K}/G_{10K} \sim 0.95 < 1$ for large $|V_{bg}|$ but then is enhanced to $G_{1.7K}/G_{10K} \sim 1.02 > 1$ around the CNP before it then is reduced even further $G_{1.7K}/G_{10K} \sim 0.75 < 1$ right at the CNP. Overall the region of the strongly altered $G_{1.7K}/G_{10K}$ behaviour coincides exactly with the region of the increased R_{cnt} (Fig. 4.3 left), where the half-width of the R_{cnt} vs. V_{bg} peak of $\Delta V_{bg} \sim 0.8$ V also is in excellent

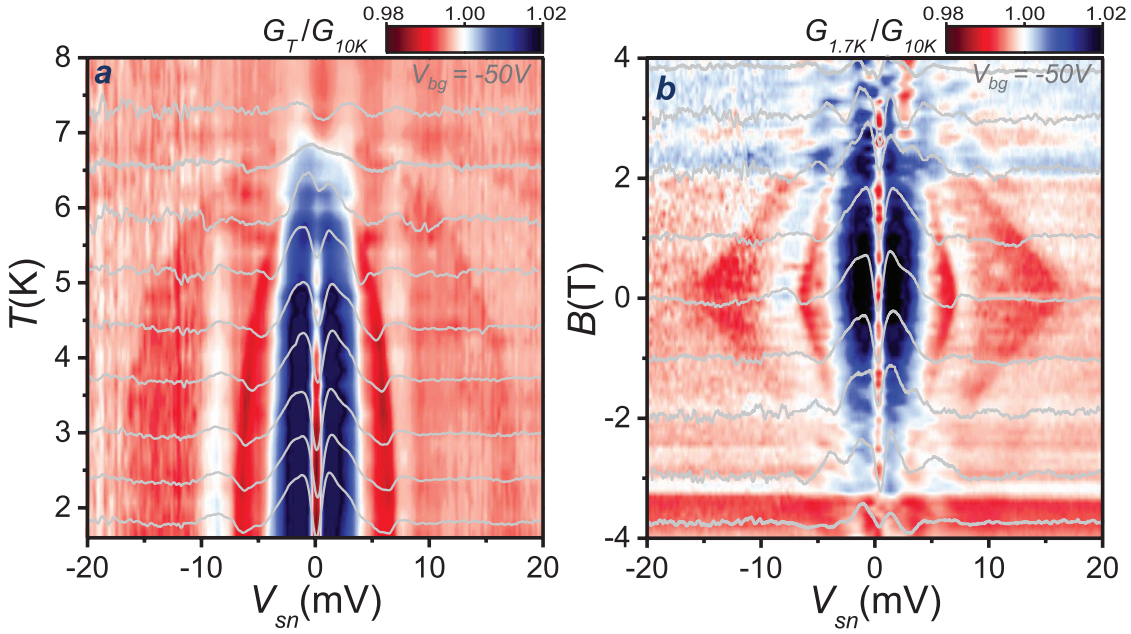

Figure 4.4: (a) T-dependence of $G_{1.7K}/G_{10K}$ vs. V_{sn}. Several, equidistant conductance dips appear for $eV_{sn} \gg \Delta_{NbSe_2}$. These dips scale with temperature as it is expected for the T-dependence of $\Delta(T)$ from the BCS theory. (b) B-dependence of $G_{1.7K}/G_{10K}$ vs. V_{sn}. Here the above gap resonances scale linearly with B-field.

agreement with the half-width of the $G_{1.7K}/G_{10K}$ vs. V_{bg} region of $\Delta V_{bg} \sim 1$ V where the signal is renormalized. From the half-width of the R_{cnt} peak we can estimated the size of the potential fluctuations $\delta\epsilon_F \sim 3$ meV matching the estimates above. In general, this behaviour is in very good agreement with theoretical expectations for the effect of AR on the conduction properties across the SN interface in the vicinity of the CNP [160] in bilayer graphene, where the effective AR probabilities are expected to be altered due to the pseudo-spin degree of freedom of the characteristic scattering probabilities.

One additional peculiarity is observed in the opposite regime where $eV_{sn} \gg \Delta_{NbSe_2}$. Although the conduction properties should not be linked to the SC properties of $NbSe_2$ since the electrons are injected at energies way above the SC gap, nevertheless we observe a set of additional conductance dips that appear to be tightly linked to Δ_{NbSe_2} (Fig. 4.4). Here, we map out a wide voltage range of $G_{1.7K}/G_{10K}$ vs. V_{sn} vs. temperature T and perpendicular magnetic field B. All resonances voltages $V_{n,res}$, with n being the index of

each resonance starting from lower voltages, scale proportionally to the T dependence of $\Delta_{NbSe_2}(T) \sim \Delta(T = 0\text{K})\sqrt{1 - T/T_c}$ as expected from the BCS theory [36]. Overall we identify four resonances that are at approximately equidistant δV_{sn} voltage steps from each other (Fig. 4.4 (a) and (b)) .

The explanation of these resonances could be the formation of standing waves of coherent Andreev-pairs along the z-direction inside the $NbSe_2$. Owing to its ultra thin thickness of only $d \sim 50$ nm and its clean vdW boundaries, such Andreev-states could be elastically reflected at the samples vertical boundaries and constructively interfere forming the equivalent of Fabry-Perot oscillation inside a SC, the so-called Tomasch oscillations [166; 167; 168]. Such above-gap oscillations are typically observed in ultra thin films of very pure SCs with very sharp interfaces. Here the resonance voltage is typically scaling as $V_{n,res} \sim \sqrt{\Delta^2 + (nhv_F/2d)^2}$ with h Plack's constant and v_F the Fermi velocity in the SC. In general this behaviour is in good agreement with our observations, as it also allows for multiple equidistant resonance dips that scale proportionally to the size of the SC gap.

4.2 Co-existence of the quantum Hall effect and Andreev reflections

Inducing superconducting correlations via proximity effect into a two dimensional conductor in the quantum Hall regime has been a long standing proposition which has recently reinvigorated attention [28; 169; 29; 51]. Unlike any other conductor, the samples in the QHE regime have an insulating bulk with conduction occurring only along the edges via chiral edge states. Here, along the SN interface, Andreev reflected electron-hole pairs are bound to the SN interface by strong B-fields, forming Andreev bound states (ABS) [29; 170; 49; 50; 51].

The high mobilities of the graphene in the previously introduced hBN/bilayer graphene/ $NbSe_2$ stacks result in a low B-field onset of the QHE below $B < 1$ T [30; 142]. Together with the relatively high upper critical field of $NbSe_2$ $H_{c2} \sim 4$ T, it thus allows for a wide B-field range of 1-4 T in which the Andreev reflections and the quantum Hall can coexist. The high electronic transparency and the high probability of ARs at the SN interface of such devices provide an ideal platform to probe the ABS.

4.2.1 Andreev spectroscopy in the quantum Hall regime in bilayer graphene

In this section we report on Andreev spectroscopy measurements in the quantum Hall regime in high mobility hBN/bilayer graphene/$NbSe_2$ devices. Here we are employing the stacking technique presented in the previous section to contact a hBN encapsulated high mobility bilayer graphene quantum Hall bar with $NbSe_2$. As can bee seen in Fig. 4.5 (a) and (b), the fabrication process, in comparison to the devices shown in the last section, involves several extra steps. We start with the assembly of a graphene Hall bar on hBN [30] but leave one end of the Hall bar un-contacted by a gold electrode. After cleaning the stack in a H/Ar atmosphere we then cover only the contacted end of the Hall bar with a layer of thin hBN to ensure the preservation of its ultra clean quality in the following fabrication steps. After another H/Ar annealing step, we then deposit the freshly cleaved $NbSe_2$ crystal on the hBN

uncovered end of the Hall bar from one side and four pre-deposited gold electrodes on the other side.

For such devices, using only the non SC electrodes we measure a Hall bar mobility of $\mu \sim 200.000$ cm^2/Vs and find fully quantized Hall plateaus in R_{xy} and zero longitudinal resistances R_{xx} below $B < 1$ T with an onset of spin/valley splitting of the Landau levels (LL) at $B \sim 4$ T (Fig. 4.5 (c)). Furthermore with the four gold electrodes covered by $NbSe_2$ we measure a sharp SC transition at $T_c \sim 7.2$ K from R vs. T and a $H_{c2} \sim 4$ T from R vs. B for the $NbSe_2$ (Fig. 4.5 (d)). Following a similar scheme as in the previous section, we measure R_{cnt} across the so created hBN/bilayer graphene/$NbSe_2$ junction by employing a 4-terminal current biased measurement setup across the junction with extracted $R_{cnt} \sim 1$ kΩ (Fig. 4.6 (a)). Fig. 4.6 (b) shows $G_{1.7K}/G_{10K}$ vs. V_{sn} with the extracted fitting parameters $Z \sim 0.7$, that define the SN junctions electronic transparency, overall confirming a relatively high probability of AR processes.

The detailed view of the T-dependence and the perpendicular B-dependence of the $G_{1.7K}/G_{10K}$ vs. V_{sn} are shown in Fig. 4.6 (c) and Fig. 4.6 (d) respectively. As AR's can take place only inside and in close proximity of Δ_{NbSe_2} the differential conductance features scale with the gap size as it is altered with T and B. Here, starting from $T_c \sim 7.2$ K Δ_{NbSe_2} scales in good agreement with the expected T-dependence from the BCS theory $\Delta_{NbSe_2}(T) \sim 1.74\Delta_0\sqrt{1 - T/T_c}$ [36], with the AR features becoming wider and stronger as T is lowered. Similarly, as the B-field is increased Δ_{NbSe_2} and the AR features become linearly smaller and disappear at $B \sim 4$ T in good agreement with H_{c2}. The linear B-dependence of $\Delta_{NbSe_2}(B)$ is due to type-II SC properties and vortex formation in the crystal of $NbSe_2$. Interestingly we find oscillatory variations of the normalized conductance with the B-field near zero bias, suggesting a potential origin due to Landau level (LL) formation inside the graphene.

To better demonstrate the interplay of LLs and ARs, we set a constant density at $V_{bg} = 2$ V and cross measure B-dependent R_{xx} and R_{xy} of the lowest lying LLs with filling factors, $\nu = 4$ and $\nu = 8$ [131]. We observe the formation of the corresponding

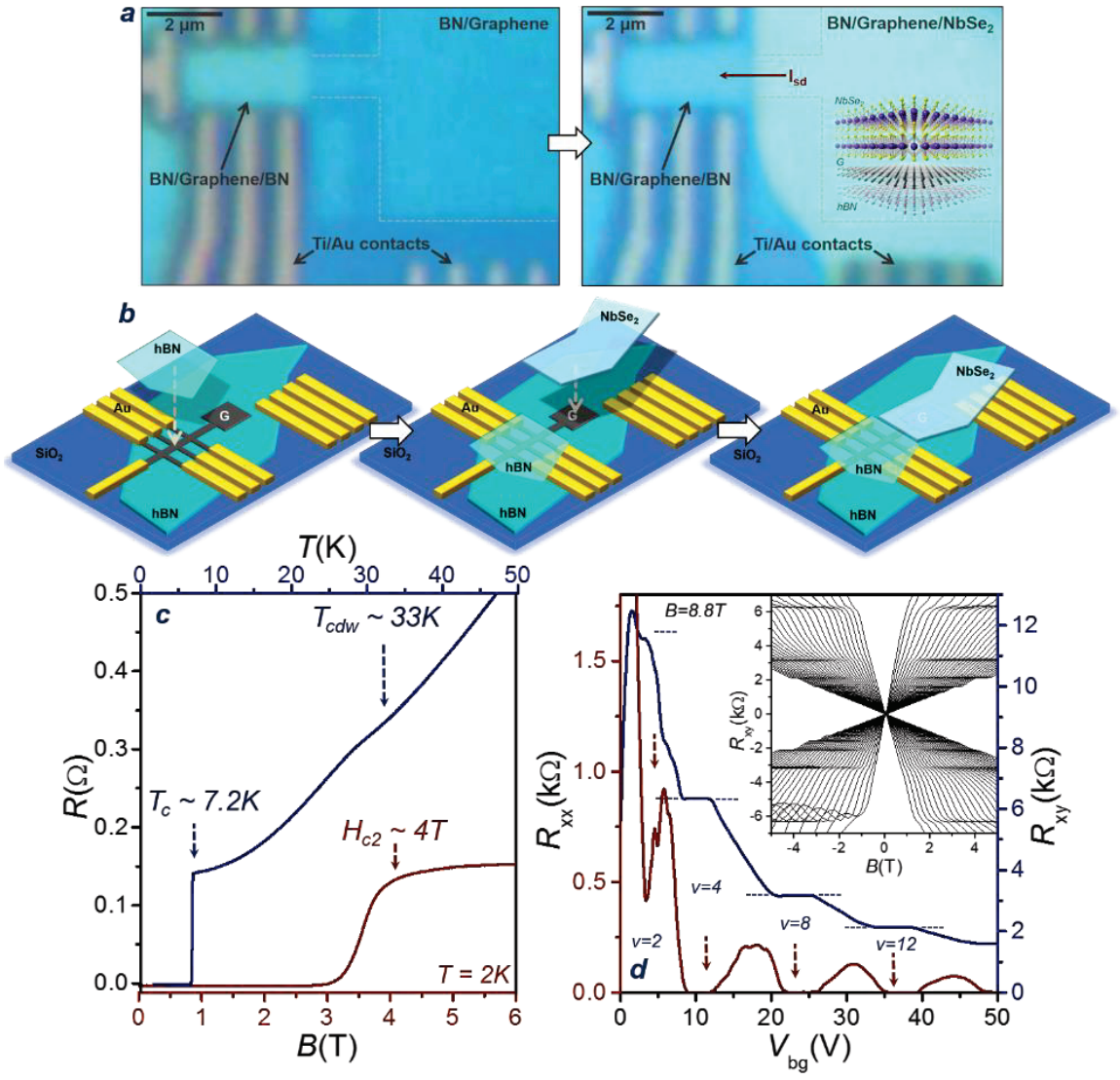

Figure 4.5: (a) Optical image of the hBN/bilayer graphene/$NbSe_2$ hetero-structure before and after deposition of the exfoliated $NbSe_2$ crystal. Inset : layered cross-section of the stack. (b) Illustration of the transfer assembly of the device. The $NbSe_2$ flake is transferred on top of the uncovered graphene region from one side and four pre-deposited gold electrodes from the other side resulting in Ohmic electrical contact of the $NbSe_2$ with all the parts. (c) R vs. T and R vs. B of $NbSe_2$ revealing the CDW transition $T_{cdw} \sim 33$ K, the SC transition $T_c \sim 7.2$ K and a $H_{c2} \sim 4$ T. (d) R_{xy} and R_{xx} vs. V_{bg} at $B = 8.8$ T demonstrating full quantization of the Hall plateaus and zero longitudinal resistance with the onset of spin/valley splitting of $\nu = 2$. Inset shows R_{xy} vs. B for various V_{bg} showing fully quantized plateaus forming at $B <$ T.

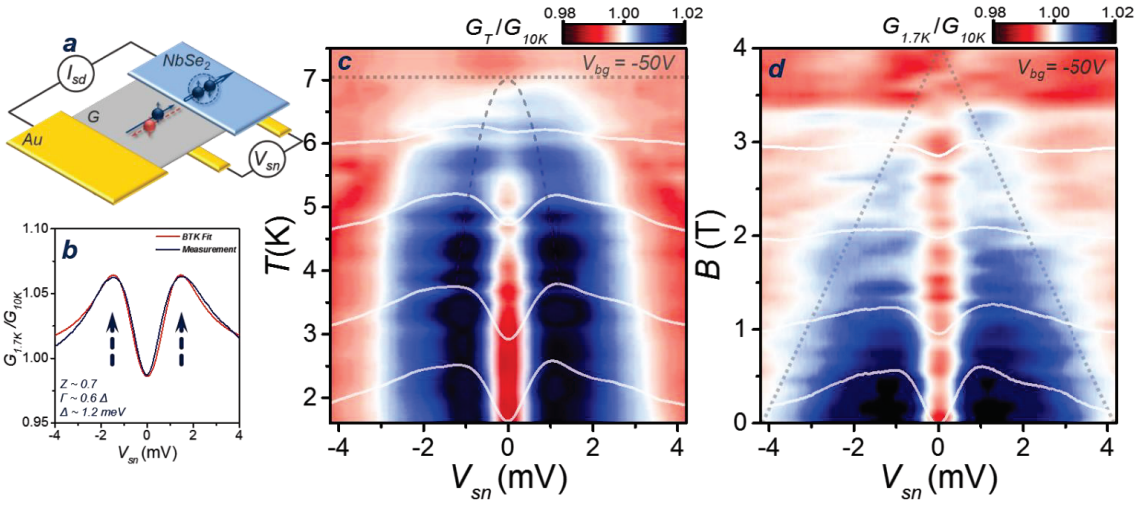

Figure 4.6: (a) Schematics of the current biased measurement setup depicting Andreev reflections at the SN interface. (b) Normalized differential conductance $G_{1.7K}/G_{10K}$ vs. V_{sn} fitted with an adjusted BKT model, with the $Z \sim 0.7$ factor assuring a high probability of AR's. The two conductance peaks identify the SC gap of $NbSe_2$ Δ_{NbSe_2}. (c) T-dependence of $G_{1.7K}/G_{10K}$ vs. V_{sn} showing the closing of Δ_{NbSe_2} with a $\Delta_{NbSe_2}(T) \sim 1.74\Delta_0\sqrt{1-T/T_c}$ dependence, which is in good agreement with the BCS theory (dashed line) with a $T_c \sim$ 7.2 K. (d) T-dependence of $G_{1.7K}/G_{10K}$ vs. V_{sn} showing an almost linear $\Delta_{NbSe_2}(B)$ dependence up to $H_{c2} \sim 4$ T.

fully quantized plateaus in R_{xy} and zero resistance in R_{xx} below H_{c2} (Fig. 4.7 (a)). This experimental scheme has clear advantages since the gaps between these LLs are much larger than for LLs with higher ν hence allowing for a better resolution of these gaps. The corresponding $G_{1.7K}/G_{10K}$ vs. V_{sn} as a function of B is shown in Fig. 4.7 (b). Here, while the outer gap regions are seemingly featureless, the inner gap region shows clear variations of high (blue) and low (red) conductance regions that seem to coincide with the B-field positions of the corresponding plateaus. Zooming in on the inner gap region $|eV_{sn}| \sim \Delta_{NbSe_2}$ we can resolve two striking features (Fig. 4.7 (c)). Here, additionally to the approximately triangular region around $V_{sn} \sim 0$ mV with its strong conductance variations due to ARs we observe diagonal conductance variations cutting through the graph, with their B-field positions at $V_{sn} \sim 0$ mV exactly coinciding with the plateaus regions in R_{xy}.

We conclude that these diagonal segments in the V_{sn} vs. B map mark the LLs. As can be seen in Fig. 4.7 (e), the LL dispersion relation as a function of B and ϵ scales almost

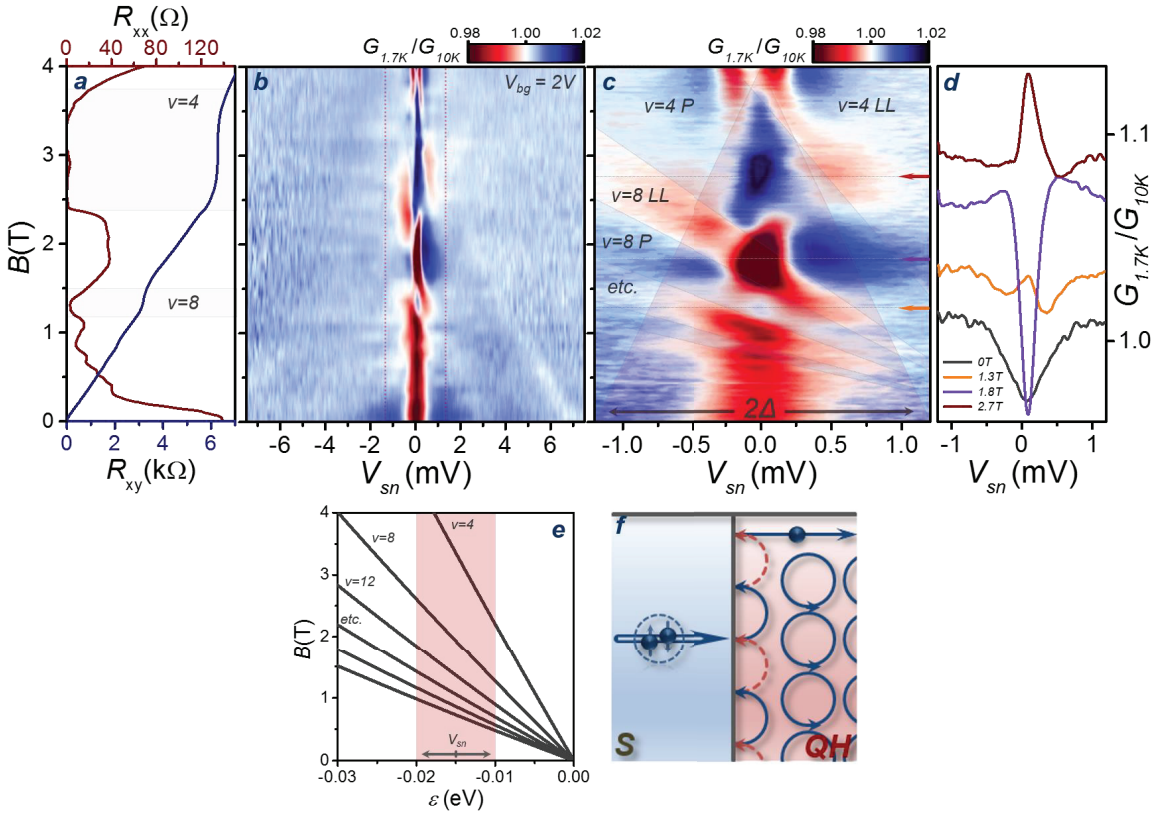

Figure 4.7: (a) Resistance R of the $NbSe_2$ crystal versus temperature T. The crystal undergoes a CDW and a SC phase transition below $T_{cdw} \sim 33$ K and $T_c \sim 6.8$ K respectively, manifesting itself in a "hump" and a sharp drop to zero resistance with a transition width of $\delta T \sim 0.1$ K (inset). (b) Fabrication of a hBN/graphene/$NbSe_2$ stack. The cleaved $NbSe_2$ crystal is transferred onto a clean hBN/bilayer graphene stack from one side and four pre-patterned gold electrodes from the other side. We perform 4-terminal current-biased measurements to characterize the junction. (c) Sketch of the cross-section of a vertical hBN/bilayer graphene/$NbSe_2$ stack (left). AFM image of the junction area (right) demonstrates the sharpness and smoothness of the so created SN junction. (d) Inset : typical 4-terminal current-biased I-V measurements for different V_{bg} showing linear, Ohmic characteristics. Contact resistance R_{cnt} versus back gate voltage V_{bg} before (red line) and after (grey line) current annealing across the junction with $I_{anneal} = 2$ mA, resulting in a clear decrease of R_{cnt} after the current is applied, obtaining a minimal contact resistance of $R_{cnt} \sim 400\ \Omega$ ($V_{bg} = -40$ V).

linearly. Here, by haven set the Fermi energy ϵ_F by the back gate $V_{bg} = 2$ V and by applying a bias voltage V_{sn} across the SN interface we can effectively probe the energy levels of the different LLs. A Cooper pair can only be injected into graphene as an electron-hole pair if the energy of the LLs coincides with the Fermi energy level of $NbSe_2$, which here, owing to a finite tunneling junction at the SN interface can be tuned by V_{sn}. Indeed, by matching the Fermi energy shift caused by V_{sn}, we can overlay the LL dispersion relation with Fig. 4.7 (c) finding good agreement with the measurement. We can hence define each segment as compressible regions of partially filled LLs (marked as LL) and incompressible regions of fully filled LLs (the QHP) respectively (Fig. 4.7 (c)).

These segments in the B-V_{sn} diagram are convoluted with the triangular region that is marking $\Delta_{NbSe_2}(B)$, so defining regions where Cooper pairs are injected into the compressible and incompressible QH regime. Having assigned these segments we can now analyze the interplay between ARs and QHE by comparing $G_{1.7K}/G_{10K}$ vs. V_{sn} for different B-fields in Fig. 4.7 (d). We find severe differences when graphene is in the compressible vs. the incompressible regime, where for the first the inner gap conductance is always decreased and for the later the inner gap conductance is strongly increased.

This effect can be explained by the formation of ABS at the SN interface. Since in the incompressible regime the bulk of the device is not conductive, the electrons and holes that are created by an incident Cooper pair at the SN interface cannot diffuse away into the bulk, but can only be bent back onto the SN interface, where they are AR again. The so created alternating electron and hole states are bound to the SN interface so forming ABS. The existence of these additional conductance states can effectively increase the overall conductance of the SN junction as now every electron that is injected into the graphene has multiple attempts to be AR as it is bent back onto the SN interface several times, effectively increasing the overall AR probability. In addition this effect can be also increased due to the chiral nature of the edge states. As the edge state are not allowed to back-scatter at the SN interface an incident electron must have an increased AR probability.

Bibliography

[1] K. S. Novoselov, D. Jiang, F. Schedin, T. J. Booth, V. V. Khotkevich, S. V. Morozov, and A. K. Geim. Two-dimensional atomic crystals. *PNAS*, 102(30), 2005.

[2] K. S. Novoselov, A. K. Geim, S. V. Morozov, D. Jiang, Y. Zhang, S. V. Dubonos, I. V. Grigorieva, and A. A. Firsov. Electric field effect in atomically thin carbon films. *Science*, 306(5696), 2004.

[3] K. S. Novoselov, A. K. Geim, S. V. Morozov, D. Jiang, M. I. Katsnelson, I. V. Grigorieva, S. V. Dubonos, and A. A. Firsov. Two-dimensional gas of massless Dirac fermions in graphene. *Nature*, 438(7065), 2005.

[4] Y. Zhang, Y. W. Tan, H. L. Stormer, and P. Kim. Experimental observation of the quantum Hall effect and Berry's phase in graphene. *Nature*, 438(7065), 2005.

[5] H. Min, R. Bistritzer, J.J. Su, and A. H. MacDonald. Room-temperature superfluidity in graphene bilayers. *Physical Review B*, 78:121401, 2008.

[6] M. Y. Kharitonov and K. B. Efetov. Excitonic condensation in a double-layer graphene system. *Semiconductor Science and Technology*, 25(3), 2010.

[7] C. H. Park, F. Giustino, J. L. McChesney, A. Bostwick, T. Ohta, E. Rotenberg, M. L. Cohen, and S. G. Louie. Van Hove singularity and apparent anisotropy in the electron-phonon interaction in graphene. *Physical Review B*, 77, 2007.

[8] N. B. Kopnin and E. B. Sonin. BCS superconductivity of Dirac electrons in graphene layers. *Physical Review Letters*, 100(24), 2008.

[9] J. L. McChesney, A. Bostwick, T. Ohta, T. Seyller, K. Horn, J. Gonzalez, and E. Rotenberg. Extended van Hove singularity and superconducting instability in doped graphene. *Physical Review Letters*, 104(13), 2010.

[10] R. Nandkishore, L. S. Levitov, and A. V. Chubukov. Chiral superconductivity from repulsive interactions in doped graphene. *Nature Physics*, 8(2), 2012.

[11] S. Das Sarma, S. Adam, E. H. Hwang, and E. Rossi. Electronic transport in two-dimensional graphene. *Reviews of Modern Physics*, 83(2), 2011.

[12] A. K. Geim. Graphene : Status and prospects. *Science*, 324(5934), 2009.

[13] A. K. Geim. Nobel lecture : Random walk to graphene. *Reviews of Modern Physics*, 83(3), 2011.

[14] A. K. Geim and K. S. Novoselov. The rise of graphene. *Nature Materials*, 6(3), 2007.

[15] A. K. Geim. Graphene prehistory. *Physica Scripta*, 146, 2012.

[16] A. K. Geim and P. Kim. Carbon wonderland. *Scientific American*, 298(4), 2008.

[17] S. V. Morozov, K. S. Novoselov, and A. K. Geim. Electron transport in graphene. *Physics-Uspekhi*, 51(7), 2008.

[18] G. E. Blonder, M. Tinkham, and T. M. Klapwijk. Transition from metallic to tunneling regimes in superconducting micro-constrictions - excess current, charge imbalance, and super-current conversion. *Physical Review B*, 25(7), 1982.

[19] C. W. J. Beenakker. Specular Andreev reflection in graphene. *Physical Review Letters*, 97(6), 2006.

[20] H. Yuan, H. Shimotani, A. Tsukazaki, A. Ohtomo, M. Kawasaki, and Y. Iwasa. High-density carrier accumulation in ZnO field-effect transistors gated by electric double layers of ionic liquids. *Advanced Functional Materials*, 19(7), 2009.

[21] J. T. Ye, S. Inoue, K. Kobayashi, Y. Kasahara, H. T. Yuan, H. Shimotani, and Y. Iwasa. Liquid-gated interface superconductivity on an atomically flat film. *Nature Materials*, 9(2), 2010.

[22] H. Yuan, H. Liu, H. Shimotani, H. Guo, M. Chen, Q. Xue, and Y. Iwasa. Liquid-gated ambipolar transport in ultrathin films of a topological insulator Bi_2Te_3. *Nano Letters*, 11(7), 2011.

[23] Y. J. Zhang, J. T. Ye, Y. Yomogida, T. Takenobu, and Y. Iwasa. Formation of a stable p-n junction in a liquid-gated MoS_2 ambipolar transistor. *Nano Letters*, 13(7), 2013.

[24] A. T. Bollinger, G. Dubuis, J. Yoon, D. Pavuna, J. Misewich, and I. Bozovic. Superconductor-insulator transition in $La_{2-x}Sr_xCuO_4$ at the pair quantum resistance. *Nature*, 472(7344), 2011.

[25] K. Ueno, S. Nakamura, H. Shimotani, A. Ohtomo, N. Kimura, T. Nojima, H. Aoki, Y. Iwasa, and M. Kawasaki. Electric-field-induced superconductivity in an insulator. *Nature Materials*, 7, 2008.

[26] D. K. Efetov and P. Kim. Controlling electron-phonon interactions in graphene at ultrahigh carrier densities. *Physical Review Letters*, 105(25), 2010.

[27] D. K. Efetov, P. Maher, S. Glinskis, and P. Kim. Multiband transport in bilayer graphene at high carrier densities. *Physical Review B*, 84, 2011.

[28] M. P. A. Fisher. Cooper-pair tunneling into a quantum Hall fluid. *Physical Review B*, 49(20), 2000.

[29] U. Zulicke, H. Hoppe, and G. Schon. Andreev reflection at superconductor-semiconductor interfaces in high magnetic fields. *Physica B-Condensed Matter*, 298(1), 2001.

[30] C. R. Dean, A. F. Young, I. Meric, C. Lee, L. Wang, S. Sorgenfrei, K. Watanabe, T. Taniguchi, P. Kim, K. L. Shepard, and J. Hone. Boron nitride substrates for high-quality graphene electronics. *Nature Nanotechnology*, 5(10), 2010.

[31] H. B. Heersche, P. Jarillo-Herrero, J. B. Oostinga, L. M. K. Vandersypen, and A. F. Morpurgo. Bipolar supercurrent in graphene. *Nature*, 446(7131), 2007.

[32] M. Popinciuc, V. E. Calado, X. L. Liu, A. R. Akhmerov, T. M. Klapwijk, and L. M. K. Vandersypen. Zero-bias conductance peak and Josephson effect in graphene-NbTiN junctions. *Physical Review B*, 85(20), 2012.

[33] P. R. Wallace. The band theory of graphite. *Physical Review*, 71, 1947.

[34] E. McCann and M. Koshino. The electronic properties of bilayer graphene. *Reports on Progress in Physics*, 76(5), 2013.

[35] V. I. Fal'ko. Electronic properties and the quantum Hall effect in bilayer graphene. *Philosophical Transactions*, 366(1863), 2008.

[36] M. Tinkham. *Introduction to superconductivity*. McGraw Hill, New York, 1996.

[37] G. Profeta, M. Calandra, and F. Mauri. Phonon-mediated superconductivity in graphene by lithium deposition. *Nature Physics*, 2012.

[38] M. S. Dresselhaus and G. Dresselhaus. Intercalation compounds of graphite. *Advances in Physics*, 2002.

[39] M. Calandra and F. Mauri. Theoretical explanation of superconductivity in CaC_6. *Physical Review Letters*, 95(23), 2005.

[40] N. Emery, C. Herold, M. d'Astuto, V. Garcia, Ch. Bellin, J. F. Mareche, P. Lagrange, and G. Loupias. Superconductivity of bulk CaC_6. *Physical Review Letters*, 95(8), 2005.

[41] Z. H. Pan, J. Camacho, M. H. Upton, A. V. Fedorov, C. A. Howard, M. Ellerby, and T. Valla. Electronic structure of superconducting KC_8 and nonsuperconducting LiC_6 graphite intercalation compounds : Evidence for a graphene-sheet-driven superconducting state. *Physical Review Letters*, 106(18), 2011.

[42] T. Valla, J. Camacho, Z. H. Pan, A. V. Fedorov, A. C. Walters, C. A. Howard, and M. Ellerby. Anisotropic electron-phonon coupling and dynamical nesting on the graphene sheets in superconducting CaC_6 using angle-resolved photoemission spectroscopy. *Physical Review Letters*, 102(10), 2009.

[43] M. J. Rosseinsky, A. P. Ramirez, S. H. Glarum, D. W. Murphy, R. C. Haddon, A. F. Hebard, T. T. Palstra, A. R. Kortan, S. M. Zahurak, and A. V. Makhija. Superconductivity at 28 K in Rb_xC_{60}. *Physical Review Letters*, 66(21), 1991.

[44] W. Shi, Z. Wang, Q. Zhang, Y. Zheng, C. Ieong, M. He, R. Lortz, Y. Cai, N. Wang, T. Zhang, H. Zhang, Z. Tang, P. Sheng, H. Muramatsu, Y. A. Kim, M. Endo, P. T. Araujo, and M. S. Dresselhaus. Superconductivity in bundles of double-wall carbon nanotubes. *Scientific Reports*, 2, 2012.

[45] B. Pannetier and H. Courtois. Andreev reflection and proximity effect. *Journal of Low Temperature Physics*, 118(5-6), 2000.

[46] T. M. Klapwijk. Proximity effect from an Andreev perspective. *Journal of Superconductivity*, 17(5), 2004.

[47] A. F. Andreev. The thermal conductivity of the intermediate state in superconductors. *JETP*, 19(5), 1964.

[48] C. W. J. Beenakker. Colloquium : Andreev reflection and Klein tunneling in graphene. *Reviews of Modern Physics*, 80(4), 2008.

[49] N. M. Chtchelkatchev and I. S. Burmistrov. Conductance oscillations with magnetic field of a two-dimensional electron gas-superconductor junction. *Electron Transport in Nanosystems*, 2008.

[50] I. M. Khaymovich, N. M. Chtchelkatchev, I. A. Shereshevskii, and A. S. Mel'nikov. Andreev transport in two-dimensional normal-superconducting systems in strong magnetic fields. *Europhysics Letters*, 91(1), 2010.

[51] H. Hoppe, U. Zulicke, and G. Schon. Andreev reflection in strong magnetic fields. *Physical Review Letters*, 84(8), 2000.

[52] H. Takayanagi and T. Akazaki. Semiconductor-coupled superconducting junctions using NbN electrodes with high H_{c2} and T_c. *Physica B*, 251, 1998.

[53] J. Nitta, T. Akazaki, and H. Takayanagi. Magnetic-field dependence of Andreev reflection in a clean Nb-InAs-Nb junction. *Physical Review B*, 49(5), 1994.

[54] C. Nguyen, H. Kroemer, and E. L. Hu. Anomalous Andreev conductance in InAs-AlSb quantum-well structures with Nb electrodes. *Physical Review Letters*, 69(19), 1992.

[55] T. D. Moore and D. A. Williams. Andreev reflection at high magnetic fields. *Physical Review B*, 59(11), 1999.

[56] A. Kastalsky, A. W. Kleinsasser, L. H. Greene, R. Bhat, F. P. Milliken, and J. P. Harbison. Observation of pair currents in superconductor-semiconductor contacts. *Physical Review Letters*, 67(21), 1991.

[57] J. Eroms and D. Weiss. Transport in Nb-InAs structures : from phase coherence to the edge state regime. *Applied Physics A - Materials Science and Processing*, 89(3), 2007.

[58] I. E. Batov, T. Schapers, N. M. Chtchelkatchev, H. Hardtdegen, and A. V. Ustinov. Andreev reflection and strongly enhanced magnetoresistance oscillations in $Ga_xIn_{1-x}As$/InP heterostructures with superconducting contacts. *Physical Review B*, 76(11), 2007.

[59] Y. deWilde, T. M. Klapwijk, A. G. M. Jansen, J. Heil, and P. Wyder. Quasi-particle lifetime broadening in normal-superconductor junctions with UPt_3. *Physica B*, 218(1), 1996.

[60] J. Cayssol. Crossed Andreev reflection in a graphene bipolar transistor. *Physical Review Letters*, 100(14), 2008.

[61] F. Giazotto, F. Taddei, F. Beltram, and R. Fazio. Crossed Andreev reflection-induced magnetoresistance. *Physical Review Letters*, 97(8), 2006.

[62] B. Anderson and R. Anderson. *Fundamentals of semiconductor devices*. McGraw-Hill, 2005.

[63] C. H. Ahn, J. M. Triscone, and J. Mannhart. Electric field effect in correlated oxide systems. *Nature*, 424(6952), 2003.

[64] A.J. Bard and L.R. Faulkner. *Electrochemical methods : Fundamentals and applications*. Wiley, 2000.

[65] M. J. Panzer and C. D. Frisbie. Exploiting ionic coupling in electronic devices : Electrolyte-gated organic field-effect transistors. *Advanced Materials*, 20, 2008.

[66] A. Das, S. Pisana, B. Chakraborty, S. Piscanec, S. K. Saha, U. V. Waghmare, K. S. Novoselov, H. R. Krishnamurthy, A. K. Geim, A. C. Ferrari, and A. K. Sood. Monitoring dopants by Raman scattering in an electrochemically top-gated graphene transistor. *Nature Nanotechnology*, 3, 2008.

[67] K. F. Mak, C. Lui, J. Shan, and T. Heinz. Observation of an electric-field-induced band gap in bilayer graphene by infrared spectroscopy. *Physical Review Letters*, 102(25), 2009.

[68] J. Yan, T. Villarson, E. A. Henriksen, P. Kim, and A. Pinczuk. Optical phonon mixing in bilayer graphene with a broken inversion symmetry. *Physical Review B*, 80(24), 2009.

[69] B. H. Brandow. Electronic structure of Mott insulators. *Advances In Physics*, 26(5), 1977.

[70] M. Imada, A. Fujimori, and Y. Tokura. Metal-insulator transitions. *Reviews of Modern Physics*, 70(4), 1998.

[71] Y. Klein and I. Terasaki. Insight on the electronic state of Sr_2IrO_4 revealed by cationic substitutions. *Journal Of Physics-Condensed Matter*, 20(29), 2008.

[72] D. Haskel, G. Fabbris, M. Zhernenkov, P. P. Kong, C. Q. Jin, G. Cao, and M. van Veenendaal. Pressure tuning of the spin-orbit coupled ground state in Sr_2IrO_4. *Physical Review Letters*, 109(2), 2012.

[73] B. J. Kim, H. Jin, S. J. Moon, J.-Y. Kim, B.-G. Park, C. S. Leem, J. Yu, T. W. Noh, C. Kim, and S.-J. Oh. Novel $J_{eff} = 1/2$ Mott state induced by relativistic spin-orbit coupling in Sr_2IrO_4. *Physical Review Letters*, 101(7), 2008.

[74] S. J. Moon, H. Jin, W. S. Choi, J.-S. Lee, S. Seo, J. Yu, G. Cao, T. W. Noh, and Y. S. Lee. Temperature dependence of the electronic structure of the $J_{eff} = 1/2$ Mott insulator Sr_2IrO_4 studied by optical spectroscopy. *Physical Review B*, 80(19), 2009.

[75] D. Hsieh, F. Mahmood, D. Torchinsky, G. Cao, and N. Gedik. Observation of a metal-to-insulator transition with both Mott-Hubbard and Slater characteristics in Sr_2IrO_4 from time-resolved photocarrier dynamics. *Physical Review B*, 86(3), 2012.

[76] J. Dai, E. Calleja, G. Cao, and K. McElroy. Local density of states study of a spin-orbit-coupling induced Mott insulator Sr_2IrO_4. *arXiv:1303.3688*, 2013.

[77] Q. Li, G. Cao, S. Okamoto, J. Yi, W. Lin, B. C. Sales, J. Yan, R. Arita, J. Kuneš, and A. V. Kozhevnikov. Microscopic and spectroscopic evidence for a Slater metal-insulator transition in Sr_2IrO_4. *arXiv:1303.7265*, 2013.

[78] G. Cao, J. Bolivar, S. Mccall, J. Crow, and R. Guertin. Weak ferromagnetism, metal-to-nonmetal transition, and negative differential resistivity in single-crystal Sr_2IrO_4. *Physical Review B*, 57(18), 1998.

[79] S. Boseggia, R. Springell, H. C. Walker, H. M. Ronnow, Ch. Rüegg, H. Okabe, M. Isobe, R. S. Perry, S. P. Collins, and D. F. McMorrow. Robustness of basal-plane antiferromagnetic order and the $J_{eff} = 1/2$ state in single-layer iridate spin-orbit Mott insulators. *Physical Review Letters*, 110(11), 2013.

[80] J. Kim, D. Casa, M. H. Upton, T. Gog, Y.-J. Kim, J. F. Mitchell, M. van Veenendaal, M. Daghofer, J. van den Brink, G. Khaliullin, and B. J. Kim. Magnetic excitation spectra of Sr_2IrO_4 probed by resonant inelastic X-ray scattering : establishing links to cuprate superconductors. *Physical Review Letters*, 108(17), 2012.

[81] S. Fujiyama, H. Ohsumi, T. Komesu, J. Matsuno, B. J. Kim, M. Takata, T. Arima, and H. Takagi. Two-dimensional Heisenberg behavior of $J_{eff} = 1/2$ isospins in the paramagnetic state of the spin-orbital Mott insulator Sr_2IrO_4. *Physical Review Letters*, 108(24), 2012.

[82] O. B. Korneta, T. Qi, S. Chikara, S. Parkin, L. E. De Long, P. Schlottmann, and G. Cao. Electron-doped $Sr_2IrO_{4-\delta}$: Evolution of a disordered $J_{eff} = 1/2$ Mott insulator into an exotic metallic state. *Physical Review B*, 82(11), 2010.

[83] F. Wang and T. Senthil. Twisted Hubbard model for Sr_2IrO_4 - magnetism and possible high temperature superconductivity. *Physical Review Letters*, 106(13), 2011.

[84] C. Rayan-Serrao, J. Liu, J. T. Heron, G. Singh-Bhalla, A. Yadav, S. J. Suresha, R. J. Paull, D. Yi, J. H. Chu, M. Trassin, A. Vishwanath, E. Arenholz, C. Frontera, J. Železný, T. Jungwirth, X. Martí, and R. Ramesh. Epitaxy-distorted spin-orbit Mott insulator in Sr_2IrO_4 thin films. *Physical Review B*, 87(8), 2013.

[85] K. Segawa, M. Kofu, S.-H. Lee, I. Tsukada, H. Hiraka, M. Fujita, S. Chang, K. Yamada, and Y. Ando. Zero-doping state and electron-hole asymmetry in an ambipolar cuprate. *Nature Physics*, 6(8), 2010.

[86] E. Arnold. Disorder-induced carrier localization in silicon surface inversion layers. *Applied Physics Letters*, 25, 1974.

[87] D. Tsui and S. Allen. Mott-Anderson localization in the two-dimensional band tail of Si inversion layers. *Physical Review Letters*, 32(21), 1974.

[88] V. L. Nguen, B. Z. Spivak, and B. I. Shklovskii. Tunnel hopping in disordered systems. *JETP*, 89, 1985.

[89] Y. Zhang, P. Dai, and M. Sarachik. Magnetoconductance of CdSe in the hopping regime : The effect of quantum interference. *Physical Review B*, 45(16), 1992.

[90] V. Srinivas, M. Rodmar, S. Poon, and Ö. Rapp. Evidence for an insulating ground state in high-resistivity icosahedral AlPdRe from the magnetoresistance. *Physical Review B*, 63(17), 2001.

[91] H. Kamimura, A. Kurobe, and T. Takemori. Magnetoresistance in Anderson-localized systems. *Physica B + C*, 117, 1983.

[92] K. Maki. Critical fluctuation of the order parameter in a superconductor. *Progress in Theoretical Physics*, 40(2), 1968.

[93] B. I. Shklovskii and B. Z. Spivak. Scattering and interference effects in variable range hopping conduction. *Hopping Transport in Solids*, 1991.

[94] N. V. Agrinskaya, V. I. Kozub, and D. V. Shamshur. Temperature dependence of the magnetoresistance in the regime of variable-range hopping conduction : Results for doped CdTe. *JETP*, 80(6), 1995.

[95] R. Rosenbaum, T. Murphy, E. Palm, S. Hannahs, and B. Brandt. Magnetoresistance of insulating amorphous Ni_xSi_{1-x} films exhibiting Mott variable-range hopping laws. *Physical Review B*, 63(9), 2001.

[96] J. Davies and J. Franz. Coulomb gap in sodium tungsten bronzes. *Physical Review Letters*, 57(4), 1986.

[97] J. R. Dahn. Phase diagram of Li_xC_6. *Physical Review B*, 1991.

[98] T. Ohzuku, Y. Iwakoshi, and K. Sawai. Formation of lithium/graphite intercalation compounds in nonaqueous electrolytes and their application as a negative electrode for a lithium ion cell. *Journal of The Electrochemical Society*, 1993.

[99] S. Sorgenfrei, C.-Y. Chiu, R. L. Gonzalez Jr, Y.-J. Yu, P. Kim, Nuckolls C., and K. L. Shepard. Label-free single-molecule detection of DNA-hybridization kinetics with a carbon nanotube field-effect transistor. *Nature Nanotechnology*, 6(8), 2011.

[100] T. Ichino, B. D. Cahan, and Y. Da Scherson. In situ attenuated total reflection fourier transform infrared spectroscopy studies of the polyethylene oxide/$LiClO_4$/metallic lithium interface. *Journal of The Electrochemical Society*, 1991.

[101] J. E. Fischer, J. M. Bloch, C. C. Shieh, M. E. Preil, and K. Jelley. Reflectivity spectra and dielectric function of stage-1 donor intercalation compounds of graphite. *Physical Review B*, 1985.

[102] M. H. Yang and P. C. Eklund. Optical dielectric function of high-stage potassium graphite intercalation compounds : Experiment and theory. *Physical Review B*, 1988.

[103] M. Zanini, K. Basu, and S. J. Fisher. Alternate synthesis and reflectivity spectrum of stage 1 lithiumgraphite intercalation compound. *Carbon*, 16(2), 1978.

[104] M. Zanini and J. E. Fischer. Polarized reflectance of alkali metal - graphite intercalation compounds. *Materials Science and Engineering*, 1977.

[105] M. Dussauze, J. Grondin, and J. C. Lassègues. Spectroscopic study of poly(ethylene oxide)$_6$: LiX complexes (X=PF_6, AsF_6, SbF_6, ClO_4). *Physical Chemistry*, 2003.

[106] A. C. Crowther, A. Ghassaei, N. Jung, and L. Brus. Strong charge-transfer doping of 1 to 10 layer graphene by NO_2. *ACS Nano*, 2012.

[107] N. Jung, A. C. Crowther, N. Kim, P. Kim, and L. Brus. Raman enhancement on graphene : Adsorbed and intercalated molecular species. *ACS Nano*, 2010.

[108] G. Csányi, P. B. Littlewood, A. H. Nevidomskyy, and C. J. Pickard. The role of the interlayer state in the electronic structure of superconducting graphite intercalated compounds. *Nature Physics*, 2005.

[109] A. A. Abrikosov. *Fundamentals of the theory of metals*. North-Holland, 1988.

[110] F. Bloch. Zum elektrischen Widerstandsgesetz bei tiefen Temperaturen. *Zeitschrift für Physik*, 1930.

[111] E. Grüneisen. Die Abhngigkeit des elektrischen Widerstandes reiner Metalle von der Temperatur. *Annalen der Physik*, 408(5), 1933.

[112] W. Meissner. *Handbuch der Experimentalphysik*. Akademische Verlagsgesellschaft, 1935.

[113] M. S. Fuhrer. Textbook physics from a cutting-edge material. *Physics*, 3, 2010.

[114] H. Stormer, L. Pfeiffer, K. Baldwin, and K. West. Observation of a Bloch-Grüneisen regime in two-dimensional electron transport. *Physical Review B*, 41(2), 1990.

[115] E. Hwang and S. das Sarma. Acoustic phonon scattering limited carrier mobility in two-dimensional extrinsic graphene. *Physical Review B*, 77(11), 2008.

[116] J.-H. Chen, C. Jang, S. Xiao, M. Ishigami, and M. S. Fuhrer. Intrinsic and extrinsic performance limits of graphene devices on SiO_2. *Nature Nanotechnology*, 3(4), 2008.

[117] S. Morozov, K. Novoselov, M. Katsnelson, F. Schedin, D. Elias, J. Jaszczak, and A. Geim. Giant intrinsic carrier mobilities in graphene and its bilayer. *Physical Review Letters*, 100(1), 2008.

[118] E. Hwang and S. das Sarma. Screening-induced temperature-dependent transport in two-dimensional graphene. *Physical Review B*, 79(16), 2009.

[119] S. das Sarma, E. H. Hwang, and E. Rossi. Theory of carrier transport in bilayer graphene. *Physical Review B*, 81(16), 2010.

[120] K. I. Bolotin, K. J. Sikes, J. Hone, H. L. Stormer, and P. Kim. Temperature-dependent transport in suspended graphene. *Physical Review Letters*, 101(9), 2008.

[121] L. Pietronero, S. Strässler, H. Zeller, and M. Rice. Electrical conductivity of a graphite layer. *Physical Review B*, 22(2), 1980.

[122] H. Suzuura and T. Ando. Phonons and electron-phonon scattering in carbon nanotubes. *Physical Review B*, 65(23), 2002.

[123] S Ono and K Sugihara. Theory of the transport properties in graphite. *Journal of Physical Society op Japan*, 21(5), 1966.

[124] K. Sugihara. Thermoelectric power of graphite intercalation compounds. *Physical Review B*, 28, 1983.

[125] H. L. Störmer, A. C. Gossard, and W. Wiegmann. Observation of intersubband scattering in a 2-dimensional electron system. *Solid State Communications*, 41(10), 1982.

[126] D. R. Leadley, R. J. Nicholas, J. J. Harris, and C. T. Foxon. Inter-subband scattering rates in GaAs-GaAlAs heterojunctions. *Semiconductor Science and Technology*, 5(11), 1990.

[127] G. Facer, B. Kane, R. Clark, L. Pfeiffer, and K. West. Carrier-lifetime enhancement and mass discontinuity inferred from transport in a parabolic quantum well during subband depopulation. *Physical Review B*, 56(16), 1997.

[128] J. Shabani, Y. Liu, and M. Shayegan. Fractional quantum Hall effect at high fillings in a two-subband electron system. *Physical Review Letters*, 105(24), 2010.

[129] E. McCann. Asymmetry gap in the electronic band structure of bilayer graphene. *Physical Review B*, 74(16), 2006.

[130] T. Ohta, A. Bostwick, T. Seyller, K. Horn, and E. Rotenberg. Controlling the electronic structure of bilayer graphene. *Science*, 313(5789), 2006.

[131] K. S. Novoselov, E. McCann, S. V. Morozov, V. I. Falko, M. I. Katsnelson, U. Zeitler, D. Jiang, Schedin. F., and A. K. Geim. Unconventional quantum Hall effect and Berry's phase of 2π in bilayer graphene. *Nature Physics*, 2, 2006.

[132] E. Castro, K. Novoselov, S. Morozov, N. Peres, J. dos Santos, J. Nilsson, F. Guinea, A. K. Geim, and A. Neto. Biased bilayer graphene : Semiconductor with a gap tunable by the electric field effect. *Physical Review Letters*, 99(21), 2007.

[133] J. B. Oostinga, H. B. Heersche, X. Liu, A. F. Morpurgo, and L. M. K. Vandersypen. Gate-induced insulating state in bilayer graphene devices. *Nature Materials*, 7, 2007.

[134] Y. Zhang, T.-T. Tang, C. Girit, Z. Hao, M. C. Martin, A. Zettl, M. F. Crommie, Y. R. Shen, and F. Wang. Direct observation of a widely tunable bandgap in bilayer graphene. *Nature*, 459(7248), 2009.

[135] J. Ye, M. F. Craciun, M. Koshino, S. Russo, S. Inoue, H. Yuan, H. Shimotani, A. F. Morpurgo, and Y. Iwasa. Accessing the transport properties of graphene and its multilayers at high carrier density. *PNAS*, 2011.

[136] S. Cho and M. Fuhrer. Charge transport and inhomogeneity near the minimum conductivity point in graphene. *Physical Review B*, 77(8), 2008.

[137] H. van Houten, J. G. Williamson, M. E. I. Broekaart, C. T. Foxon, and J. J. Harris. Magnetoresistance in a GaAs-heterostructure with double subband occupancy. *Physical Review B*, 37, 1988.

[138] N. W. Ashcroft and N. D. Mermin. *Solid State Physics*. New York : Holt, 1976.

[139] E. Zaremba. Transverse magnetoresistance in quantum wells with multiple subband occupancy. *Physical Review B*, 45, 1992.

[140] A. K. Geim and I. V. Grigorieva. Van der Waals heterostructures. *Nature*, 499(7459), 2013.

[141] L. Britnell, R. M. Ribeiro, A. Eckmann, R. Jalil, B. D. Belle, A. Mishchenko, Y. J. Kim, R. V. Gorbachev, T. Georgiou, S. V. Morozov, A. N. Grigorenko, A. K. Geim, C. Casiraghi, A. H. C. Neto, and K. S. Novoselov. Strong light-matter interactions in heterostructures of atomically thin films. *Science*, 340(6138), 2013.

[142] C. R. Dean, A. F. Young, P. Cadden-Zimansky, L. Wang, H. Ren, K. Watanabe, T. Taniguchi, P. Kim, J. Hone, and K. L. Shepard. Multicomponent fractional quantum Hall effect in graphene. *Nature Physics*, 7(9), 2011.

[143] M. Yankowitz, J. M. Xue, D. Cormode, J. D. Sanchez-Yamagishi, K. Watanabe, T. Taniguchi, P. Jarillo-Herrero, P. Jacquod, and B. J. LeRoy. Emergence of superlattice Dirac points in graphene on hexagonal boron nitride. *Nature Physics*, 8(5), 2012.

[144] N. M. Gabor, J. C. W. Song, Q. Ma, N. L. Nair, T. Taychatanapat, K. Watanabe, T. Taniguchi, L. S. Levitov, and P. Jarillo-Herrero. Hot carrier-assisted intrinsic photoresponse in graphene. *Science*, 334(6056), 2011.

[145] L. Wang, I. Meric, P. Y. Huang, Q. Gao, Y. Gao, H. Tran, T. Taniguchi, K. Watanabe, L. M. Campos, D. A. Muller, J. Guo, P. Kim, J. Hone, K. L. Shepard, and C. R. Dean.

One-dimensional electrical contact to a two-dimensional material. *Science*, 342(6158), 2013.

[146] S. Gariglio, N. Reyren, A. D. Caviglia, and J. M. Triscone. Superconductivity at the $LaAlO_3/SrTiO_3$ interface. *Journal of Physics-Condensed Matter*, 21(16), 2009.

[147] A. Ohtomo and H. Y. Hwang. A high-mobility electron gas at the $LaAlO_3/SrTiO_3$ heterointerface. *Nature*, 441(7089), 2006.

[148] J. Son, P. Moetakef, B. Jalan, O. Bierwagen, N. J. Wright, R. Engel-Herbert, and S. Stemmer. Epitaxial $SrTiO_3$ films with electron mobilities exceeding 30,000 $cm^2V^{-1}s^{-1}$. *Nature Materials*, 9(6), 2010.

[149] S. Thiel, G. Hammerl, A. Schmehl, C. W. Schneider, and J. Mannhart. Tunable quasi-two-dimensional electron gases in oxide heterostructures. *Science*, 313(5795), 2006.

[150] A. Tsukazaki, A. Ohtomo, T. Kita, Y. Ohno, H. Ohno, and M. Kawasaki. Quantum Hall effect in polar oxide heterostructures. *Science*, 315(5817), 2007.

[151] X. Du, I. Skachko, and E. Y. Andrei. Josephson current and multiple Andreev reflections in graphene SNS junctions. *Physical Review B*, 77(18), 2008.

[152] F. Miao, S. Wijeratne, Y. Zhang, U. C. Coskun, W. Bao, and C. N. Lau. Phase-coherent transport in graphene quantum billiards. *Science*, 317(5844), 2007.

[153] K. Komatsu, C. Li, S. Autier-Laurent, H. Bouchiat, and S. Gueron. Superconducting proximity effect in long superconductor/graphene/superconductor junctions: From specular Andreev reflection at zero field to the quantum Hall regime. *Physical Review B*, 86(11), 2012.

[154] P. Rickhaus, M. Weiss, L. Marot, and C. Schonenberger. Quantum Hall effect in graphene with superconducting electrodes. *Nano Letters*, 12(4), 2012.

[155] B. P. Clayman and R. F. Frindt. Superconducting energy gap of $NbSe_2$. *Solid State Communications*, 9(22), 1971.

[156] R. F. Frindt. Superconductivity in ultrathin $NbSe_2$ layers. *Physical Review Letters*, 28(5), 1972.

[157] I. Naik and A. K. Rastogi. Charge density wave and superconductivity in 2H-and 4H-$NbSe_2$: A revisit. *Pramana-Journal of Physics*, 76(6), 2011.

[158] A. Soumyanarayanan, M. M. Yee, Y. He, J. van Wezel, D. J. Rahn, K. Rossnagel, E. W. Hudson, M. R. Norman, and J. E. Hoffman. Quantum phase transition from triangular to stripe charge order in $NbSe_2$. *PNAS*, 110(5), 2013.

[159] N. E. Staley, J. Wu, P. Eklund, Y. Liu, L. J. Li, and Z. Xu. Electric field effect on superconductivity in atomically thin flakes of $NbSe_2$. *Physical Review B*, 80(18), 2009.

[160] T. Ludwig. Andreev reflection in bilayer graphene. *Physical Review B*, 75(19), 2007.

[161] J. Martin, N. Akerman, G. Ulbricht, T. Lohmann, J. H. Smet, K. Von Klitzing, and A. Yacoby. Observation of electron-hole puddles in graphene using a scanning single-electron transistor. *Nature Physics*, 4(2), 2008.

[162] J. M. Xue, J. Sanchez-Yamagishi, D. Bulmash, P. Jacquod, A. Deshpande, K. Watanabe, T. Taniguchi, P. Jarillo-Herrero, and B. J. Leroy. Scanning tunnelling microscopy and spectroscopy of ultra-flat graphene on hexagonal boron nitride. *Nature Materials*, 10(4), 2011.

[163] K. M. Burson, W. G. Cullen, S. Adam, C. R. Dean, K. Watanabe, T. Taniguchi, P. Kim, and M. S. Fuhrer. Direct imaging of charged impurity density in common graphene substrates. *Nano Letters*, 13(8), 2013.

[164] F. N. Xia, V. Perebeinos, Y. M. Lin, Y. Q. Wu, and P. Avouris. The origins and limits of metal-graphene junction resistance. *Nature Nanotechnology*, 6(3), 2011.

[165] T. Y. Chen, S. X. Huang, and C. L. Chien. Pronounced effects of additional resistance in Andreev reflection spectroscopy. *Physical Review B*, 81(21), 2010.

[166] W. J. Tomasch. Geometrical resonance and boundary effects in tunneling from superconducting In. *Physical Review Letters*, 16(1), 1966.

[167] C. Visani, Z. Sefrioui, J. Tornos, C. Leon, J. Briatico, M. Bibes, A. Barthelemy, J. Santamaria, and J. E. Villegas. Equal-spin Andreev reflection and long-range coherent transport in high-temperature superconductor/half-metallic ferromagnet junctions. *Nature Physics*, 8(7), 2012.

[168] T. Wolfram and G. W. Lehman. Theory of Tomasch effect. *Physics Letters A*, A 24(2), 1967.

[169] M. Ma and A. Y. Zyuzin. Josephson effect in the quantum Hall regime. *Europhysics Letters*, 21(9), 1993.

[170] T. Dirks, T. L. Hughes, S. Lal, B. Uchoa, Y. F. Chen, C. Chialvo, P. M. Goldbart, and N. Mason. Transport through Andreev bound states in a graphene quantum dot. *Nature Physics*, 7(5), 2011.